# A CHEMICAL EXPLORATION OF MASSIVE STAR-FORMING REGIONS: UNRAVELING THE MOLECULAR COMPLEXITY OF HOT CORES

**Samer Jamal El-Abd**

B.S. Astronomy-Physics, University of Virginia, 2018

M.S. Astronomy, University of Virginia, 2020

A Dissertation Presented to the Graduate
Faculty of the University of Virginia
in Candidacy for the Degree of
Doctor of Philosophy

Department of Astronomy

University of Virginia
April 2024

Committee Members:

Crystal L. Brogan
Remy Indebetouw
Robin T. Garrod
Kateri H. Dubay

# Abstract

The short-lived massive star formation process is difficult to observe in its early stages and therefore an ill-understood mechanism. Of the regions we have been able to observe, much of the information we are able to glean comes from analysis of their molecular emission spectra, particularly in the radio regime. Star-forming regions are hotbeds of interstellar chemistry; the physical conditions in these regions are conducive to producing a large number of complex interstellar molecules. Attaining a better understanding of this unique chemistry will in turn better inform us on the ongoing physical processes. In this work I describe my efforts to better understand and characterize the molecular emission from massive star-forming regions, and subsequently the physical conditions in which they are found. The relative column densities of the structural isomers methyl formate, glycolaldehyde, and acetic acid are first derived for a dozen positions towards the massive star-forming regions MM1 and MM2 in the NGC 6334I complex, which are separated by ∼4000 au. Relative column densities of these molecules are also gathered from the literature for 13 other star-forming regions. In this combined dataset, a clear bi-modal distribution is observed in the relative column densities of glycolaldehyde and methyl formate. No such distribution is evident with acetic acid. The two trends are comprised of star-forming regions with a variety of masses, suggesting that there must be some other common parameter that is heavily impacting the formation of glycolaldehyde. This is indicative of some demonstrable differentiation in these cores; studying the abundances of these isomers may provide a clue as to the integral chemical processes ongoing in a variety of protostellar environments. The time-consuming nature of fitting synthetic spectra to observations interactively for such line-rich sources often results in such analysis

being limited to data extracted from a single-dish observation or a handful of pixels from an interferometric observation. Yet, star-forming regions display a wide variety of physical conditions that are difficult, if not impossible, to accurately characterize with such a limited number of spectra. I have developed an automated fitting routine that visits every pixel in the field of view of an ALMA data cube and determines the best-fit physical parameters, including excitation temperature and column densities, for a given list of molecules. In this proof-of-concept work, I provide an overview of the fitting routine and apply it to $0\farcs26$, 1.1 km s$^{-1}$ resolution ALMA observations of two sites of massive star-formation in NGC 6334I. Parameters were found for 21 distinct molecules by generating synthetic spectra across 7.48 GHz of spectral bandwidth between 280 and 351 GHz. Spatial images of the derived parameters for each of the $>$ 8000 pixels are presented with special attention paid to the $C_2H_4O_2$ isomers and their relative variations. I highlight the greater scientific utility of the column density and velocity images of individual molecules compared to traditional moment maps of single transitions.

I then apply this routine - the Simultaneous Autonomous Molecular Emission Resolver (SAMER) - to a new high-mass star-forming region, G34.41+0.24. This source is part of the Complex Chemistry in hot Cores with ALMA (CoCCoA) survey, which aims to improve our understanding of the massive star formation process through the observation of twenty-five hot cores in a self-consistent manner across a common spatial resolution, spectral resolution, and frequency range. Preliminary images of the excitation temperature, velocities, and various molecules will be presented, as will interpretations on how they inform us on the physical processes driven by the hot core. Future directions and applications following the results of this work will also be discussed.

# Acknowledgements

Dedicated to my family, friends, and everyone else who's helped me along the way.
I couldn't possibly have done this without you.

# Table of contents

**List of Figures** **ix**

**List of Tables** **x**

**1 Introduction** **1**
1.1 Massive Star Formation . . . 2
1.2 Astrochemistry . . . 5
1.2.1 Gas-Phase and Grain-Surface Chemistry . . . 7
1.3 Applying Astrochemistry to Star Formation . . . 10
1.3.1 Measuring Chemical Abundances . . . 10
1.3.2 Observing Molecular Spatial Distributions . . . 13
1.4 NGC 6334I . . . 15

**2 Chemical Abundance Patterns Across Star Forming Regions** **19**
2.1 Introduction . . . 19
2.2 Observations & Data Reduction . . . 22
2.2.1 Observations . . . 22
2.2.2 Analysis of NGC 6334I . . . 23
2.3 Literature Sources . . . 26
2.4 Results & Discussion . . . 28
2.5 Conclusions . . . 33

**3 Streamlining the Process of Measuring Interstellar Molecules** **36**
3.1 Introduction . . . 36
3.2 ALMA Data Characteristics . . . 39
3.2.1 Test Case: NGC 6334I . . . 39
3.2.2 Observations . . . 41
3.3 The Fitting Routine . . . 43
3.3.1 Technique . . . 43
3.3.2 Molecules Included in the Model . . . 48
3.3.3 Exclusion of Channels . . . 49
3.3.4 Uncertainties . . . 52

3.3.5 Identifying Areas of Concern . . . 55
3.4 Results . . . 57
3.4.1 The Shared Parameters - $T_{ex}$, $\Delta V$, and $V_{LSR}$ . . . 57
3.4.2 Column Densities . . . 58
3.4.3 Column Density Ratios . . . 61
3.5 Discussion . . . 62
3.5.1 Previous Findings . . . 62
3.5.2 Collating the Column Density Results . . . 63
3.5.3 Comparison with Traditional Moment Maps . . . 67
3.6 Conclusions . . . 72

**4 Initial Application of SAMER to a Survey of High Mass Star-Forming Regions 75**
4.1 Introduction . . . 75
4.2 G34.41+0.24 . . . 76
4.3 Observations . . . 77
4.4 Methods . . . 77
4.5 Results . . . 79
4.5.1 Excitation Temperature . . . 79
4.5.2 Linewidth . . . 81
4.5.3 Velocity . . . 81
4.5.4 Molecule Images . . . 83
4.6 Conclusions . . . 85

**5 Conclusions 87**
5.1 Next Steps . . . 90

**6 Appendices 92**
A1 Appendix for Chapter 2 . . . 93
A1.1 Beam Corrections . . . 93
A1.2 Full NGC 6334I Simulations for Selected Positions . . . 93
A2 Data for Chapter 3: . . . 111
A2.1 Appendix A - Sample Spectra . . . 111
A2.2 Appendix B - Complete Molecule Results and Uncertainties . 116
A3 Appendix C - Miscellaneous Data . . . 141

# List of Figures


1.1 Proposed schematic for massive star formation . . . . . 4
1.2 Chemical evolution around massive protostars . . . . . 6
1.3 Modeled gas-phase abundances of molecules over time . . . . . 9
1.4 Mechanisms for grain-surface chemistry . . . . . 10
1.5 Rotation diagram example . . . . . 12
1.6 Sample spectrum from a star-forming region . . . . . 14
1.7 Infrared image of NGC 6334 . . . . . 16
1.8 ALMA and Herschel HIFI Spectral Comparison . . . . . 17
1.9 Outburst in NGC 6334I . . . . . 18

2.1 $C_2H_4O_2$ isomer moment maps . . . . . 22
2.2 Bimodal distribution in scatter plots of the $C_2H_4O_2$ isomers . . . . . 29

3.1 NGC 6334I continuum image . . . . . 40
3.2 Sample NGC 6334I-MM1 spectrum with channel masking demonstration 45
3.3 Linewidth histogram demonstration . . . . . 47
3.4 Pixel-hopping scheme for NGC 6334I-MM1 . . . . . 52
3.5 Pixel-hopping scheme for NGC 6334I-MM2 . . . . . 56
3.6 Excitation temperature, linewidth, and velocity images for NGC 6334I-MM1 . . . . . 57
3.7 Excitation temperature, linewidth, and velocity images for NGC 6334I-MM2 . . . . . 58
3.8 Images of the $C_2H_4O_2$ isomers in NGC 6334I-MM1 . . . . . 60
3.9 Images of the $C_2H_4O_2$ isomers in NGC 6334I-MM2 . . . . . 61
3.10 Images of the ratios of the $C_2H_4O_2$ isomers in NGC 6334I-MM1 . . . 62
3.11 Bimodal distribution of the $C_2H_4O_2$ isomers as described by the automated fitting routine . . . . . 64
3.12 Bimodal distribution of the $C_2H_4O_2$ isomers as described by the automated fitting routine colored by temperature . . . . . 66
3.13 Comparison with moment 0 map in NGC 6334I-MM1 . . . . . 67
3.14 Comparison with moment 1 map in NGC 6334I-MM1 . . . . . 68
3.15 Comparison with moment 0 map in NGC 6334I-MM2 . . . . . 70
3.16 Comparison with moment 1 map in NGC 6334I-MM2 . . . . . 72

4.1 Example spectrum from G34.41+0.24 . . . . . 77
4.2 G34.41+0.24 excitation temperature image . . . . . 79
4.3 G34.41+0.24 linewidth image . . . . . 80
4.4 G34.41+0.24 velocity image . . . . . 82
4.5 Image of methyl formate in G34.41+0.24 . . . . . 83
4.6 Image of acetic acid in G34.41+0.24 . . . . . 84
4.7 Image of glycolaldehyde in G34.41+0.24 . . . . . 84

6.1 First set of spectra from NGC 6334I-MM1 . . . . . 95
6.2 Second set of spectra from NGC 6334I-MM1 . . . . . 96
6.3 Third set of spectra from NGC 6334I-MM1 . . . . . 97
6.4 Fourth set of spectra from NGC 6334I-MM1 . . . . . 98
6.5 Fifth set of spectra from NGC 6334I-MM1 . . . . . 99
6.6 Sixth set of spectra from NGC 6334I-MM1 . . . . . 100
6.7 Seventh set of spectra from NGC 6334I-MM1 . . . . . 101
6.8 Eighth set of spectra from NGC 6334I-MM1 . . . . . 102
6.9 First set of spectra from NGC 6334I-MM2 . . . . . 103
6.10 Second set of spectra from NGC 6334I-MM2 . . . . . 104
6.11 Third set of spectra from NGC 6334I-MM2 . . . . . 105
6.12 Fourth set of spectra from NGC 6334I-MM2 . . . . . 106
6.13 Fifth set of spectra from NGC 6334I-MM2 . . . . . 107
6.14 Sixth set of spectra from NGC 6334I-MM2 . . . . . 108
6.15 Seventh set of spectra from NGC 6334I-MM2 . . . . . 109
6.16 Eighth set of spectra from NGC 6334I-MM2 . . . . . 110
6.17 NGC 6334I-MM1 finder image . . . . . 112
6.18 NGC 6334I-MM2 finder image . . . . . 112
6.19 Sample $C_2H_4O_2$ isomer fits to NGC 6334I-MM1 spectra . . . . . 113
6.20 Sample $C_2H_4O_2$ isomer fits to NGC 6334I-MM1 spectra . . . . . 114
6.21 Sample $C_2H_4O_2$ isomer fits to NGC 6334I-MM2 spectra . . . . . 115
6.22 NGC 6334I-MM1 excitation temperature image and uncertainty . . . 116
6.23 NGC 6334I-MM1 linewidth image and uncertainty . . . . . 117
6.24 NGC 6334I-MM1 velocity image and uncertainty . . . . . 117
6.25 NGC 6334I-MM1 methanol image and uncertainty . . . . . 118
6.26 NGC 6334I-MM1 13-methanol image and uncertainty . . . . . 118
6.27 NGC 6334I-MM1 methyl cyanide image and uncertainty . . . . . 119
6.28 NGC 6334I-MM1 13-methyl cyanide image and uncertainty . . . . . 119
6.29 NGC 6334I-MM1 cyanamide image and uncertainty . . . . . 120
6.30 NGC 6334I-MM1 ketene image and uncertainty . . . . . 120
6.31 NGC 6334I-MM1 acetaldehyde image and uncertainty . . . . . 121
6.32 NGC 6334I-MM1 formamide image and uncertainty . . . . . 121
6.33 NGC 6334I-MM1 formic acid image and uncertainty . . . . . 122
6.34 NGC 6334I-MM1 dimethyl ether image and uncertainty . . . . . 122

6.35 NGC 6334I-MM1 ethanol image and uncertainty . . . . . 123
6.36 NGC 6334I-MM1 ethyl cyanide image and uncertainty . . . . . 123
6.37 NGC 6334I-MM1 acetone image and uncertainty . . . . . 124
6.38 NGC 6334I-MM1 methyl formate image and uncertainty . . . . . 124
6.39 NGC 6334I-MM1 glycolaldehyde image and uncertainty . . . . . 125
6.40 NGC 6334I-MM1 acetic acid image and uncertainty . . . . . 125
6.41 NGC 6334I-MM1 13-methyl formate image and uncertainty . . . . . 126
6.42 NGC 6334I-MM1 a-ethylene glycol image and uncertainty . . . . . 126
6.43 NGC 6334I-MM1 g-ethylene glycol image and uncertainty . . . . . 127
6.44 NGC 6334I-MM1 methoxymethanol image and uncertainty . . . . . 127
6.45 NGC 6334I-MM1 sulfur dioxide image and uncertainty . . . . . 128
6.46 NGC 6334I-MM2 excitation temperature image and uncertainty . . . 129
6.47 NGC 6334I-MM2 linewidth image and uncertainty . . . . . 129
6.48 NGC 6334I-MM2 velocity image and uncertainty . . . . . 130
6.49 NGC 6334I-MM2 methanol image and uncertainty . . . . . 130
6.50 NGC 6334I-MM2 13-methanol image and uncertainty . . . . . 131
6.51 NGC 6334I-MM2 methyl cyanide image and uncertainty . . . . . 131
6.52 NGC 6334I-MM2 13-methyl cyanide image and uncertainty . . . . . 132
6.53 NGC 6334I-MM2 cyanamide image and uncertainty . . . . . 132
6.54 NGC 6334I-MM2 ketene image and uncertainty . . . . . 133
6.55 NGC 6334I-MM2 acetaldehyde image and uncertainty . . . . . 133
6.56 NGC 6334I-MM2 formamide image and uncertainty . . . . . 134
6.57 NGC 6334I-MM2 formic acid image and uncertainty . . . . . 134
6.58 NGC 6334I-MM2 dimethyl ether image and uncertainty . . . . . 135
6.59 NGC 6334I-MM2 ethanol image and uncertainty . . . . . 135
6.60 NGC 6334I-MM2 methyl cyanide image and uncertainty . . . . . 136
6.61 NGC 6334I-MM2 acetone image and uncertainty . . . . . 136
6.62 NGC 6334I-MM2 methyl formate image and uncertainty . . . . . 137
6.63 NGC 6334I-MM2 glycolaldehyde image and uncertainty . . . . . 137
6.64 NGC 6334I-MM2 acetic acid image and uncertainty . . . . . 138
6.65 NGC 6334I-MM2 13-methyl formate image and uncertainty . . . . . 138
6.66 NGC 6334I-MM2 a-ethylene glycol image and uncertainty . . . . . 139
6.67 NGC 6334I-MM2 g-ethylene glycol image and uncertainty . . . . . 139
6.68 NGC 6334I-MM2 methoxymethanol image and uncertainty . . . . . 140
6.69 NGC 6334I-MM2 sulfur dioxide image and uncertainty . . . . . 140
6.70 NGC 6334I-MM1 spectral linewidth comparison . . . . . 141
6.71 Source of velocity discrepancy between fitting routine and moment map 142

# List of Tables

2.1 Physical Parameters for Spectra Extraction Locations in NGC 6334I . 27
2.2 Transitions Used to Calculate Isomer Column Densities in NGC 6334I 27
2.3 $C_2H_4O_2$ Isomer Column Densities in Each Source . . . . . 35

3.1 Molecules Included in the Fitting Routine . . . . . 71

# Chapter 1

# Introduction

Massive stars - classically defined as stars whose mass exceeds 8 $M_\odot$ - are relatively rare when compared with their lower-mass counterparts, yet influence their surroundings to such a degree that they play a huge role in the chemical evolution of the interstellar medium. This low frequency with which massive stars form, when combined with their relatively short lives, make for objects that are difficult to study in the early stages of their formation. This is problematic as the formation of massive stars is responsible for much of the chemical enrichment we observe in the interstellar medium, including prebiotic molecules that serve as stepping stones for life to form. By observing the rich molecular envelopes that form around massive star-forming cores we can use the emission spectra from these molecules to attain a better understanding of the physical conditions in which they are formed.

In this work I will describe my efforts to shed light on the early stages of the massive star formation process and its physical properties through characterizing the molecular emission from such regions. In Chapter 2 I detail my work to measure the chemical inventory of the massive star-forming region NGC 6334I with a focus on the $C_2H_4O_2$ isomers; results for these molecules are then compared with values in the lit-

erature for a number of other star-forming regions. In Chapter 3 I describe my efforts to overcome the shortcomings of the previous study - and indeed, the shortcomings of many studies made of star-forming regions - by developing an automated least-squares fitting routine that greatly accelerates the rate at which these measurements of interstellar molecules can be made. This enables novel methods of analysis for star-forming regions, where spectra are often crowded with lines and kinematically complicated across an observed field of view.

## 1.1 Massive Star Formation

The giant molecular clouds (GMCs) that serve as the primary sites of star formation are enormous structures composed of gas and dust. A typical GMC spans tens of parsecs in size and contains up to $10^6$ solar masses of material; the temperature of a quiescent cloud is very cold, on the order of 10 K (Shu et al. 1987; Beuther et al. 2006; Kennicutt & Evans 2012). Density variations due to effects such as turbulence and local gravitational instabilities eventually cause portions of these clouds to begin collapsing (Lada & Lada 2003). These denser regions, which are typically found along filamentary substructures in the GMC, are referred to as "clumps." These clumps have characteristic sizes of $\sim$ 1 pc; contained within this space are both dense cores ($\sim$ 0.1 pc) and individual cores ($\sim$ 0.01 pc) which will go on to form multiple stellar systems (terminology adopted from Motte et al. (2018)). This includes higher-order multiples, in which massive stars are commonly found (Chini et al. 2013).

The formation of low- and medium-mass stars follows a fairly straightforward, well-understood path at the level of an individual core. The core isothermally collapses due to its own gravity, periodically shedding energy in the form of outflows and jets to conserve angular momentum. All the while it continues to gain mass through

infalling matter until the protostellar envelope is exhausted of material and the radiation pressure from the protostar prevents further accretion (Andre et al. 1999; Frank et al. 2014).

Unlike their lower mass counterparts, the formation of massive stars is not as well understood. Attempts to simulate the formation of such massive stars through a scaled-up version of the process described above results in fragmentation of the core, culminating in the formation of several low-mass stars instead. It is feasible that some massive stars are formed this way, but additional mechanisms appear to be required to support the sustained growth of a single massive core against fragmentation, i.e. the turbulent core model of McKee & Tan (2002).

Another theory of massive star formation comes in the form of the competitive accretion model. In this scenario, a star may be favorably positioned within a cluster such that the total gravitational potential of said cluster funnels increased material to the star. This increase in available material to be accreted rapidly increases the mass of the star, which is in line with the accelerated timescales on which massive stars form (Bonnell & Bate 2006). This theory is expanded upon in the global hierarchical collapse model, whereby the small-scale collapse of individual cores takes place within the large-scale collapse of the surrounding clump (Vázquez-Semadeni et al. 2016). An adapted version of the global hierarchical collapse model was put forward by Motte et al. (2018) and is displayed in Figure 1.1.

Recent observational and theoretical evidence suggest that the rate at which massive protostellar objects gain mass is not regular, but instead undergoes periods of rapid accretion which may constitute as much as 60% of a star's final mass (Meyer et al. 2017, 2020). These episodes of accretion are accompanied by events known as accretion outbursts, which release a significant amount of energy and material into

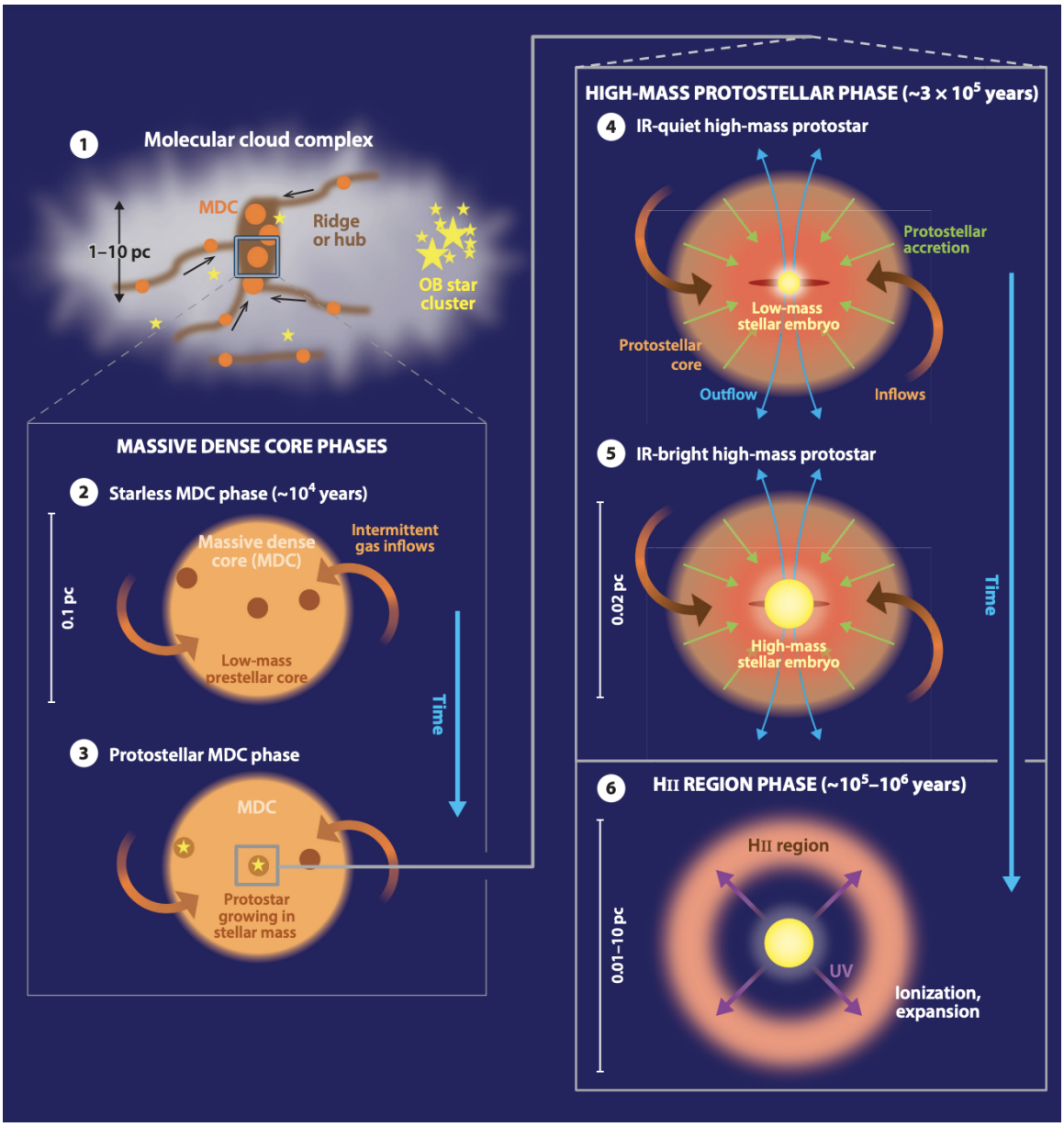


Fig. 1.1.— The global hierarchical collapse model of massive star formation. A low-mass prestellar core is favorably positioned within a clump such that it is able to accrete enough mass that it forms a high-mass protostar. This accretion is driven by both the collapse of the small-scale core, and the large-scale collapse of the clump. This figure originally appeared in Motte et al. (2018), where it was adapted from Tigé et al. (2017).

the surrounding medium (Fischer et al. 2019). Observational evidence currently exists only for three such events in massive protostars; our understanding of their impact on the star formation process is therefore still fairly limited, as lingering effects on the continuum and maser emission varies significantly from source to source (Caratti O Garatti et al. 2017; Brogan et al. 2019; Hunter et al. 2021).

In order to better constrain the formation mechanisms for these stars we must better understand the physical conditions in which these stars form and their subsequent impact on the circum-protostellar environment. In order to do this, we turn to the unique and complex chemistry that can be found in these regions.

## 1.2 Astrochemistry

In the beginning, our universe was composed of a relatively simple mixture of hydrogen and helium, with trace amounts of other elements. As the first generations of stars came online, heavier elements such as carbon, oxygen, and nitrogen were formed in these primordial furnaces through nuclear fusion. Still heavier elements were formed when these stars died in fantastic supernovae, scattering their remains throughout interstellar space. Today, these elements are fundamental components of what are called complex organic molecules (COMs) - interstellar molecules that contain six or more atoms of which at least one is carbon. While not necessarily "complex" by terrestrial chemical standards, the harsh environment of space is generally not conducive to the reactions necessary to form more complicated molecular structures and so this terminology has been adopted (Herbst & Van Dishoeck 2009).

The formation of these molecules is an inherently compelling subject of study as it has the potential to give us answers to one of the most basic questions of all - how did life on Earth come to be? The amino acids and proteins necessary for life are

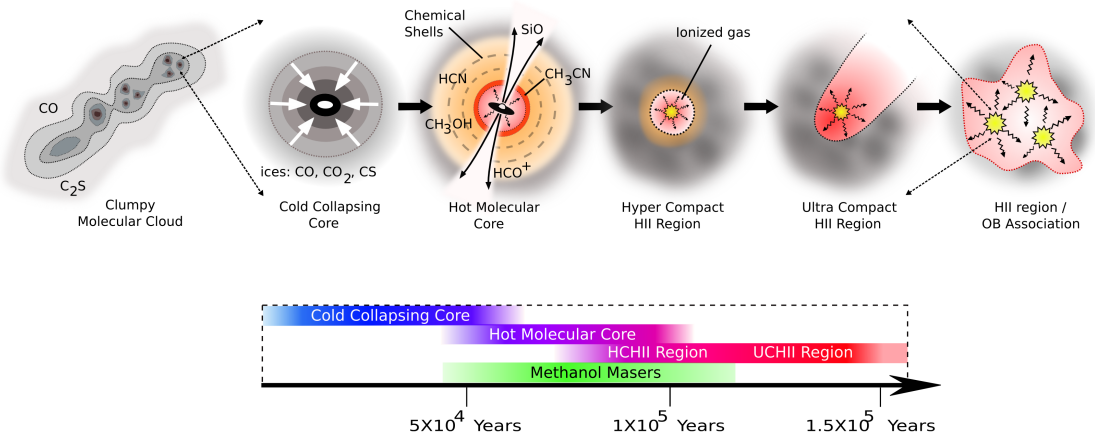


Fig. 1.2.— Another schematic of massive star formation focusing on the chemical evolution in an individual core, including the hot core phase where complex molecules are detectable in the gas phase. Image credit: Cormac Purcell.

more complex than anything found in space thus far - as evidenced by astronomers' continuously stymied efforts to detect glycine, the simplest amino acid (Snyder et al. 2005). Recent evidence does suggest, however, that it may be found in comets (Elsila et al. 2009).

The molecules that have successfully been detected in space are incredibly valuable tools for probing the physical environments in which they're found. From the first detection of CH in 1937 to today, over two hundred distinct molecular species have been detected in the interstellar medium (ISM) (McGuire 2022). Some molecules trace specific physical phenomena well enough that their very detection is enough to impart information on a source. SiO, for instance, serves as an excellent indicator of shocks, such as those produced by protostellar outflows. This relationship is attributed to the sputtering of SiO from dust grains by the shocks induced by the protostellar outflow (Gusdorf et al. 2008). Other molecules and their relative abundances are useful in placing constraints on possible molecular formation mechanisms which in turn further inform us on the present and historical physical conditions of their environments.

This is all relevant as we attempt to better understand the massive star formation process. The relative chemical enrichment that we observe in star-forming regions of all masses is a direct consequence of the unique physical conditions that arise in the immediate vicinity of protostars. The cold, inert $H_2$ and CO that dominate the makeup of GMCs begin to warm up as the clumps begin to collapse under the effect of their own gravity. The warmer and denser environment that these molecules find themselves in both enables a host of reactions that cannot occur elsewhere in the interstellar medium and liberates molecules found on grain surfaces. These reactions lead to the increased gas-phase abundance of more complex molecules such as formaldehyde ($H_2CO$) and methanol ($CH_3OH$). The detection of such molecules is indicative of a hot core - an early stage of massive star formation where radiation from the protostar is responsible for heating up the surrounding medium (Helmich & Van Dishoeck 1997; Van Dishoeck 2008) - see Figure 1.2.

In order to better understand the regions in which these complex molecules are detected it is important to have a better understanding of their formation mechanisms. The reactions that form these molecules can be split into two distinct regimes: gas-phase and grain-surface reactions.

### 1.2.1 Gas-Phase and Grain-Surface Chemistry

The detection of interstellar COMs is typically conducted through their rotational emission spectra in the gas phase. For much of the time that this field of study has existed, it was believed that molecules in the interstellar medium were formed primarily through gas-phase chemistry. As models increased in complexity, those that began to more heavily incorporate chemical reactions that occurred on the surface of dust grains produced results that better matched the observed distribution of

molecules (Garrod et al. 2008). Even $H_2$, the most abundant interstellar molecule, is believed to form primarily on the surface of dust grains, though this occurs at a relatively early evolutionary stage of a GMC when the temperature is still cold enough that atomic hydrogen can be accreted onto the surface, whereupon two atoms will recombine (Cazaux & Tielens 2004).

Early theories on the formation of COMs favored their production through gas-phase ion-molecule chemistry (Herbst et al. 1977). However this was shown to be too inefficient to replicate the abundances of particular molecules observed in the interstellar medium (ISM) (Horn et al. 2004); this led to grain-surface chemistry being the favored method of formation for many molecules in recent years (e.g., Garrod et al. 2008; Garrod 2013; Linnartz et al. 2015). A number of recent laboratory and chemical modeling studies, however, suggest that gas-phase reactions may indeed be non-trivial formation pathways for COMs, particularly in cold environments (Laas et al. 2011; Balucani et al. 2015; Skouteris et al. 2018).

Much of our understanding of interstellar chemistry comes from the development of chemical models that aim to reproduce the abundances of molecules we observe in the ISM. These simulations combine the physical conditions in the early stage of star formation with an atomic and molecular inventory of species; associated with each species are parameters such as reaction rates and tendency to accrete on dust grains (Garrod et al. 2008). As time in the simulation progresses, the physical conditions change to match the evolution of the protostellar object and this in turn affects the likely reactions in the model and the formation rates of molecules - see Figure 1.3. Other mechanisms such as reactions driven by cosmic rays are also considered (Garrod et al. 2022).

In the early stages of star formation, the ambient temperature is so low that only

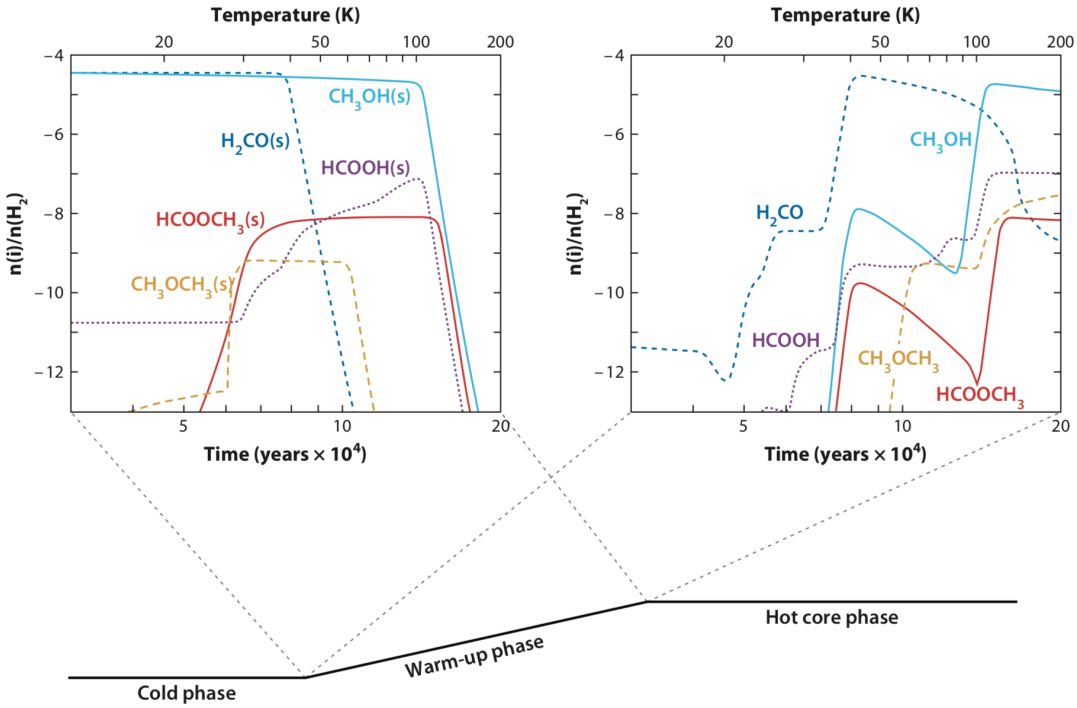


Fig. 1.3.— The solid-state (left) and gas-phase (right) abundances of various molecules in a chemical model at various stages in the star formation process. The desorption of these molecules from grain surfaces due to higher temperatures drastically increases their gas-phase abundances and their detectability in the radio regime. This figure originally appeared in Herbst & Van Dishoeck (2009), where it was adapted from Garrod & Herbst (2006).

exothermic reactions can occur as energy barriers for endothermic reactions cannot be overcome. The microscopic ($\sim$ 1 micron) dust grains that can be found in GMCs serve an important role in enabling such chemical reactions. There are three mechanisms by which reactions can occur on the grain surface: Langmuir-Hinshelwood, Eley-Rideal, and hot atom. Figure 1.4 is a graphical representation of all three of these mechanisms.

In the Langmuir-Hinshelwood mechanism, a reactant diffuses across potential minima along the grain surface by overcoming the barrier $E_b$ between sites or quantum tunneling. Once it meets another reactant in the same potential minimum, the two

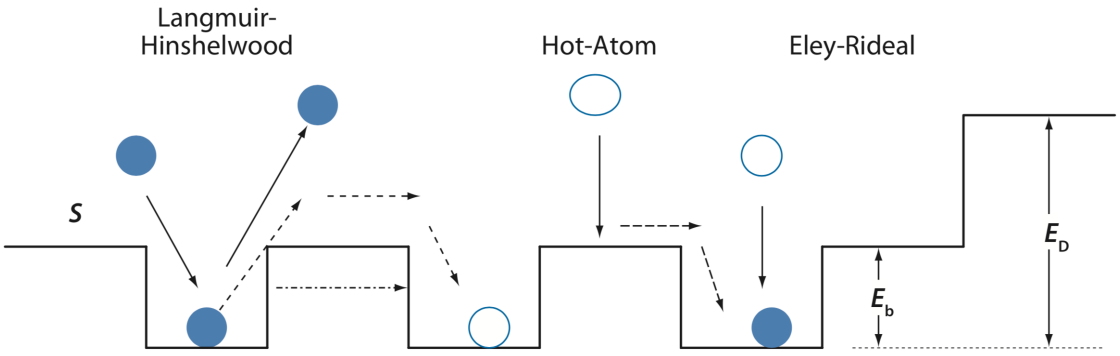


Fig. 1.4.— A grain surface with sticking efficiency $S$ and desorption energy $E_d$ possesses a number of potential minima that all have a (smaller) barrier of $E_b$. This figure originally appeared in Herbst & Van Dishoeck (2009).

may combine to form a new molecule. In the Eley-Rideal mechanism, a gas-phase reactant lands on the grain surface and immediately reacts with an atom or radical that was already present on the grain surface. In the hot atom mechanism, a gas phase reactant is accreted onto the grain surface and jumps between several minima before finding another species to react with.

## 1.3 Applying Astrochemistry to Star Formation

### 1.3.1 Measuring Chemical Abundances

Technological advancements in telescope instrumentation allowing for wider bandwidths and higher sensitivities have played a huge role in aiding astronomers' goals of understanding the cosmos. Thanks to facilities such as the Atacama Large Millimeter/submillimeter Array (ALMA), obtaining high-resolution spectroscopic observations of distant star-forming regions has become almost routine. Obtaining this data is not the end goal, however; the next step is to translate the observed intensities into physical quantities that describe the conditions in these regions. To do this we begin

with an equation relating the molecular column density and excitation temperature (both of which are unknown quantities) to a set of known or observable quantities (Turner 1991):

$$\frac{N_U}{g_U} = \frac{N_{tot}}{Q(T_{ex})} e^{\frac{-E_u}{T_{ex}}} = \frac{3k \int T_{MB} dV}{8\pi^3 \nu S \mu^2} \tag{1.1}$$

where $N_U$ is the number of molecules in the upper energy state, $g_U$ is the upper state degeneracy, $Q(T_{ex})$ is the partition function of the molecule at a given excitation temperature, $E_U$ is the upper state energy of the emission line, $k$ is Boltzmann's constant, $\nu$ is the frequency of an emission line, $S$ is the intrinsic line strength, $\mu$ is the permanent dipole moment, and $\int T_{MB} dV$ is the integrated main beam temperature. Once several emission lines from a single molecule have been observed, we can begin to solve for $N_{tot}$ and $T_{ex}$ using a method known as a rotation diagram (Goldsmith & Langer 1999). Plotting the quantity on the right hand side as a function of the upper state energy for each transition theoretically yields a straight line where the slope is inversely proportional to the temperature, $\frac{-1}{T_{ex}}$, and the column density $N_{tot}$ can be solved from the y-intercept - see Figure 1.5. Proper use of this equation requires that the molecule in question is adequately described by a single excitation temperature, that the emitting source fills the beam of the telescope, and that the lines are optically-thin, though corrections can be made for the opacity. The lines that are used to construct the rotation diagram must also be unblended with lines from other molecules; in the case that a rotation diagram is being constructed for a star-forming region, the density of lines can make it difficult to identify enough properly isolated transitions.

According to Herbst & Van Dishoeck (2009), the best method for characterizing the molecular emission from star-forming regions is to first build up a physical model

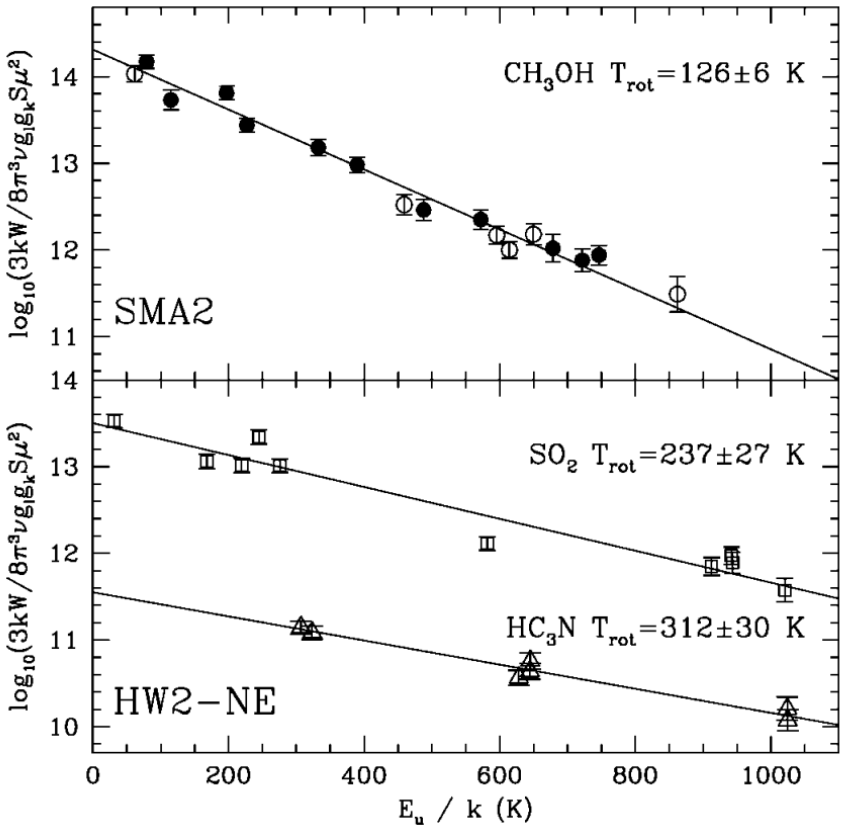


Fig. 1.5.— An example of a rotation diagram that was constructed for three molecules: $CH_3OH$ (methanol), $SO_2$ (sulfur dioxide), and $HC_3N$ (cyanoacetylene). This figure originally appeared in Brogan et al. (2007).

of the source, which then allows for proper simulation of the emission spectra from a given list of molecules that are not in local thermodynamic equilibrium (LTE). There are two issues which make such an approach difficult to apply in practice:

1. In the case that the protostellar region is in fact forming a cluster of stars - as is generally the case for massive stars - then a physical model is next to impossible to produce. In this case the gas is both intrinsically and extrinsically heated which greatly complicates efforts to measure the temperature, and even getting an estimate of the number of protostars can be a difficult task.

2. Non-LTE simulation of a molecule's emission spectra requires knowledge of a molecule's collisional coefficients - the most complex molecule for which such measurements have been made is methanol ($CH_3OH$). As emission models will often include dozens of more complex species, more work needs to be done on this front before reliable non-LTE models can be produced.

The next best method of analysis for these star-forming regions is to build up an LTE model of the molecular emission and vary physical parameters such as the temperature, velocity, and column densities to match the observations as best as possible. The vital assumption with this method is that the gas is well-mixed such that all of the observed molecules are contained within the same layer of gas - this is not likely to be entirely accurate, but some level of approximation is required to perform the analysis at all. In practice, this assumption can be seen to fall apart when especially abundant molecules such as methanol and methyl cyanide are simultaneously observed with other molecules. These abundant species - which are detected in both the inner regions of the hot core and in the colder, lower density protostellar envelope - require more creative treatments (See Section 3).

### 1.3.2 Observing Molecular Spatial Distributions

The physical conditions in star-forming regions often exhibit steep temperature and density gradients. As such, certain regions may be more conducive to formation pathways for different molecules and so it is a useful exercise to map the morphology of specific parameters for individual molecules. Ideally, the desired quantity - whether its the column density of a molecule or its velocity - would be directly measured for each pixel of a data cube in a region of interest. Building up the previously-discussed LTE synthetic spectrum to measure these quantities is a time-consuming

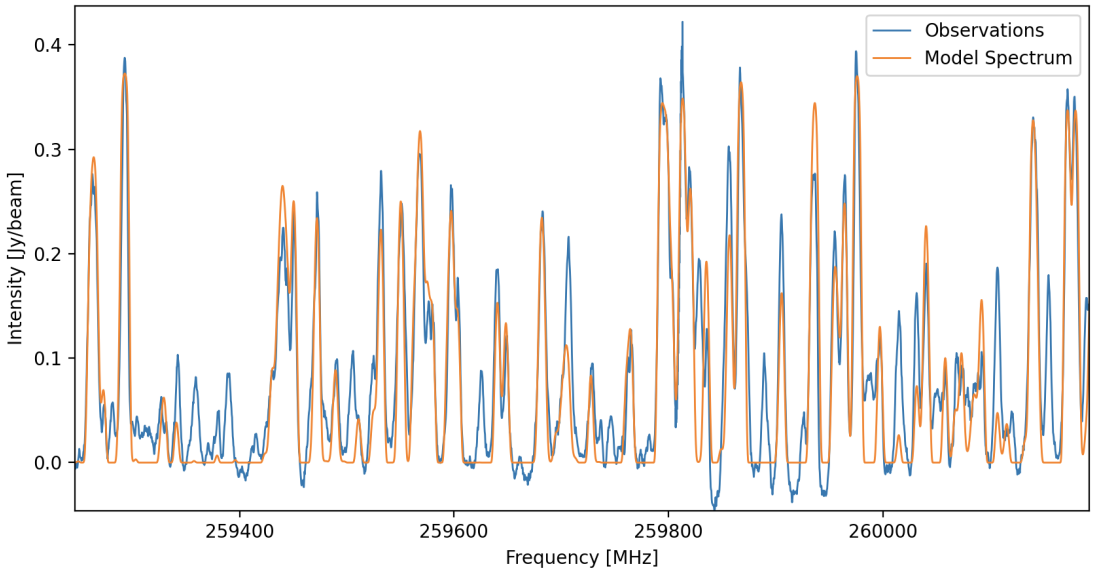


Fig. 1.6.— A sample spectrum extracted from a massive star-forming region with ALMA showcasing dozens of rotational emission lines. A simulated spectrum (orange) has been overlaid on the observations (blue).

task, however. For this reason, constructing such models is typically only done for a handful of pixels at best, and a different approach is used to characterize molecules over a large field of view.

The standard methods for analyzing the spatial distribution and kinematics of interstellar molecules over a large field of view make use of a variety of moment maps. Moment 0 maps analyze the integrated intensity of a single transition of a molecule across a given region and are often used as a proxy for the spatial distribution of the molecule. It is impossible, however, to disentangle the excitation conditions of a single transition from the physical abundance of its associated molecule using such an analysis. In regions that span a range of temperatures such as star-forming regions, this raises the question of whether we are observing a variation in the abundance of the molecule or whether we are highlighting regions where the physical conditions more readily excite a particular transition. Moment 1 maps use the intensity-weighted

velocity of a transition to generate a velocity-field and are useful for studying the kinematics of a molecule. A velocity or linewidth gradient across the field of view, however, significantly hampers the applicability of these techniques. Spectral contamination from other molecules may easily be introduced, or the emission that one is attempting to integrate may shift out of the selected channel range, though efforts have been made to mitigate these issues such as the VINE maps introduced by Calcutt et al. (2018). In quiescent regions, these concerns can be alleviated by carefully selecting a transition and channel range to isolate only the emission of interest; however, in star-forming regions with complex kinematics and molecular inventories that vary from pixel to pixel, such a task is monumentally more difficult.

Chapter 3 of this work describes my efforts to bypass the pitfalls presented by both rotation diagrams and moment maps by making it possible to efficiently make measurements of these physical parameters across thousands of pixels, regardless of the level of spectral line blending. This allows for analysis of a molecule's spatial distribution and kinematics in a manner unbiased by a select few transitions.

## 1.4 NGC 6334I

The astronomical source that is central to much of the focus in this thesis is NGC 6334I. NGC 6334, also known as the Cat's Paw Nebula, is a massive star-forming complex that houses several sites of ongoing star formation (Tigé et al. 2017), including region I (Brogan et al. 2016). What makes this source especially useful as a case study in massive star formation is its relative proximity to Earth. At a distance of 1.3 kpc (Reid et al. 2014), it is a prime candidate for study as we are able to observe the star formation on relatively small physical scales with instruments such as ALMA. The nebula is displayed in full in Figure 1.7, with region I highlighted.

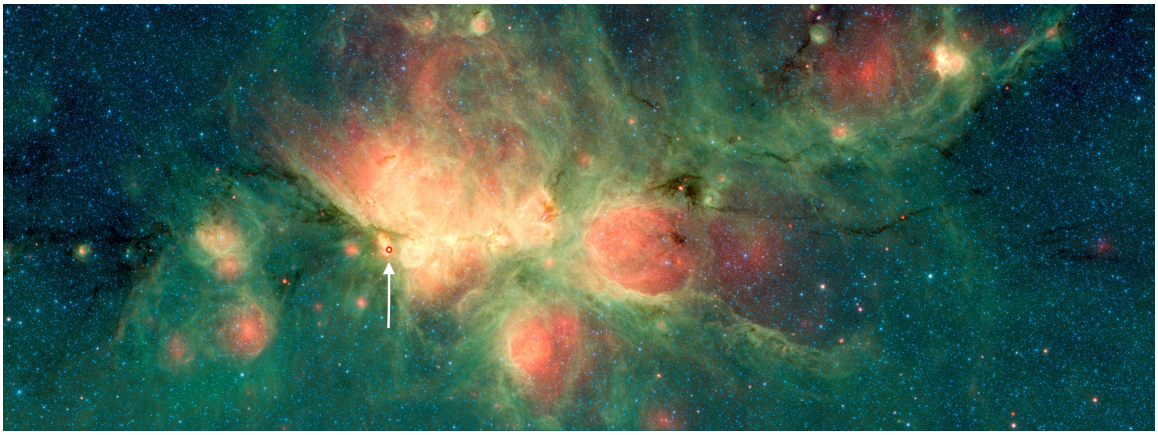

Fig. 1.7.— An infrared image of NGC 6334, the Cat's Paw Nebula. Clouds such as this serve as the birthplaces for stars. Region I is highlighted in red. Image credit: NASA.

NGC 6334I displays a rich chemistry, and with the variety in properties between different sites of star formation, serves as a vibrant astrochemical laboratory for a number of studies. A recent example is an in-depth study of the inventory of amide molecules, constraining their formation pathways and suggesting that these molecules may play a significant role as prebiotic molecular species undertaken by Ligterink et al. (2020, , including S. El-Abd). Due to its varied chemical inventory, NGC 6334I is a prime location to undertake searches for new interstellar molecules; recent species that were detected in this source for the first time include methoxymethanol (McGuire et al. 2017b, , including S. El-Abd) and methoxyethanol (Fried et al. 2024, accepted for publication, including S. El-Abd). An unsuccessful search was also carried out for interstellar $H_2CCS$ and HCCSH (McGuire et al. 2019, , including S. El-Abd), the latter of which has yet to be detected in the interstellar medium.

This source was also used in a pilot study for ALMA's Band 10 receivers which both identified additional outflow-tracing transitions of HDO and CS but also compared the emission of a much more complex molecule, glycolaldehyde, across Bands 4, 7, and 10. These spectra were compared with data observed by Herschel's HIFI

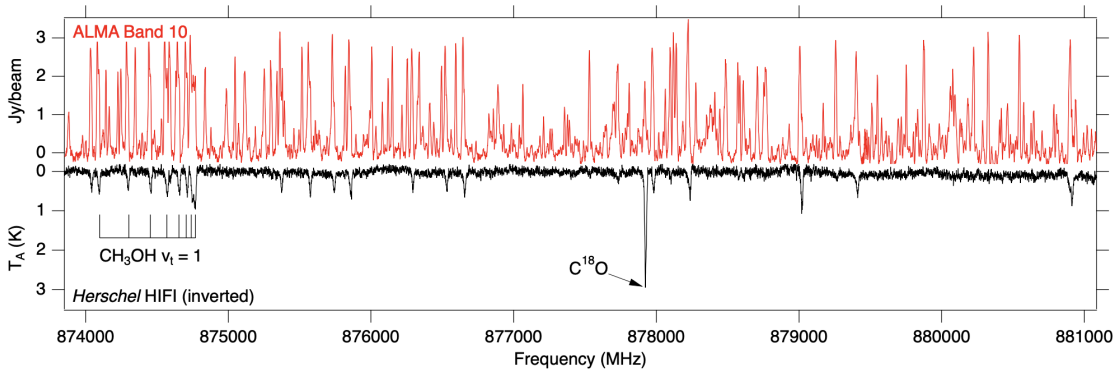


Fig. 1.8.— A comparison of the spectra observed using ALMA Band 10 (red) and Herschel's HIFI instrument (black,inverted). The increased spatial resolution of ALMA allows us to resolve many new spectral lines. This figure originally appeared in McGuire et al. (2018).

instrument in the same frequency range, showcasing both the advantages of ALMA's improved spatial resolution and the chemical diversity in NGC 6334I (McGuire et al. 2018) - see Figure 1.8.

In early 2015, the continuum emission from MM1B, a localized region within NGC 6334I, was observed to have quadrupled over the span of just a few years while the emission from neighboring regions was unchanged (Hunter et al. 2017, , see Figure 1.9). This rapid increase in the continuum emission coincided with the excitement of several new water masers (Brogan et al. 2018) and is likely evidence for an accretion outburst having occurred in the source. Unlike the recent outburst in G358.93-0.03 studied by Brogan et al. (2019), however, the observed effects in NGC 6334I did not abate; the elevated continuum levels continue to be observed in the source years later (Hunter et al. 2021, ,including S. El-Abd). As one of the few sources in which an accretion outburst from a massive protostar has been observed, NGC 6334I presents an invaluable opportunity to learn more about this elusive process.

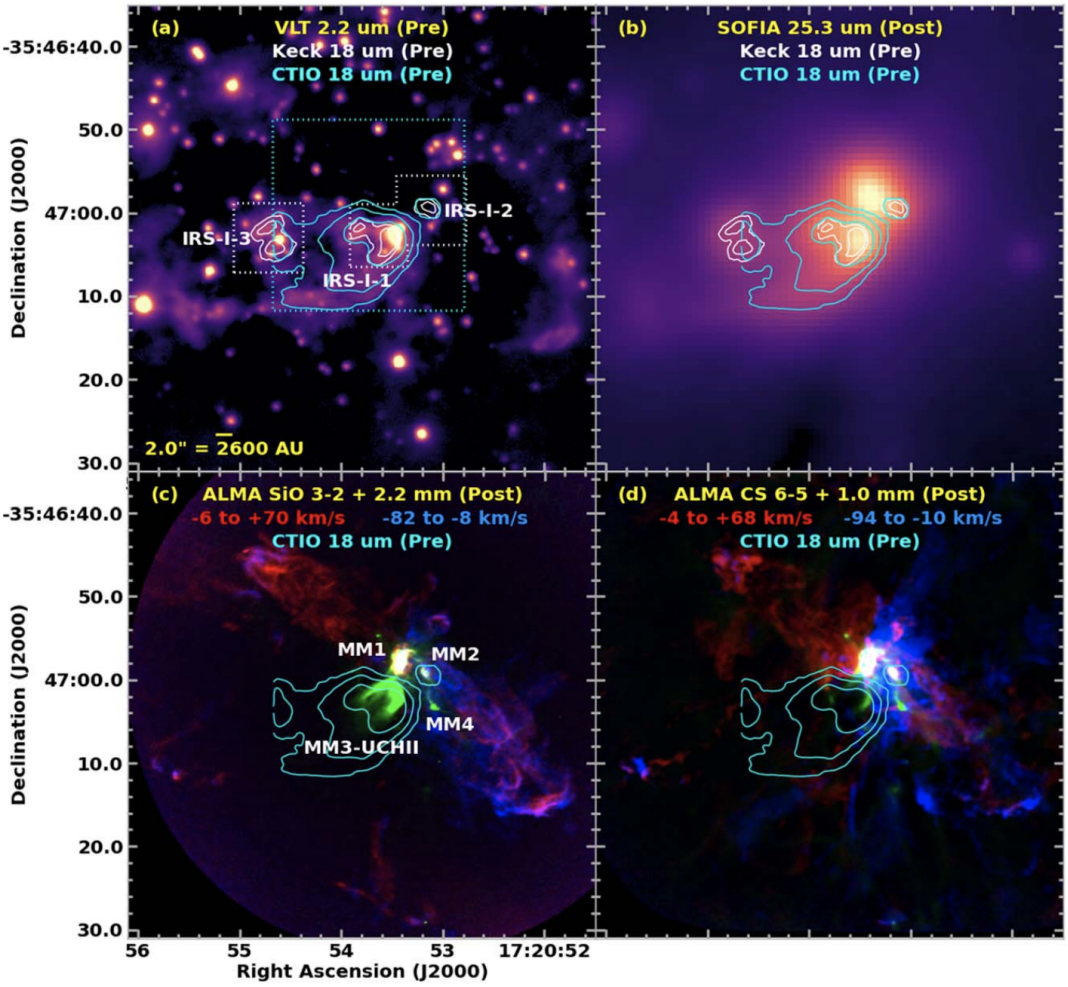


Fig. 1.9.— Comparison of the pre- and post-outburst continuum in NGC 6334I, with each colorscale image and contour labeled as pre- or post-outburst. MM1 is labeled in panel (c). The relatively redshifted and blueshifted SiO and CS transitions in (c) and (d) trace outflows driven by the outburst. This figure originally appeared in Hunter et al. (2017).

# Chapter 2

# Chemical Abundance Patterns Across Star Forming Regions

This chapter was originally published in The Astrophysical Journal in 2019 under the title *Interstellar Glycolaldehyde, Methyl Formate, and Acetic Acid I: A Bi-modal Abundance Pattern in Star Forming Regions* (El-Abd et al. 2019). It is presented here in its entirety with the exception of one paragraph from the introduction.

## 2.1 Introduction

The formation of complex organic molecules (COMs) - those species with 6 or more atoms (Herbst & van Dishoeck 2009) - is a phenomenon known to occur during the early stages of star formation. Many of the radicals that drive the production of these COMs - methyl ($CH_3$), hydroxymethyl ($CH_2OH$), and methoxy ($CH_3O$) - are produced during the photodissociation of methanol ($CH_3OH$; Laas et al. 2011). For molecules such as the $C_2H_4O_2$ isomers methyl formate ($CH_3OCHO$), acetic acid ($CH_3COOH$), and glycolaldehyde ($CH(O)CH_2OH$), the rate at which these radicals

are produced, and the relative branching fractions between their production pathways, will directly influence the relative abundance of each isomer, as well as other species containing these functional groups. Understanding the formation of the $C_2H_4O_2$ isomers is an important step to understanding the formation of yet more complex molecules that are necessary for life.

One issue that continues to plague efforts to model the production of the $C_2H_4O_2$ isomers is the overabundance of glycolaldehyde in simulations, especially relative to methyl formate which seems to be more accurately reproduced (Laas et al. 2011; Garrod 2013). With respect to the reactions forming these species from $CH_3OH$ photodissociation products, Garrod (2013) suggested the primary routes are:

$$HCO + CH_3O \longrightarrow HCOOCH_3 \tag{2.1}$$

and

$$HCO + CH_2OH \longrightarrow CH(O)CH_2OH \tag{2.2}$$

and

$$CH_3 + COOH \longrightarrow CH_3COOH \tag{2.3}$$

for methyl formate, glycolaldehyde, and acetic acid, respectively. All of these reactions are exothermic. Important to note is that while acetic acid can be produced from the photodissociation products of methanol, this is not believed to be its primary formation pathway, which is instead hydrogenation of $CH_2COOH$ on grain surfaces.

This likely implies some or all of the following possibilities:

1. the formation of glycolaldehyde via the above reaction is far less efficient than currently believed,

2. the abundances of the precursor species (primarily HCO and $CH_2OH$) are substantially different than those predicted by the models (perhaps due to incorrect branching ratios from $CH_3OH$ photodissociation),

3. there are unknown competing formation pathways that serve as sinks for $CH_2OH$, reducing the availability of this radical for forming glycolaldehyde through Reaction 2.2, or

4. there is an underlying, unaccounted for physical process that is affecting glycolaldehyde abundances that needs to be better constrained.

Adding further complexity, recent modeling of these species has suggested a number of viable gas-phase formation pathways, in addition to these grain-surface radical-radical recombination reactions (Balucani et al. 2015; Skouteris et al. 2018). Rivilla et al. (2019) study and model the HCO emission from IRAS 16293 and are able to accurately reproduce the abundance of HCO; they also posit that the dominant formation route for glycolaldehyde is the one presented here.

In this paper we perform an in-depth analysis on the abundance of glycolaldehyde, methyl formate, and acetic acid in the massive protocluster NGC 6334I (Brogan et al. 2016) by extracting spectra from a dozen positions in the cloud. We also present a systematic study of these molecules across 13 additional interstellar sources using literature data. The new data toward NGC 6334I and their analysis are described in §2.2, efforts to standardize the literature sources are presented in §2.3, and the results are presented and discussed in §2.4.

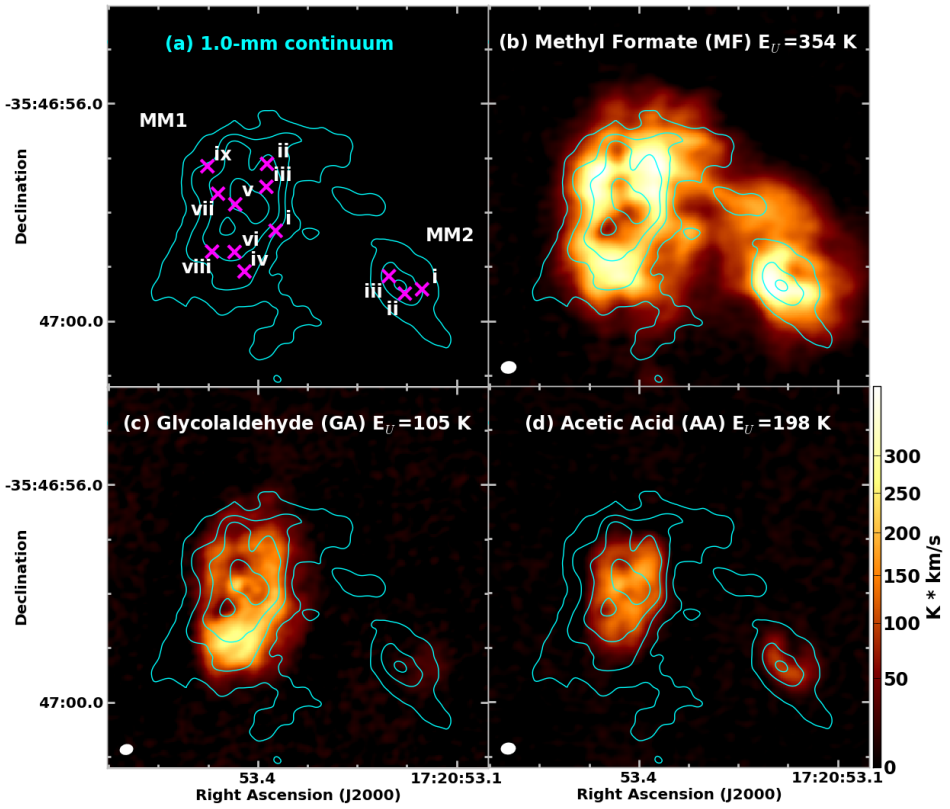


Fig. 2.1.— Panel (a) shows the locations where spectra where extracted from NGC 6334 I MM1 and MM2 (magenta × symbols and white labels) overlaid on contours of the 1 mm dust continuum (contour levels: 17.5, 52.5, 140.0, and 367.5 mJy beam$^{-1}$). See Table 2.1 for the physical conditions in each position. Panels b, c, and d show integrated intensity (moment 0) maps showing the spatial distribution of methyl formate (b), glycolaldehyde (c), and acetic acid (d) integrated from -10.4 to -2.7 km s$^{-1}$; the continuum contours from (a) are also overlaid. See Table 2.1 for a list of the position coordinates.

## 2.2 Observations & Data Reduction

### 2.2.1 Observations

The ALMA data toward NGC 6334I were observed during Cycle 3 in 2016, project code 2015.A.00022.T. The data were calibrated using the ALMA Cycle 4 pipeline (CASA 4.7.2). The observations were centered at $\alpha$(J2000) = 17:20:53.36, $\delta$(J2000)

= -35:47:00.0 and had a nominal resolution of $0.24'' \times 0.17''$ ($-83^{\circ}$), a full width half-power (FWHP) of the primary beam of $20''$, a spectral resolution of 1.1 km $s^{-1}$, and a rms per channel of 2.0 mJy $beam^{-1}$ (0.62 K). The observations consisted of two tunings, each with four spectral windows, with a bandwidth of 1.87 GHz per window. The first set of spectral windows were centered at 280.1, 282.0, 292.1, and 294.0 GHz. The second set of spectral windows were centered at 337.1, 339.0, 349.1, and 351.0 GHz. Primary beam corrections were applied to the images and the cubes were smoothed to a resolution of $0.26'' \times 0.26''$ before analysis. Further details are given in McGuire et al. (2017a), Hunter et al. (2017), and Brogan et al. (2018).

### 2.2.2 Analysis of NGC 6334I

#### Methods

NGC 6334I contains two prodigious hot core spectral line sources MM1 and MM2 (Bøgelund et al. 2018; Zernickel et al. 2012; Beuther et al. 2007). As can be seen in Figure 2.1, the morphology of the three $C_2H_4O_2$ isomers varies across each source. To account for this and get an accurate sampling of the chemistry in the cloud we extracted spectra from 9 positions around MM1 and 3 positions around MM2. We began analyzing these spectra by building a simulated model of the observed molecular line emission. We assumed a single excitation temperature and that the molecules were in local thermodynamic equilibrium (LTE). Measurement and subtraction of the background continuum from the observations were done following the methods of Brogan et al. (2018).

To verify the accuracy of the assumed $T_{ex}$, we use the formalism of Turner (1991) for molecules described by a single value of $T_{ex}$. The pertinent equations are

$$\Delta T_B = [J_\nu(T_{ex}) - J_\nu(T_{bg})](1 - e^{-\tau_0}), \tag{2.4}$$

where

$$J_\nu(T) \equiv (h\nu/k)[e^{h\nu/kT} - 1]^{-1}. \tag{2.5}$$

Here, $\Delta T_B$ is the observed brightness temperature of the line above the background continuum, $T_{ex}$ is the excitation temperature of that molecule, $T_{bg}$ is the background continuum temperature at the frequency of the transition, and $\tau_0$ is the optical depth of the line. Given a $T_{ex}$ and $T_{bg}$, the limit of $\Delta T_B$ as lines become optically thick ($\tau_0 \gg 1$) can be calculated from Equation 2.4. Alternatively, and in the case of the observations described here, if $\Delta T_B$ can be measured from optically thick lines, and $T_{bg}$ is known, $T_{ex}$ can be inferred. This analysis assumes that all molecules within the $0.26'' \times 0.26''$ beam share the same value of $T_{ex}$ (see Appendix A1 for a more complete discussion of this assumption).

Assuming the molecules can be described by a single excitation temperature, the column density ($\mathrm{cm}^{-2}$) can be determined using the formalisms outlined in Hollis et al. (2004) for a molecule described by a single $T_{ex}$ in the presence of a background continuum $T_{bg}$, and given in Equation 2.6.

$$N_T = \frac{1}{2}\frac{3k}{8\pi^3}\sqrt{\frac{\pi}{\ln 2}}\frac{Qe^{E_u/T_{ex}}\Delta T_B \Delta V}{\nu S \mu^2 \eta_B}\frac{1}{1 - \frac{e^{h\nu/kTex} - 1}{e^{h\nu/kT_{bg}} - 1}} \tag{2.6}$$

Here, $Q$ is the partition function, $E_u$ is the upper state energy (K), $\Delta T_B$ is the brightness temperature of the line above the continuum (K), converted from the measured intensity in Jy $\mathrm{beam}^{-1}$ using the Planck scale, $\Delta V$ is the linewidth (km $\mathrm{s}^{-1}$), $S$ is the intrinsic line strength, $\mu^2$ is the transition dipole moment (Debye$^2$), $\eta_B$ is the

beam efficiency, and $T_{bg}$ is the background continuum temperature (K). The partition function for each molecule was calculated through a direct summation of states as described in Gordy & Cook (1984), and includes contributions from excited vibrational states with non-trivial populations. Given a column density, this formalism can also be used to obtain a simulated, predicted spectrum of a molecule ($\Delta T_B$ for each transition with an applied Gaussian lineshape function of width $\Delta V$).

We sought to identify those transitions of methyl formate, glycolaldehyde, and acetic acid that were least blended with other molecular features. To do this, we performed a zeroth-order, by-eye fit to the data for a number of different interstellar molecules by generating simulated spectra at fixed values of $T_{ex}$, $\Delta V$, and $v_{lsr}$. In total, at least 50 molecular species, including vibrational states and isotopologues, were identified in each MM1 and MM2 extraction position. For each species, the value of $N_T$ was then varied until the best visual match between a detected molecule (typically for many transitions) and the observations was found. The spectral line properties for all of the simulated molecules were obtained from the CDMS (Müller et al. 2005b) and JPL (Pickett et al. 1998a) databases, accessible at `www.splatalogue.net`. While the exact column densities for these molecules were not derived, the simulated spectra served to identify the transitions of our target species that were the most useful for analysis (i.e. least contaminated by spectral blending with other lines). A number of spectra, including the modeled molecular spectra, are shown in Appendix A1.

Next, a least-squares optimization of the column densities of methyl formate, glycolaldehyde, and acetic acid was performed using only those lines that were identified as likely unblended, and which were seen to be optically thin (see Table 2.2). The molecular line properties of methyl formate, acetic acid, and glycolaldehyde were based on the laboratory works of Ilyushin et al. (2009), Ilyushin et al. (2013), and

Carroll et al. (2010), respectively, and previous work referenced therein.

### Exploring the Parameter Space of NGC 6334I

The molecular emission models that we constructed for each extraction position across MM1 and MM2 serve as valuable tools with which to explore the variation in physical conditions across the two sources. None of the parameters that were used to create the emission model - $T_{ex}$, $\Delta V$, and $v_{lsr}$ - were consistent across the entire region which is indicative of the prodigious effect of protostars on their surroundings. Excitation temperatures in MM1, for instance, were found to vary between 135-285 K while the excitation temperatures in MM2 varied from 152-200 K. The background temperature (i.e. continuum brightness temperature) was also found to vary significantly across NGC 6334I; increases in excitation temperature largely tracked changes in the background continuum which varied anywhere from 26.9-192.7 K in MM1 and 21.8-58.6 K in MM2. Fit $v_{lsr}$ values spanned a range of 3.8 km s$^{-1}$ in MM1 and 1.2 km s$^{-1}$ in MM2 which demonstrates the complex bulk motions of the gas in the source. The linewidths in MM2 were able to be consistently fit at 2.80 km s$^{-1}$ while in MM1 they varied from 3.00-4.50 km s$^{-1}$. For a full breakdown of the measured physical conditions in each region, refer to Table 2.1.

## 2.3 Literature Sources

For our comparison of the $C_2H_4O_2$ isomers, we compiled a list of star-forming regions for which the column density of methyl formate was known and at least an upper limit was available for the column density of glycolaldehyde. Values for the column densities of methyl formate, acetic acid, and glycolaldehyde in the literature are presented here unchanged from the original analysis with few exceptions, detailed in Table 2.3. For

Table 2.1: Physical Parameters for Spectra Extraction Locations in NGC 6334I

| Region | RA | Dec | $T_{ex}$ | $T_{bg,Low}$ | $T_{bg,High}$ | $v_{LSR}$ | $\Delta V$ |
|---|---|---|---|---|---|---|---|
| | hh:mm:ss | dd.mm.ss | (K) | (K) | (K) | (km s$^{-1}$) | (km s$^{-1}$) |
| MM1-i | 17:20:53.373 | -35.46.58.341 | 135 | 26.9 | 31.3 | -7.0 | 3.25 |
| MM1-ii | 17:20:53.386 | -35.46.57.112 | 175 | 79.7 | 94.6 | -5.0 | 3.25 |
| MM1-iii | 17:20:53.387 | -35.46.57.533 | 225 | 108.2 | 129.7 | -5.2 | 3.00 |
| MM1-iv | 17:20:53.420 | -35.46.59.088 | 150 | 38.4 | 44.8 | -8.2 | 4.50 |
| MM1-v | 17:20:53.434 | -35.46.57.856 | 285 | 159.3 | 192.7 | -4.4 | 3.25 |
| MM1-vi | 17:20:53.435 | -35.46.58.731 | 190 | 77.6 | 88.6 | -7.0 | 3.25 |
| MM1-vii | 17:20:53.460 | -35.46.57.661 | 185 | 96.5 | 112.4 | -4.8 | 3.00 |
| MM1-viii | 17:20:53.469 | -35.46.58.724 | 150 | 57.1 | 64.7 | -6.8 | 3.00 |
| MM1-ix | 17:20:53.476 | -35.46.57.156 | 150 | 36.8 | 45.2 | -5.0 | 2.50 |
| MM2-i | 17:20:53.152 | -35.46.59.416 | 150 | 21.8 | 27.8 | -9.0 | 2.80 |
| MM2-ii | 17:20:53.178 | -35.46.59.494 | 200 | 44.4 | 58.6 | -9.0 | 2.80 |
| MM2-iii | 17:20:53.202 | -35.46.59.175 | 180 | 44.2 | 57.7 | -7.8 | 2.80 |

The background temperature of the observations varied between the lower and upper sidebands of the ALMA data.

Table 2.2: Transitions Used to Calculate Isomer Column Densities in NGC 6334I

| Source | Molecule | $J'$ | $K'_a$ | $K'_c$ | $J''$ | $K''_a$ | $K''_c$ | A/E | Frequency (MHz) | $I$ (Jy beam$^{-1}$) | $S_{ij}\mu^2$ (D$^2$) | $E_{upper}$ (K) |
|---|---|---|---|---|---|---|---|---|---|---|---|---|
| MM1-i | Methyl Formate | 24 | 3 | 22 | 23 | 3 | 21 | A | 279294.919 | 0.086 | 7.29 | 178.53 |
| | | 23 | 17 | * | 22 | 17 | * | A | 282510.849 | 0.202 | 55.80 | 354.42 |
| | | 24 | 20 | * | 23 | 20 | * | E | 294678.389 | 0.097 | 19.66 | 442.06 |
| | | 24 | 18 | * | 23 | 18 | * | A | 294769.955 | 0.184 | 56.17 | 391.75 |
| | Acetic Acid | 23 | * | 20 | 22 | * | 19 | E | 279775.7366 | 0.080 | 111.46 | 177.86 |
| | | 26 | * | 26 | 25 | * | 25 | E | 281891.4488 | 0.089 | 48.83 | 186.17 |
| | | 26 | * | 25 | 25 | * | 24 | E | 291814.6653 | 0.102 | 141.3 | 198.33 |
| | Glycolaldehyde | 25 | 3 | 22 | 24 | 4 | 21 | ... | 279230.1847 | 0.184 | 74.73 | 189.12 |
| | | 25 | 4 | 22 | 24 | 3 | 21 | ... | 282760.5619 | 0.237 | 74.86 | 189.19 |
| | | 15 | 4 | 11 | 14 | 3 | 12 | ... | 292924.2749 | 0.052 | 11.55 | 77.67 |
| | | 16 | 7 | 10 | 15 | 6 | 9 | ... | 348314.054 | 0.380 | 37.24 | 105.43 |

The transitions that were used in the least squares analysis.

the acetic acid column densities provided by Remijan et al. (2002) and Remijan et al. (2003), a correction was applied to the partition function used in those works to make it consistent with the partition function used in other sources, and by our analysis. A correction for the beam size was also made to the glycolaldehyde abundance reported in Fuente et al. (2014) for NGC 7129 FIRS 2 in order to more accurately compare with their methyl formate value. For the source G31.41+0.31, measurements of the methyl formate and glycolaldehyde column densities were available from Calcutt et al. (2014), however Rivilla et al. (2017) provide a more recent measurement with a multi-line analysis, so their value was adopted for this work. Even so, the ratio of methyl formate to glycolaldehyde abundances between the two works only differed by $\sim$20%. Errors on the column densities were generally provided in the literature. When they were not, a 30% uncertainty was assumed.

## 2.4 Results & Discussion

Presented in Table 2.3 are the compiled column densities of methyl formate, acetic acid, and glycolaldehyde for each source that was used in this analysis. The molecules span several orders of magnitude in column density, reflective primarily of the span of absolute gas number densities in these sources. Critically, however, the ratios of the molecular column densities in each source vary significantly. Rather than introduce additional uncertainty in the source-to-source comparisons by attempting to derive abundances relative to $H_2$ from yet other disparate literature studies for each source, we choose to focus our analysis on the relative behavior of the three molecules to each other. This brings with it the assumption that all three molecules are co-spatial in each observation. A more accurate approach would require a detailed, self-consistent, interferometric survey of these species from a single study.

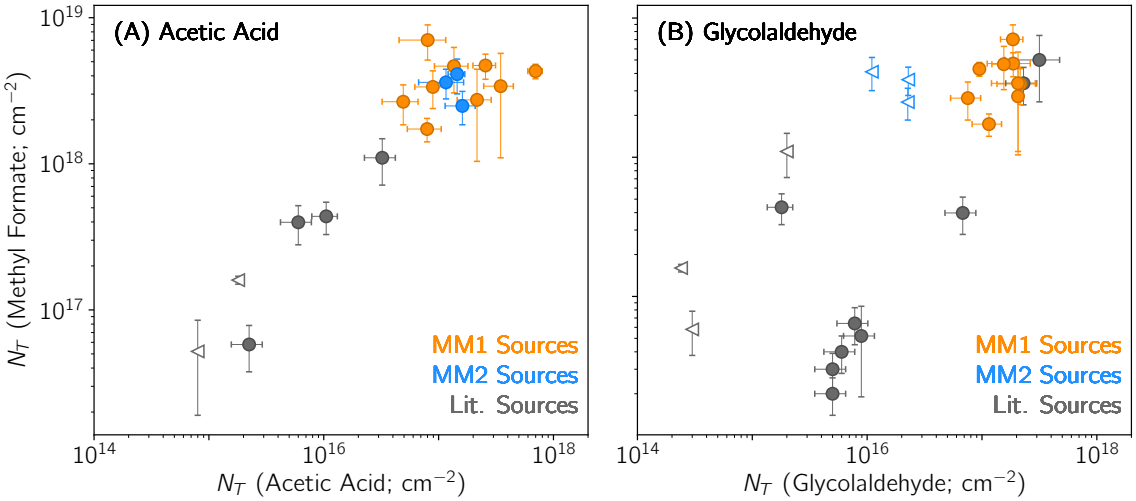


Fig. 2.2.— Scatter plots of methyl formate column density versus **(A)** acetic acid and **(B)** glycolaldehyde column densities in our sample of sources. Filled symbols are detections, open symbols are upper limits for the x-axis (see Table 2.3). Data points from MM1 are colored in orange, data points from MM2 are colored in blue, and data points from sources in the literature are in gray. There is a clear bifurcation in the GA data that does not exist in the AA data.

To test for any relationship between the isomers among the column densities provided in the literature, we plotted the column density of methyl formate as a function of the acetic acid and glycolaldehyde column densities. In the plot of methyl formate vs acetic acid (Figure 2a), the column densities increase at a similar rate. In the plot of methyl formate vs glycolaldehyde (Figure 2b), however, there is a clear bi-modal distribution in the glycolaldehyde column densities. The two trends are characterized by a number of sources with a "small" methyl formate to glycolaldehyde (MF/GA) ratio, and a number of sources with a "large" MF/GA ratio. The "small" MF/GA sources are a mixture of low and high-mass star-forming regions, while the "large" MF/GA sources are exclusively high-mass star-forming regions.

The trends shown in Figure 2.2 raise several questions about the nature of the chemistry occurring in the compiled list of star-forming regions. In the case of methyl

formate versus acetic acid, the single trend is likely a simple statement that the column densities of both species are tied to the bulk amount of gas in the cloud: i.e., “more is more."

Far more interesting is the clear demarcation in the column density of methyl formate versus glycolaldehyde in the star-forming regions. We can discern no single parameter which explains the observed differentiation. While the regions with a large MF/GA ratio are exclusively high-mass star-forming regions, there are also several high-mass star-forming regions in the group of sources with a small MF/GA ratio. This would seem to indicate that while mass is certainly an important factor in the ongoing processes of these protostellar regions, there must be some additional factor(s) that are impacting the chemistry.

That the two trends are not comprised only of sources with a specific mass means that there must be some other underlying factor through which the sources are chemically related. There was no significant trend in the excitation temperature of the sources, and there was not enough information on their ages to draw any meaningful conclusion. The inhomogeneity of the current dataset makes it an impossible task to reliably compare further properties among all of the sources. Particularly interesting is the fact that NGC 6334I-MM1 and -MM2, despite their proximity ($\sim$ 4000 au), do not share the same trend in their MF/GA ratios (being small and large, respectively). Significantly, this was consistent across all of the positions from which we extracted spectra (Figure 2.1). In a forthcoming paper (Willis et al. 2019, in prep), we examine the differentiation observed between MM1 and MM2 with a detailed physical and chemical model of NGC 6334I. This work will present a substantially updated chemical network and modelling study on all three isomers, incorporating a range of recent laboratory and theorized studies on these reactions (e.g. Shannon et al. (2013);

Skouteris et al. (2018)).

The likely implication of the bi-modal distribution is that the protostellar environment in which these molecules are forming is heavily influencing the production of glycolaldehyde, more so than the other $C_2H_4O_2$ isomers. While it cannot be ruled out completely based on current data, the other possibility is that the protostellar environment is instead affecting the production of methyl formate and acetic acid in extremely similar ways. If there were evidence for a single parent molecule that was responsible for the formation of a significant fraction of the interstellar methyl formate and acetic acid, this would be a much more attractive possibility. However, to our knowledge no such precursor is currently proposed in the literature.

Recent work by Skouteris et al. (2018) suggests ethanol ($C_2H_5OH$) is a precursor molecule for both glycolaldehyde and acetic acid. A preliminary examination regarding the abundances of ethanol, acetic acid, and glycolaldehyde in these sources did not suggest a strong correlation, but the sample size was too small to draw any concrete conclusions as only six sources had measured abundances for all three molecules.

Dimethyl ether ($CH_3OCH_3$) has been proposed as a precursor molecule to methyl formate (Balucani et al. 2015). The link between the two molecules is supported by observations of their relative abundance across a number of sources (Jaber et al. 2014), as well as their spatial distribution (Brouillet et al. 2013). The spatial distribution of the molecules is tightly correlated in NGC 6334I, and the relative abundances of dimethyl ether and methyl formate would also appear to be related in the sources used for our analysis. While there is no known process from which to form acetic acid directly from dimethyl ether, the radicals which go on to form dimethyl ether, methyl ($CH_3$) and methoxy ($CH_3O$), are direct photodissociation products of $CH_3OH$, and are thus in competition with formation routes for glycolaldehyde, methyl formate,

and acetic acid.

The difficulty of accurately reproducing glycolaldehyde abundances in chemical models may be due partly to factors that are displayed in this data. If the production of glycolaldehyde is significantly altered depending on some physical factor that was previously unaccounted for, then reproducing the proper abundances becomes a much more difficult task. Although many models are now incorporating time-dependent temperature alterations, density gradients, and even cosmic-ray-induced secondary electron processes (e.g., Shingledecker & Herbst 2018), constructing detailed physical models for each individual source is time-consuming and still involves many assumptions and simplifications. If the root cause for the dichotomy in glycolaldehyde abundances observed here is determined to be physical in nature as opposed to being a result of the atomic inventory of the regions, it is likely influencing many other molecular pathways as well. Observational determination of the cause, or at least a constraint on the possible causes, would significantly narrow the phase-space needed to be explored by models.

It must be noted that while we believe we have located a majority of the reliable literature reports of sources with at least two of these species, we are still working with a relatively small number of sources. Additionally, because the measurements of these column densities were compiled from a list of 11 different papers spanning over a decade, using many disparate facilities, and with different linear resolutions on the sky, the techniques used to measure the column densities are not self-consistent. Especially in the case of single-dish observations, there is a real possibility that the results are confused by underlying, unresolved substructure in the chemical distribution.

Nevertheless, the clear discrepancy between the glycolaldehyde and methyl formate column densities, especially when compared to the tightly-correlated acetic acid

and methyl formate column densities, strongly suggests that there is a real chemical and/or physical cause underlying these results. Most previous studies of the molecular composition of star-forming regions have either observed sources with a beam unable to resolve the source or extracted spectra from a single location within a resolved source. The best path forward is clearly a dedicated, self-consistent study of these three isomers in a much larger sample set of sources, using ALMA to account for underlying source substructure, and to ensure the observations are conducted on consistent linear spatial scales.

## 2.5 Conclusions

We have conducted a literature search and presented new observations comparing the relative column densities of the three $C_2H_4O_2$ isomers methyl formate, glycolaldehyde, and acetic acid in a total of fifteen various protostellar environments. The column densities of methyl formate and acetic acid were well-correlated, and are likely simply tracking the relative total gas mass in each source. Methyl formate and glycolaldehyde, however, display a stark dichotomy in their relative column densities. One group of sources, for which the MF/GA ratio was small, was comprised of star-forming regions with a variety of masses. The other group, for which the MF/GA ratio was much larger, was comprised entirely of high-mass star-forming regions. That the trends could not be entirely ascribed to the mass of the star-forming region suggests the existence of another parameter by which these regions can be linked. This is an excellent indicator of the stellar environment impacting the column densities of at least one of the aforementioned molecules. A dedicated, self-consistent follow-up observational study of the $C_2H_4O_2$ isomeric family, combined with chemical simulations, has the potential to constrain formation pathways for a variety of interstellar

molecules.

This paper makes use of the following ALMA data: #2015.A.00022.T. ALMA is a partnership of ESO (representing its member states), NSF (USA) and NINS (Japan), together with NRC (Canada) and NSC and ASIAA (Taiwan) and KASI (Republic of Korea), in cooperation with the Republic of Chile. The Joint ALMA Observatory is operated by ESO, AUI/NRAO and NAOJ. The National Radio Astronomy Observatory is a facility of the National Science Foundation operated under cooperative agreement by Associated Universities, Inc. Support for B.A.M. was provided by NASA through Hubble Fellowship grant #HST-HF2-51396 awarded by the Space Telescope Science Institute, which is operated by the Association of Universities for Research in Astronomy, Inc., for NASA, under contract NAS5-26555. This research made use of NASA's Astrophysics Data System Bibliographic Services, Astropy, a community-developed core Python package for Astronomy (Astropy Collaboration et al. 2013), and APLpy, an open-source plotting package for Python hosted at http://aplpy.github.com.

Table 2.3: $C_2H_4O_2$ Isomer Column Densities in Each Source

| Source | MF | GA | AA | MF/GA | MF/GA | Region Mass | Obs. | Beam | Ref. |
|---|---|---|---|---|---|---|---|---|---|
| | Column Density [$cm^{-2}$] | | | | Class. | | Type | Corrected | |
| NGC 6334I MM1-i | $1.7(3) \times 10^{18}$ | $1.2(3) \times 10^{17}$ | $8(3) \times 10^{16}$ | 15 (5) | Small | High | Int. | M | ... |
| NGC 6334I MM1-ii | $3(1) \times 10^{18}$ | $2.2(8) \times 10^{17}$ | $9(3) \times 10^{16}$ | 16 (7) | Small | High | Int. | M | ... |
| NGC 6334I MM1-iii | $3(2) \times 10^{18}$ | $2.1(8) \times 10^{17}$ | $3(1) \times 10^{17}$ | 17 (13) | Small | High | Int. | M | ... |
| NGC 6334I MM1-iv | $7(2) \times 10^{18}$ | $1.9(4) \times 10^{17}$ | $8(3) \times 10^{16}$ | 38 (13) | Small | High | Int. | M | ... |
| NGC 6334I MM1-v | $4.3(5) \times 10^{18}$ | $9.5(8) \times 10^{16}$ | $7(1) \times 10^{17}$ | 45 (6) | Small | High | Int. | M | ... |
| NGC 6334I MM1-vi | $3(2) \times 10^{18}$ | $2.1(2) \times 10^{17}$ | $2.2(7) \times 10^{17}$ | 13 (8) | Small | High | Int. | M | ... |
| NGC 6334I MM1-vii | $4.7(9) \times 10^{18}$ | $1.9(8) \times 10^{17}$ | $2.6(6) \times 10^{17}$ | 25 (11) | Small | High | Int. | M | ... |
| NGC 6334I MM1-viii | $5(2) \times 10^{18}$ | $1.6(3) \times 10^{17}$ | $1.4(4) \times 10^{17}$ | 30 (12) | Small | High | Int. | M | ... |
| NGC 6334I MM1-ix | $2.7(8) \times 10^{18}$ | $8(2) \times 10^{16}$ | $5(2) \times 10^{16}$ | 35 (15) | Small | High | Int. | M | ... |
| NGC 6334I MM2-i | $3.6(8) \times 10^{18}$ | $< 2.3 \times 10^{16}$ | $1.2(5) \times 10^{17}$ | $\geq$158.3 | Large | High | Int. | M | ... |
| NGC 6334I MM2-ii | $2.5(6) \times 10^{18}$ | $< 2.3 \times 10^{16}$ | $1.6(5) \times 10^{17}$ | $\geq$110.2 | Large | High | Int. | M | ... |
| NGC 6334I MM2-iii | $4(1) \times 10^{18}$ | $< 1.1 \times 10^{16}$ | $1.5(2) \times 10^{17}$ | $\geq$373.6 | Large | High | Int. | M | ... |
| Orion-KL | $1.6(1) \times 10^{17}$ | $< 2.4 \times 10^{14}$ | $< 1.8 \times 10^{15}$ | $\geq$667 | Large | High | Int. | M | 1 |
| Sgr-B2 (N) | $4(1) \times 10^{17}$ | $1.8(5) \times 10^{15}$ | $1.1(2) \times 10^{16}$ | 243 (85) | Large | High | S.D. | No | 2 |
| W51/e2 | $1.1(4) \times 10^{18}$ | $< 2.0 \times 10^{15}$ | $3(1) \times 10^{16}$ | $\geq$550.0 | Large | High | S.D. | Yes | 3, 4 |
| G34.3+0.2 | $6(2) \times 10^{16}$ | $< 3.0 \times 10^{14}$ | $2.2(7) \times 10^{15}$ | $\geq$193.3 | Large | High | S.D. | Yes | 3, 5 |
| G31.41+0.31 | $5(3) \times 10^{18}$ | $3(2) \times 10^{17}$ | ... | 16 (10) | Small | High | S.D. | Yes | 6 |
| G29.96-0.02 | $2.0(6) \times 10^{16}$ | $5(2) \times 10^{15}$ | ... | 4 (1) | Small | High | Int. | Yes | 7 |
| G24.78+0.08A1 | $3.0(9) \times 10^{16}$ | $5(2) \times 10^{15}$ | ... | 6 (3) | Small | High | Int. | Yes | 7 |
| G24.78+0.08A2 | $4(1) \times 10^{16}$ | $6(2) \times 10^{15}$ | ... | 7 (3) | Small | High | Int. | Yes | 7 |
| NGC 7129 FIRS 2 | $3(1) \times 10^{18}$ | $2.3(7) \times 10^{17}$ | ... | 15 (6) | Small | Intermediate | Int. | ‡ | 8 |
| IRAS 16293 | $4(1) \times 10^{17}$ | $7(2) \times 10^{16}$ | $6(2) \times 10^{15}$ | 6 (2) | Small | Low | Int. | Yes | 9 |
| L1157-B1 | $5.4(8) \times 10^{13}$ | $3.4(7) \times 10^{13}$ | $< 2.1 \times 10^{13}$ | 1.6 (0.4) | Small | Low | S.D. | No | 10 |
| NGC 1333 IRAS 4A | $5(3) \times 10^{16}$ | $9(3) \times 10^{15}$ | $< 8.0 \times 10^{14}$ | 6 (4) | Small | Low | Int. | M | 11, 5 |
| NGC 1333 IRAS 2A | $6(2) \times 10^{16}$ | $8(2) \times 10^{15}$ | ... | 8 (3) | Small | Low | Int. | M | 11 |

Please refer to §2.4 for an explanation of the MF/GA classification.
The region masses given are taken directly from the respective reference.
Int. and S.D. - Interferometer and Single-Dish, respectively.
M - These beams appear well-matched to the source size as observed, and thus no correction was made by the authors.
‡A beam correction was applied to glycolaldehyde for this work. See Appendix A1.
[1]Favre et al. (2011), [2]Belloche et al. (2013), [3]Lykke et al. (2015), [4]Remijan et al. (2002), [5]Remijan et al. (2003), [6]Rivilla et al. (2017), [7]Calcutt et al. (2014), [8]Fuente et al. (2014), [9]Jørgensen et al. (2016), [10]Lefloch et al. (2017), [11]Taquet et al. (2015)

# Chapter 3

# Streamlining the Process of Measuring Interstellar Molecules

This chapter was originally published in The Astrophysical Journal in 2024 under the title *An Automated Chemical Exploration of NGC 6334I at 340 au Resolution* (El-Abd et al. 2024). It is presented here in its entirety with the exception of one paragraph from Section 3.5.3.

## 3.1 Introduction

The energetic events associated with star formation and the clustered nature of massive protostars result in a complicated picture with respect to the kinematics and excitation mechanisms of the surrounding gas (Hunter et al. 2021; Rivilla et al. 2013). As the nascent protostars continue to evolve they heat up this gas, enabling a plethora of chemical reactions that cannot efficiently occur elsewhere in the interstellar medium (Jorgensen et al. 2020). The molecules that are formed in these unique environments are useful tools for understanding the physical conditions in which they are found.

The characteristics of their rotational line emission can be used to measure the temperature and velocity of the gas (assuming local thermodynamic equilibrium), and the relative abundances of molecules constrain their formation pathways (Herbst & Van Dishoeck 2009).

The molecular emission that arises from star forming environments is a valuable tool for constraining the physical conditions of protostellar regions, *but only in the case that this emission can be properly identified.* The reality is that spectroscopic observations in the millimeter regime are often a dense conglomeration of lines due to the high spectral line density of many molecules. This makes it a challenging task to isolate the emission from a single molecule; attaining an accurate picture of the chemical inventory for such regions requires simultaneously fitting a large number of molecules to the data to accurately model as much of the observed spectral bandwidth as possible. We are fortunate to have a number of tools such as `molsim` (Lee et al. 2023), `XCLASS` (Möller et al. 2017), `MADCUBA` (Martín et al. 2019), `CASSIS` (Vastel et al. 2015), `WEEDS` (Maret et al. 2011) and `pyspeckit` (Ginsburg & Mirocha 2011) which make it a relatively trivial process to overlay a simulated rotational spectrum of a molecule over our observations for a wide range of physical parameters. Given a wide enough bandwidth of observations, we can then be confident of a molecule's detection and characteristics if we can match the observed emission with reasonable parameters for a large number of emission lines. Individually fitting molecules to observations with a large bandwidth is a time-consuming process, however, especially if one wants to characterize the behavior of a large number of molecules. For this reason, the spectral analysis of star-forming regions is often limited to a small number of positions, if not a single one - thus leaving a wealth of information on the proverbial table. This approach is particularly problematic when applied to massive star-forming

regions, as they are often physically and kinematically complex (Brogan et al. 2007; Cunningham et al. 2023, e.g.,). Because the physical conditions vary significantly over the field of view of the observation, it is impossible to extrapolate information across the region from measurements taken over a handful of pixels with any confidence.

To address this problem, we have developed an automated least-squares fitting routine that will fit the combined spectra of a given list of molecules to every pixel in an ALMA image cube. This technique allows for a broader exploration of the physical conditions and molecular abundances surrounding massive star-forming regions and other protostellar environments by both accelerating the production of the measurements of interstellar molecular abundances and increasing the number of positions for which these measurements can be made. We have chosen ALMA data toward NGC 6334I spanning a total bandwidth of 7.48 GHz in the frequency range from 280 to 351 GHz for our initial proof of concept study. This massive Galactic protocluster hosts two extremely rich hot core line sources, each with distinct physical conditions and kinematics (see § 3.2.1 for additional details), providing ample fodder to test our fitting technique on a challenging use case. The goal of this work should be stated clearly: we are not claiming that the final fit parameters for each pixel are necessarily as accurate as those that would be derived were one to manually fit each of the molecules by hand in one of the pixels. That said, we do believe that the derived parameters are reasonably accurate for the vast majority of the pixels in our field of view. These fits - taking into account their uncertainties - provide a unique point of view with regards to the spatial morphology of complex interstellar molecules that is not biased by an *a priori* choice in the extraction location of the spectra. Massive star-forming regions are physically and kinematically complicated; the ability to take a holistic view of such regions will be a crucial step forward for understanding their

ongoing physical processes.

In this paper, the data on which the fitting routine was tested are described in § 3.2, while the fitting technique itself is described in § 3.3. Images of the excitation temperature, linewidths, and velocity measured for each of >8000 pixels across two distinct regions in NGC 6334I are presented in § 3.4, along with images of the physical column densities of the $C_2H_4O_2$ isomers. § 3.5 expands on some of the methods of analysis this technique enables, as well as how the velocity and column density images compare with their moment map counterparts.

## 3.2 ALMA Data Characteristics

### 3.2.1 Test Case: NGC 6334I

NGC 6334I contains two prodigious hot core spectral line sources, MM1 and MM2 (Beuther et al. 2007; Zernickel et al. 2012; Bøgelund et al. 2018). At a distance of 1.3 kpc (Reid et al. 2014; Chibueze et al. 2014), these two sources are separated by only ∼4000 au (see Figure 3.1, making any chemical differentiation between the two of them particularly diagnostic as it is reasonable to assume they likely formed from similar primordial material. MM1 (the brighter of the two sources) hosts at least two young protostars, MM1B and MM1D. Complicated bulk motions are evident in the source, with at least two outflows: one on a larger scale oriented NE-SW (Qiu et al. 2011) and another more compact, dynamically young outflow in the N-S direction (Brogan et al. 2018). It is currently unclear which source within MM1 is driving these outflows. MM2 (129 K continuum peak at 350 GHz) is a source with significantly lower brightness temperature than MM1 (222 K continuum peak), but MM2 is still rich with molecular line emission and exhibits much narrower linewidths

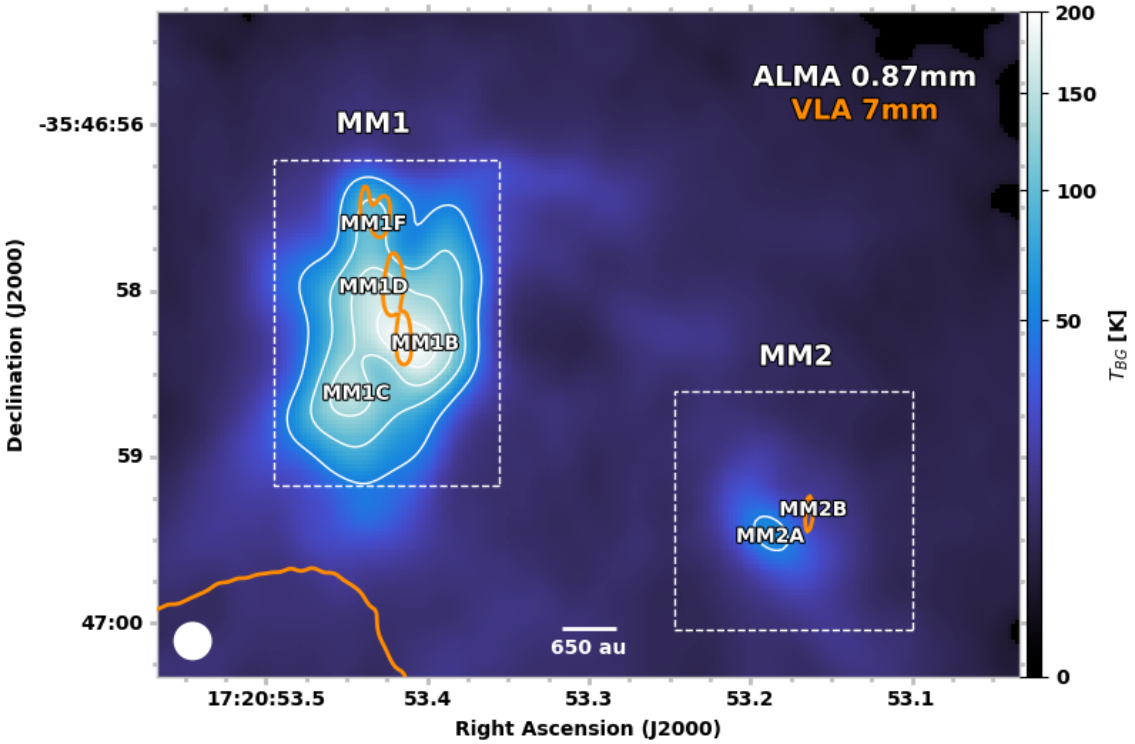


Fig. 3.1.— An ALMA 0.87 mm continuum image of the central portion of NGC 6334I showing the proximity of MM1 and MM2. The white contours denote continuum brightness temperatures of 50, 90, 130, and 170 K. The orange contours mark VLA 7 mm emission of 11 K (the contour at the southwest edge of the frame arises from MM3, Brogan et al. 2016). The dashed boxes highlight the regions over which we ran the automated fitting routine.

(see Figures 3.6 and 3.7).

NGC 6334I-MM1 has recently undergone an accretion outburst in 2015 (MacLeod et al. 2018; Hunter et al. 2017). Accretion onto young stellar objects is an avenue by which stars are believed to gain a significant portion of their final mass (Fischer et al. 2019, 2022). While this mechanism has long been associated with low-mass star formation, recent observational and theoretical evidence indicates this mechanism occurs in massive star formation as well (Garatti et al. 2017; Hunter et al. 2021; Meyer et al. 2021). Such accretion may occur rapidly in discrete episodes as opposed

to a steady process that takes place over a longer stretch of time. These episodes are also responsible for energetic outflows driven through the surrounding cloud, raising the level of continuum emission as well as driving maser emission. In NGC 6334I-MM1, the continuum emission quadrupled in intensity and coincided with a rapid increase in the maser emission observed from the source. Both effects are still visible six years after the event (Hunter et al. 2017, 2021). It is highly likely that these energetic events serve as the impetus for a variety of unique chemical reactions across the region in question. Attaining a better understanding of this unique, complex environment is not feasible through the analysis of a small handful of positions. A new approach is required to be able to understand the entire breadth of the physical conditions and their associated molecular products.

### 3.2.2 Observations

The ALMA data toward NGC 6334I used for this study were observed during Cycle 3 in 2016, under project code 2015.A.00022.T. These are the same data used in El-Abd et al. (2019) but have since been reprocessed with the ALMA Cycle 8 pipeline (version 6.2.1-7-pipeline-2021.2.0.128, Hunter et al. 2023) to account for an ALMA renormalization issue that can affect the flux scaling of strong spectral lines[1]; these corrections were found to be of order 10% for the most affected transition, CS (J=6-5), and much lower to undetectable for the majority of transitions arising from complex organic molecules.

The observations consisted of two tunings, each with four spectral windows, with a bandwidth of 1.87 GHz per pair of windows. The first set of spectral windows were centered at 280.1, 282.0, 292.1, and 294.0 GHz. The second set of spectral windows

[1]see https://help.almascience.org/kb/articles/what-errors-could-originate-from-the-correlator-spectral-normalization-and-tsys-calibration

were centered at 337.1, 339.0, 349.1, and 351.0 GHz. Both tunings were taken with a factor of 2 online channel averaging producing a channel width of 976.6 kHz; the spectral cubes were made with a channel width of 1.1 km $s^{-1}$, comparable to the effective spectral resolution. The observations were centered at $\alpha$(J2000) = $17^h$:$20^m$:$53^s$.36, $\delta$(J2000) = -35°:47′:00″.0 and the images were created with CASA (The Casa Team et al. 2022) using `robust` image weighting values of 0.2 and 0.5 for the lower and higher frequency tunings, respectively. The resulting angular resolution of the images was a bit less than 0.″26 (the beam was oversampled by a factor of 5 relative to the minor axis of the synthesized beam). The data were self-calibrated using the bright continuum emission, and the solutions were also applied to the continuum-subtracted line data; the continuum subtraction was performed as described in Brogan et al. (2018). The full width at half-power (FWHP) of the primary beam is $\sim 20''$ and the images were corrected for the primary beam response. The cubes were smoothed to a uniform circular angular resolution of 0.″26 before analysis with an rms noise per channel of 1.8 mJy $beam^{-1}$ for the lower tuning and 3.0 mJy $beam^{-1}$ for the upper tuning.[2] Further data processing details are given in McGuire et al. (2017b), Hunter et al. (2017), and Brogan et al. (2018).

[2]The rms noise measurements were made in line-free channels of the data cube at several positions between the 0.8 and 0.6 primary beam response annulus; a further distance from the phase center than either MM1 or MM2. These are conservative estimates because the noise is not uniform in the maps corrected for the primary beam response; the noise level increases with distance from the phase center.

## 3.3 The Fitting Routine

### 3.3.1 Technique

`molsim` is a publicly-available Python package tailored for the analysis of high spectral resolution spectroscopic observations of astronomical sources. The use of this package, or others like it, enables astronomers to match the rotational spectra of molecules measured in the lab to observations made of the ISM and in turn derive physical parameters from those observations. This package has already been used to great effect across a number of different studies ranging from single-dish observations of a dark molecular cloud (McGuire et al. 2020) to interferometric surveys of massive star-forming regions (Schuessler et al. 2022; Remijan et al. 2022). In tests comparing similar Python packages, Ginsburg et al. (2022) found that the simulations produced by `molsim` were in good agreement with those produced by `XCLASS` and `pyspeckit`.

In addition to telescope- and source-specific parameters, for each molecule we derive values for excitation temperature ($T_{ex}$), linewidth ($\Delta V$), velocity ($v_{LSR}$), and column density ($N_T$) by forward-modeling the spectra of each species and performing a least-squares fit of the combined spectra across the entire frequency range of the observations. For our treatment of NGC 6334I, we made the assumption that all of the molecules in the model share a single excitation temperature, linewidth, and velocity for each pixel while we allow the column density to vary on a molecule-by-molecule basis. We discuss the robustness of each of these assumptions in detail later. In the case of $T_{ex}$ specifically, this assumption is required in order to properly account for optical depth corrections when lines of different species overlap with one another. As many of the spectral lines in our observations are at least modestly optically thick, a full radiative transfer analysis would be needed in order to simulate contributions

from molecules at more than one excitation temperature, which is not possible in the current version of `molsim`.

While our initial goals were to use a least-squares minimizer - specifically, the bounded limited-memory BFGS algorithm (Zhu et al. 1997) - to find all of the relevant parameters for simulating the molecules, the nature of the spectra we were attempting to fit meant we were left with less than satisfactory results in pixels that had a particularly bright continuum or showed substantial absorption signals. For our specific test data on NGC 6334I near 300 GHz, which exhibits both very high dust continuum and high line opacity for abundant molecules, as well as a fairly extreme level of line blending, we found that it would be better to make independent measurements of the excitation temperature and linewidth for each pixel and rely on the minimizer to fit the velocity and column densities.

The excitation temperature is measured by assuming the brightest lines in our spectral range are optically thick (see Figure 3.2). From this, it follows that we can directly solve for the excitation temperature adopting the formalism of Turner (1991):

$$\Delta T_B = [J_\nu(T_{ul}) - J_\nu(T_{bg})][1 - \exp(-\tau)] \tag{3.1}$$

where the source is assumed to fill the beam, $\Delta T_B$ is the intensity of a single transition, $T_{ul}$ is the excitation temperature, $T_{bg}$ is the background temperature (measured from the continuum image of each spectral window), $\tau$ is the opacity, and

$$J_\nu(T) = (h\nu/k)[\exp(h\nu/kT) - 1]^{-1}. \tag{3.2}$$

Assuming $\tau >> 1$ and rearranging the equations to solve for $T_{ul}$ per pixel, hereafter referred to as $T_{ex}$, we have

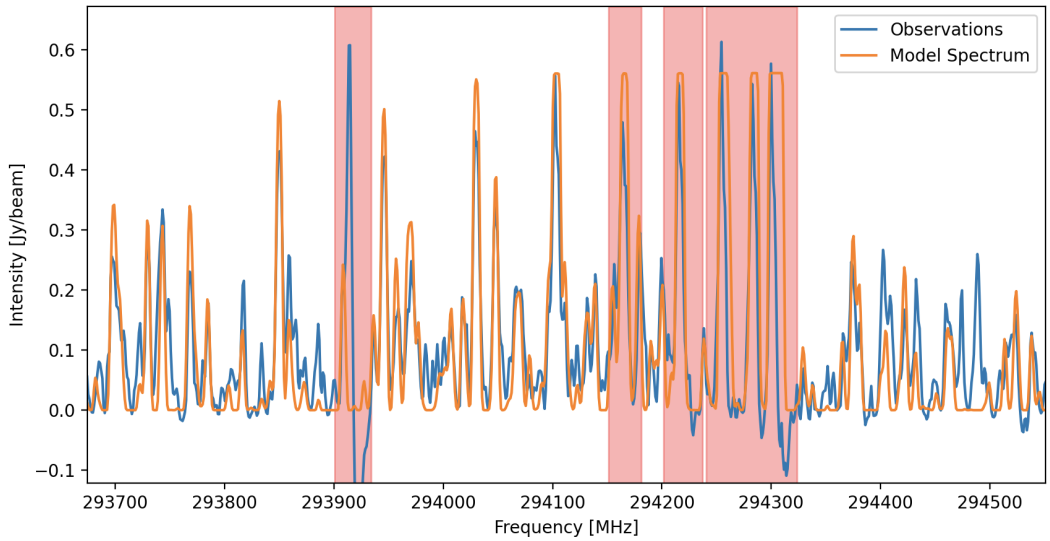


Fig. 3.2.— A sample spectrum extracted from MM1 (blue) with a simulated emission spectrum using fitted parameters from the routine (orange) overlaid. The channels highlighted in red either contain emission from a molecule used exclusively for masking purposes (such as at 293900 MHz), or contain emission from a molecule included in the model where the particular transition falls below the upper state energy threshold criteria - such lines are likely both optically thick and significantly impacted by absorption. These highlighted channels are excluded from the data used by the fitting routine in any capacity. See Section 3.3.3 for a more detailed explanation.

$$T_{ex} = \frac{h\nu/k}{\ln\left(\frac{h\nu}{k(J_\nu(T_{bg})+\Delta T_B)} + 1\right)}. \tag{3.3}$$

The adopted value for $\Delta T_B$ is found by computing the mean intensity, $I$, of all $N$ channels within 5% of the peak intensity (from any line) for each pair of spectral windows (there are two spectral windows per sideband, two sidebands per tuning, and two different tunings) using the following equations:

$$\begin{aligned} \Delta T_B &= \overline{\Delta T}_{Bspw} \\ \Delta T_{Bspw} &= \frac{\sum_{j=1}^{N} I_j}{N} \end{aligned} \tag{3.4}$$

In the case of deviations from our assumption of a well-mixed, homogeneous gas

parcel, the temperature derived from the optically thick lines may not perfectly represent those of the optically thin lines for a given species. We expect any such deviations to be small, and indeed find that the excitation temperatures derived from our optically thick lines result in fits to the optically thin lines well within expected uncertainties. The linewidth for each pixel is found by first running a spectral peak-finding algorithm across the entire frequency range of our observations, excluding any peaks below $10\sigma$ (see Section 2.2.1 for a description of the noise measurement). A Gaussian is fit to each of these spectral peaks and the resulting FWHM values are binned in a histogram. Another Gaussian is fit to the histogram itself, with the central value of this final Gaussian adopted as the canonical linewidth for the pixel in question. Although the linewidth of any particular transition may be heavily affected by spectral line confusion, the ensemble is largely insensitive to this effect given the large number of fitted transitions - see Figure 3.3. Visual inspection of the fits and examination of residuals in numerous spectra show that the values extracted from this procedure indeed robustly describe the vast majority of spectral lines.

Once the excitation temperature and linewidth have been measured, the fitting itself begins with a single pixel on the image with every molecule initialized to the same column density. Once the velocity and column densities have been measured, the same process is carried out for the pixel directly to the north, with the velocity and column densities from the previous pixel used as the starting parameters. This process is continued until the entire column has been fit (see Figure 3.4). Scripts are then launched in parallel that each use one of the pixels in this first column as a starting point and then moves across the rest of the corresponding row in the image. Using scripts in this fashion allows us to maintain the workflow of using the parameters from previous pixels as the starting point for the next fit while greatly

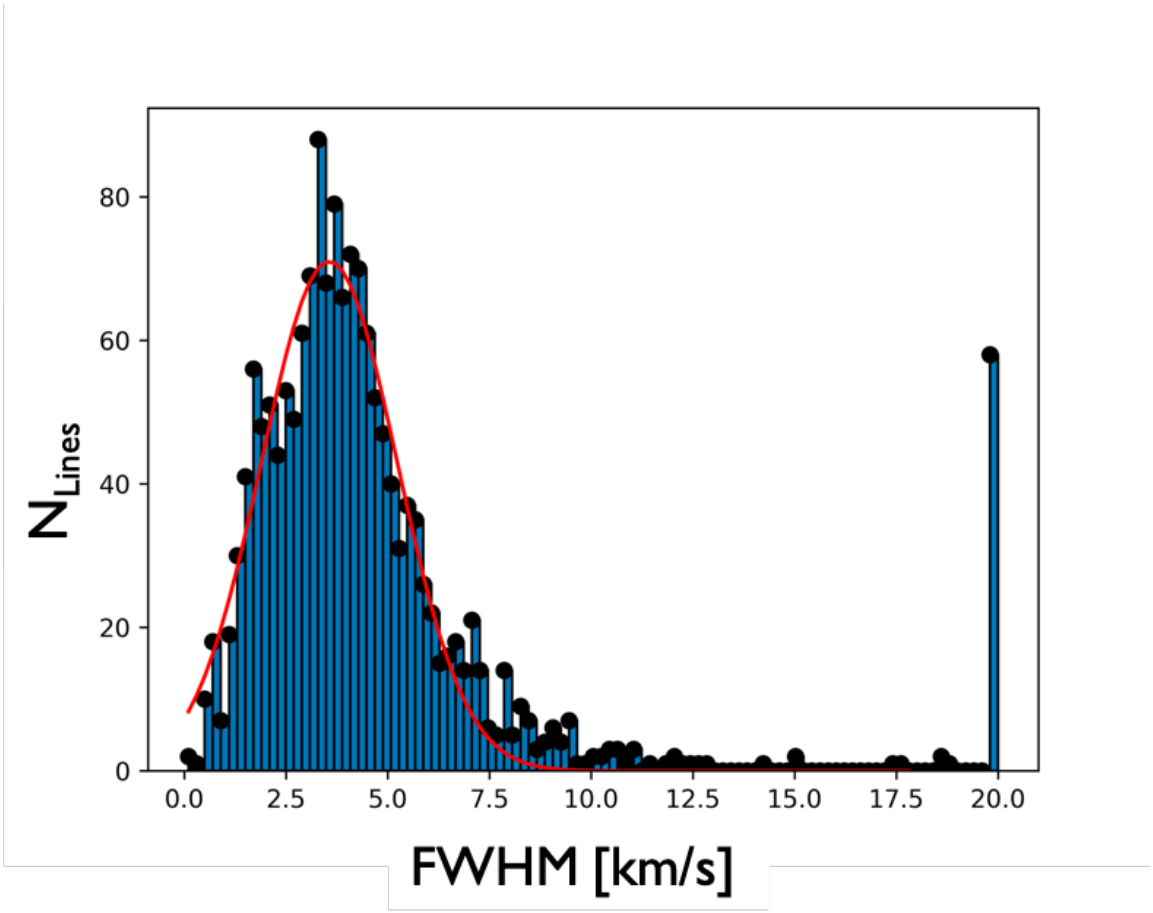


Fig. 3.3.— An example of the Gaussian fit to a histogram of FWHM values fitted for all transitions $> 10\sigma$ from a single pixel (blue). The adopted value for the linewidth of a given pixel is taken from the central value of the fitted Gaussian (red line). The large value of $N_{Lines}$ for the highest velocity bin ($\sim$ 20 km s$^{-1}$ for this example) is a consequence of the peak-finding algorithm fitting a single Gaussian to the many blended line features in the data and includes any fitted FWHM $\geq$ 20 km s$^{-1}$.

decreasing the necessary computation time.

The minimization process is dramatically accelerated by the use of boundary conditions on the allowed values explored by the minimizer for each parameter. The flexibility on the bounds were carefully selected while balancing two factors: capturing the spread in physical parameters across NGC 6334I and a desire to make things more computationally efficient. In this case, we are aided by the assumption that the physical parameters should not vary dramatically (orders of magnitude) between pixels. Thus, we are able to set boundary conditions such that neighboring pixels should not differ significantly from one another.

For the results presented in this work, the velocity was allowed to vary by $\pm$ 1.0 km s$^{-1}$ from pixel-to-pixel, while the column density for each molecule was allowed to vary by $\pm$ 0.4 dex - these bounds were centered on the fitted value from the previous pixel in the fit. While this methodology for setting the bounds works for the vast majority of pixels in our images, a poor fit in one pixel has the potential to adversely affect the fit in the subsequent pixel - see Section 3.3.5 for a discussion of where this might have impacted our results.

### 3.3.2 Molecules Included in the Model

The results presented in this work are the product of a best-fit synthetic emission model containing rotational spectra from 21 different molecules. Regarding which species to simulate, the molecules included in the models of El-Abd et al. (2019) served as the starting point, with molecules added and removed as we explored the capability of the automated fitting method (see Table 3.1 for the complete list). Several of the molecules initially included with the model had a relatively small number of transitions in the frequency range of our observations. Due to the small number of

data points that the minimizer was working with - and more importantly, the overall number of available *unblended* transitions - the fit parameters for these molecules were poorly constrained relative to the other molecules.

Due to the poor fits in some regions for these molecules, we conducted another run of the fitting routine that was identical in every way except for the exclusion of these molecules. This run produced best-fit parameters for the remaining molecules that were well-matched to the previous results, indicating that the inclusion of a handful of poorly-constrained molecules does not negatively impact the fitting of the other molecules in our model. However we continued to exclude these molecules from future runs of the fitting routine as their inclusion drastically increased the required computation time. This increase was likely due to their minimal contributions to the final emission model over a wide range of parameters, meaning that a larger parameter space was being explored for each of these molecules. As these molecules did still have emission in a significant number of pixels in our field of view, channels that contained any of their emission were excluded from the fit.

While the 21 molecules that we included in the fitting routine cover a significant amount of the spectral emission, there are still a number of lines that can be attributed to molecules that are not included, or are otherwise unidentified. This result is within expectations - the goal of this initial pass was to fit the bulk of the emission in as efficient a manner as possible with molecules of interest.

### 3.3.3 Exclusion of Channels

We quickly found that we could not simply start the code and leave it with nothing but the minimization function to guide it. NGC 6334I is a kinematically complicated source with a number of outflows and a bright continuum (Brogan et al. 2018);

these properties cause effects in the spectra that make their simulations much more challenging. The key was figuring out how to identify the channels in our observations that exhibited significant absorption from molecular transitions with $E_{up} \ll T_{bg}$ or other such effects that we are currently incapable of modeling appropriately and excluding them from the fit.

The primary solution was to use an upper state energy exclusion threshold that is applied to problematic molecules included in the model - methyl cyanide and formamide in our case. These molecules are extremely abundant and have many intense lines in the frequency range of our observations. Many of these transitions have low upper state energies - such transitions are easy to excite and are prone to displaying absorption effects due to an intervening colder layer of molecules along our line of sight. There is also the matter of the absorption of these low-lying transitions against the bright continuum - this effect is more pronounced as the continuum level increases. These phenomena allow us to use the background temperature as a measure of which lines we can safely include in our simulations to fit. The exclusion threshold is dependent on the mean background temperature at that pixel (measured for each of four spectral windows), and excludes any channels of the observation from being fit if they are contaminated with emission from transitions with an upper state energy below the threshold (see Figure 3.2 for a demonstration). While the implementation of this threshold alleviated the opacity issue, there are still instances where the results of the fitting routine appear to be unphysical - see Figures 6.27 and 6.32 in Appendix A2. The depression around MM1D is a likely consequence of the complex kinematics in that particular region, with visible evidence for multiple velocity components for some molecules. This effect appears to be more pronounced for molecules with higher column densities.

Methanol is an especially problematic molecule to fit in NGC 6334I. In the frequency range used for the study, the vibrational ground state of methanol ($v_t$=0) is dominated by relatively low $E_{up}$ transitions that are optically thick; this is true to a large degree even for the $v_t$=1 transitions. Thus, methanol required a separate solution - splitting the catalog into separate vibrational states such that we only attempted to fit the $v_t = 2$ transitions, as fitting the $v_t = 0, 1$ transitions was an impossible task for most of the pixels in this source due to their significant opacity and consequent absorption effects. All of the $v_t = 0, 1$ transitions were used to exclude channels from the observations as above regardless of their upper state energy. As with methyl cyanide and formamide, there appear to be regions that are difficult to get a handle on the methanol parameters, with MM1D again highlighted (Figure 6.25). For each of these molecules, and even less abundant molecules like methyl formate, the 13C isotopologues are certainly a more reliable representation of their spatial morphologies.

Additionally, a handful of molecules such as $H_2CO$ and CS were present in our observations but had few to no unblended transitions that were also unaffected by significant absorption effects. The simulated emission from all of the transitions of these molecules was used to exclude additional channels from the observations (see Section 3.3.2 for the criteria for including a molecule in the model and Table 3.1 for a complete list of molecules). All of these methods of treating the emission from various molecules not only improved the fits for the affected molecules like methyl cyanide and formamide, but also improved the fits for many of the other molecules included in the model.

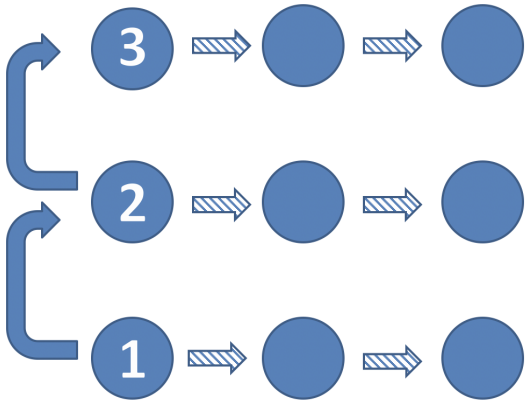


Fig. 3.4.— Diagram showing the path of the fitting routine in MM1 on a sample 3x3 image. The final fit parameters for one pixel are used as the starting parameters for the next pixel as denoted by the arrows. The dashed arrows denote the subsequent stage of fitting.

### 3.3.4 Uncertainties

The uncertainties in the values produced by the fitting are estimated through the propagation of uncertainties in the fundamental measurements with the exception of the linewidth, $\Delta V$. Spatial maps of the uncertainties for each parameter can be found in Appendix A2.

#### Excitation Temperature

The two relevant quantities in Eq. 3.3 for measuring the uncertainty in the excitation temperature are $\Delta T_B$ and $T_{bg}$. The rms noise for both of these quantities were measured and this uncertainty was propagated through the equation for excitation temperature for each spectral window; the values for each spectral window were added in quadrature. An additional factor of 10% of the final fitted value was

added in quadrature with the final rms noise value to account for the absolute flux calibration uncertainty (Cortes et al. 2023).

### Linewidth

The uncertainty in the linewidths is taken directly from the uncertainty automatically calculated by the `lmfit` package used for the Gaussian fit to the histogram in Figure 3.3.

### $\mathbf{V_{LSR}}$

The uncertainty in the central value of a Gaussian can be approximated with the following equation (Campbell 2018)

$$\sigma_c = \frac{\sqrt{FWHM\Delta\nu}}{SNR} \tag{3.5}$$

where $\Delta\nu$ is the channel width of the observation. From this, the uncertainty in our fitted velocity is the root mean square of $\sigma_c$ scaled by the number of transitions used to constrain the velocity.

$$\sigma_{V_{LSR}} = \frac{\sqrt{\sum_{j=1}^{N} \frac{\sigma_{cj}^2}{N}}}{\sqrt{N}} \tag{3.6}$$

It should be stated that the uncertainty for the velocity given in this work is *not the uncertainty in the velocity for any single molecule in our model.* Rather, it is the uncertainty of the single best-fit velocity for the *ensemble* of included molecules.

**Column Density**

The column density can be related to the intensity of a single optically thin transition with the following equation (Hollis et al. 2004)

$$N_T = \frac{1}{2}\frac{3k}{8\pi^3}\sqrt{\frac{\pi}{\ln 2}}\frac{Q\exp(E_u/T_{ex})\Delta T_B \Delta V}{B\nu S\mu^2\eta_B\left(1-\frac{\exp(h\nu/kT_{ex})-1}{\exp(h\nu/kT_{bg})-1}\right)} \tag{3.7}$$

where the relevant quantities for propagating the uncertainty are $\Delta T_B$, $\Delta V$, $T_{ex}$, and $T_{bg}$ for a single transition. However, our calculation of the column density is dependent on *all* of the transitions included in the molecule's catalog. Due to the nature of performing a least-squares minimization the stronger transitions will be weighted more heavily in this calculation. The uncertainty in our final value for the column density can then be found by taking an intensity-weighted mean of the column density uncertainty calculated for individual optically thin transitions of a molecule

$$\sigma_{N_T} = \sqrt{\left(\sum_{j=1}^{N}\frac{\sigma_j I_j^2}{\sum_{k=1}^{N} I_k^2}\right)^2 + \sigma_{flux}^2} \tag{3.8}$$

where $N$ is the number of transitions, $\sigma_j$ is the propagated uncertainty of the column density for a single transition, $I_j$ is the intensity of the transition, and $\sigma_{flux}$ represents 10% of the column density value to account for the absolute flux calibration uncertainty (Cortes et al. 2023). Note that $\sigma_j$ does not take into account the absolute flux calibration uncertainty as this quantity is correlated across transitions and incorporating it before the final step would result in an underestimate of the uncertainty. As the intensity of optically thick transitions does not change with small changes to the column density, such transitions do not contribute to the uncertainty calculation and are thus excluded from the calculation.

### 3.3.5 Identifying Areas of Concern

While a visual inspection indicates that the simulated spectra generated by the automated fitting routine appear to match the observations within the uncertainties for the vast majority of the pixels in our field of view, there are a number of pixels for which the derived parameters were a relatively poor representation of the observations. The principle area of concern was a block of pixels toward MM1C, which displayed a large number of absorbed channels. While the derived parameters for many of the molecules were reasonable, the visible absorption negatively affected enough of the molecules that we decided to mask the region in its entirety for the column density maps. We have highlighted the pixels here as both a cautionary example and as a demonstration that the routine is capable of extricating itself from an unrealistic parameter space after fitting a problematic region.

Since the rows are each fit independently in our pseudo-parallel fitting routine, we had to be careful about introducing artificial structure. This was apparent in early versions of the routine where two rows would diverge wildly in velocity and/or column density for the same molecule. There appeared to be two separate causes for such an effect:

1. High opacity: When moving over areas of high opacity, the fitting routine could not match any of the strongly absorbed lines for molecules like methanol or methyl cyanide.

2. Low initial signal: Starting the fitting routine in a region of the image with low signal would cause the column density for weak molecules to go to unrealistic values, which could propagate through the rest of the image due to the bounds being dependent on the fit from the previous pixel.

These two separate causes were evident in MM1 and MM2, respectively. The opacity issue in MM1 and efforts to mitigate it have already been discussed with the upper state energy threshold in Section 3.3.3, though this did not solve the issue for every pixel as shown with the additional mask we put in place around MM1C. In MM2, we found that simply starting the routine in an image column with higher signal and then branching out in either direction alleviated the issue. This fix necessitated a change in how the fitting routine hopped between pixels (see Figure 3.5).

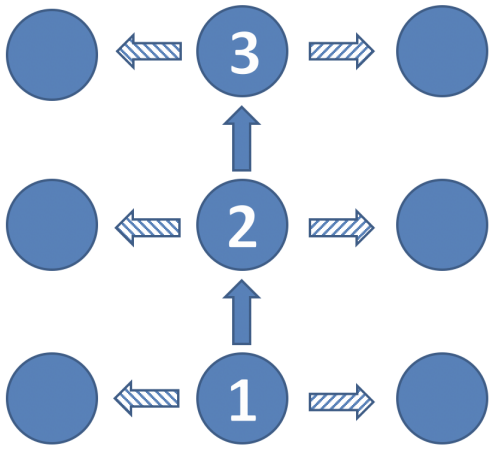


Fig. 3.5.— Diagram showing the path of the fitting routine in MM2 on a sample 3x3 image. This path was better suited to MM2 due to the low signal at the edges of our field of view for many molecules. The dashed arrows denote the subsequent stage of fitting.

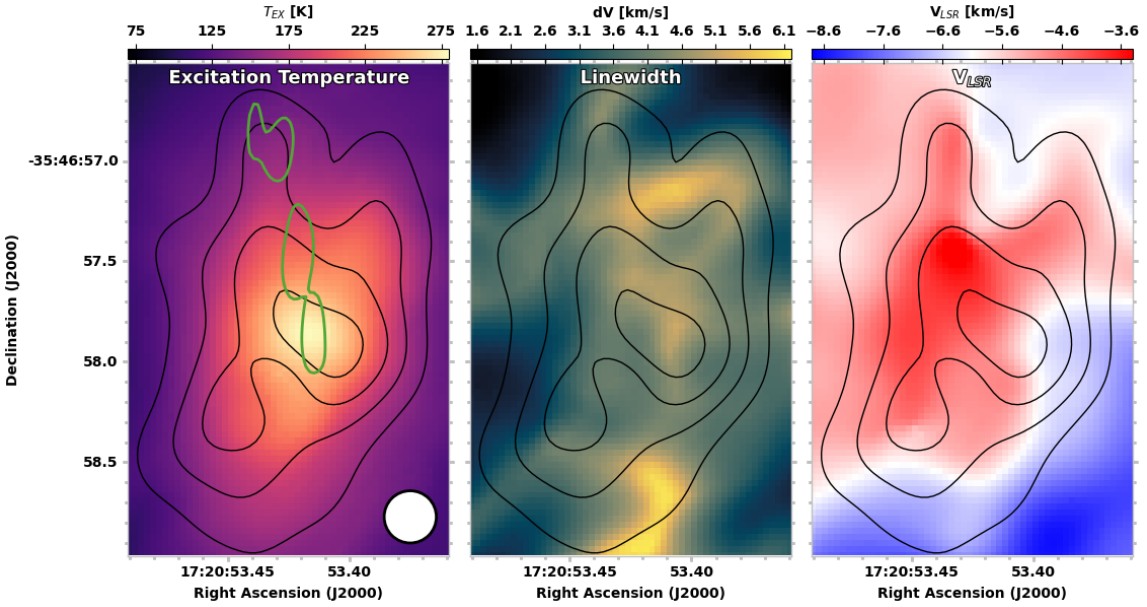


Fig. 3.6.— The excitation temperature (left) linewidth (middle), and velocity (right) maps for MM1 that were produced by the fitting routine. These parameters were shared for all of the molecules in our model. The contours mark continuum levels of 50, 90, 130, and 170 K. The green contours mark the same VLA 7mm emission as in Figure 3.1.

## 3.4 Results

### 3.4.1 The Shared Parameters - $T_{ex}$, $\Delta V$, and $V_{LSR}$

Figure 3.6 shows the final values for the excitation temperatures, linewidths, and velocities across MM1 while Figure 3.7 shows the same for MM2. For both of these sources, the presented linewidth images have been deconvolved from the channel width. In MM1, the excitation temperature tracks rather well with the continuum emission with little to no variation otherwise. The linewidth image, on the other hand, shows a significant amount of internal structure with broadening clearly visible in a column to the north and south. This broadening is consistent with our understanding of the kinematics of MM1 as the existence of a N-S outflow has previously been

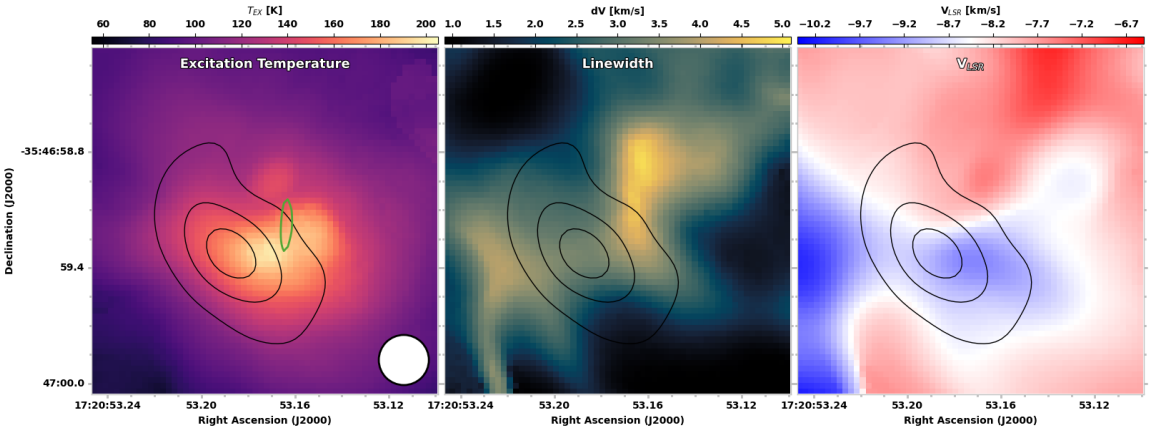


Fig. 3.7.— The excitation temperature (left) linewidth (middle), and velocity (right) maps for MM2 that were produced by the fitting routine. These parameters were shared for all of the molecules in our model. The contours mark continuum levels of 20, 35, and 50 K. The green contours mark the same VLA 7mm emission as in Figure 3.1.

traced by maser emission and thermal lines of CS and HDO (Brogan et al. 2018; McGuire et al. 2018). The line broadening is a likely consequence of the walls of the outflow impacting the more quiescent gas. This technique gives us a concrete visual demonstration on how such large scale effects have a measurable impact on the spectral emission.

In MM2, neither the excitation temperature nor the linewidth images correlate particularly well with the continuum emission. The excitation temperature increases rapidly to the west of the continuum peak, whereas the linewidths display a clear enhancement to the northwest.

### 3.4.2 Column Densities

The column density is uniquely derived for each of the 21 molecules that are included in the fitting routine's emission model. In this discussion, we will primarily be focusing on images for the three $C_2H_4O_2$ isomers: methyl formate, glycolaldehyde, and acetic

acid, with images for the other molecules available in Appendix A2. The methyl formate image will, however, be that of the $^{13}$C isotopologue ($CH_3O^{13}CHO$) due to the fact that it is optically thin over our entire field of view as opposed to the standard isotopologue. Each of the images in the following sections (Figures 3.8 and 3.9) has had two masks applied. Using the final fit parameters for each molecule, any pixel with less than 3 transitions with intensities greater than 5x the rms noise was masked. This mask manifests largely in the outermost pixels of MM1 and also results in a significant portion of the MM2 field of view being masked for certain molecules. The previously-mentioned block of pixels around MM1C (§ 3.3.5) was masked for all molecules.

**MM1 Results**

The spatial morphology of 13-methyl formate follows the continuum emission in a fairly straightforward manner - peaks and troughs in the continuum emission are generally mirrored by increases and decreases in the 13-methyl formate column density, respectively.

The glycolaldehyde column density does not follow the continuum quite as closely as 13-methyl formate with several locations across MM1 presenting column densities close to the maximum; the strongest peak lies to the west of MM1B, which is offset from the peak of 13-methyl formate.

Acetic acid exhibits the sharpest increases and fall-offs in column density in our field of view for MM1, with a peak column density exceeding the other two molecules (its peak column density approaches that of 12-methyl formate) while also having a significant amount of masking visible due to the lack of detectable transitions in the north and south. While acetic acid also peaks to the west of MM1B, there is little

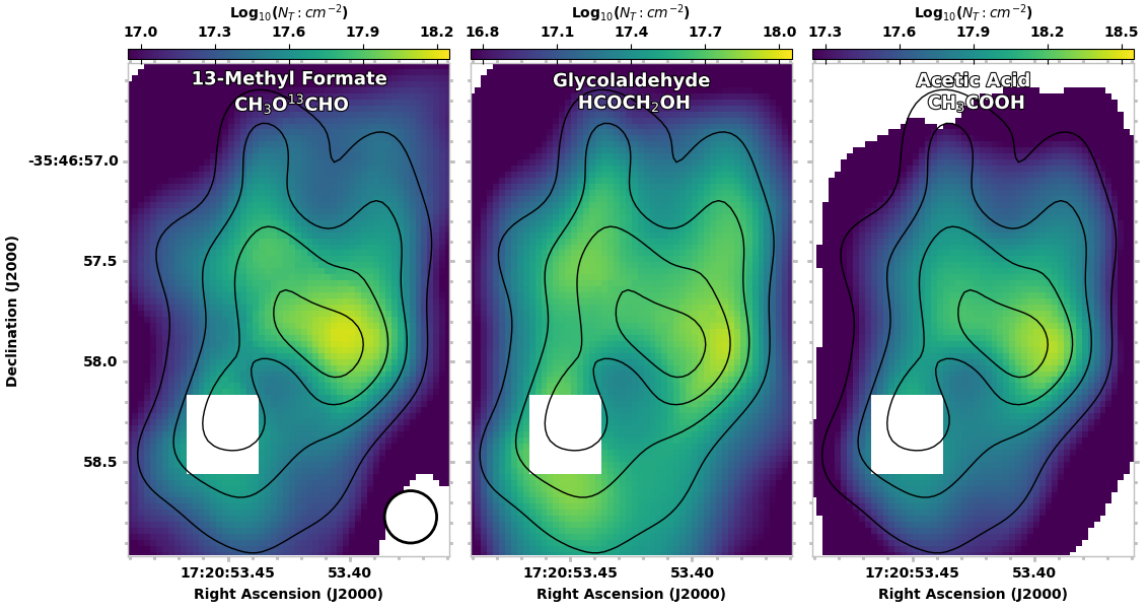


Fig. 3.8.— MM1 column density maps for the three $C_2H_4O_2$ isomers: 13-methyl formate (left), glycolaldehyde (middle), and acetic acid (right) produced by the fitting routine. Pixels with a low signal-to-noise ratio have been masked on a per-molecule basis and appear white (mainly visible in the acetic acid map) with an additional mask applied around MM1C for all molecules.

apparent structure in the column density map besides also following the continuum emission fairly closely.

### MM2 Results

As shown in Figure 3.9, 13-methyl formate is the easiest isomer to detect in MM2, with relatively few pixels meeting the criteria for masking. The principal structure in the column density is a narrow band that closely follows the continuum emission. A slight decrease in the column density is also visible to the northwest of the continuum peak, around MM2B.

In MM2, glycolaldehyde is largely seen towards the innermost regions, with much of the image masked due to the lack of readily detectable transitions. The previous

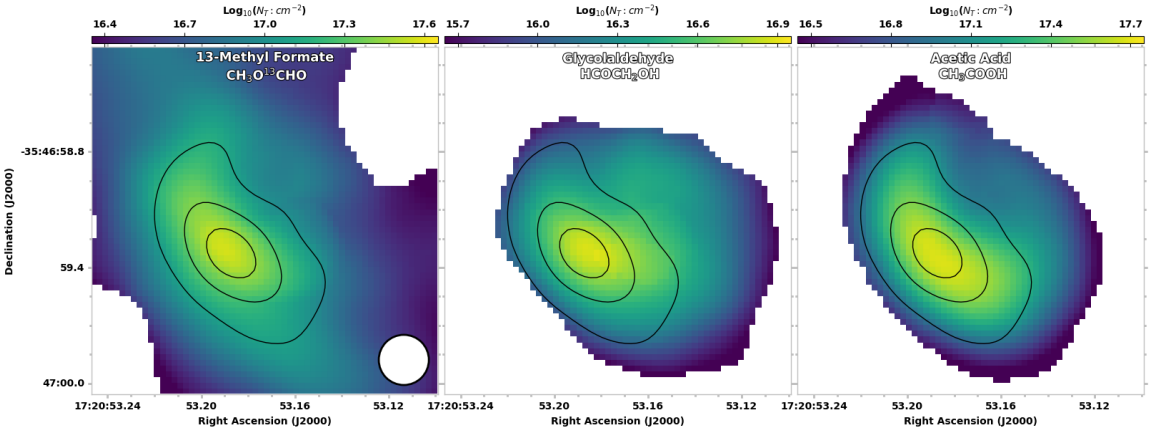


Fig. 3.9.— MM2 column density maps for the three $C_2H_4O_2$ isomers: 13-methyl formate (left), glycolaldehyde (middle), and acetic acid (right) produced by the fitting routine. Pixels with a low signal-to-noise ratio have been masked on a per-molecule basis and appear white, which has a noticeable impact on all three molecules in MM2.

work of El-Abd et al. (2019) had established the difficulty in detecting glycolaldehyde toward this source; this is reinforced by the significant masking in the field of view due to the small number of visible transitions. The presented column densities for glycolaldehyde in MM2 should be treated as upper limits.

The acetic acid distribution in MM2 is compact around the continuum emission, with much of the field of view again being masked due to the low intensity of the strongest transitions. In pixels that haven't been masked, however, the acetic acid morphology closely resembles that of 13-methyl formate with the same narrow band cutting through the continuum contours.

### 3.4.3 Column Density Ratios

A unique benefit of this method of spectral analysis is the ability to produce images that directly display the column density ratios between molecules, shown in Figure 3.10 for the three $C_2H_4O_2$ isomers. There is a coherent structure to the map of the glycolaldehyde column density ratio with 13-methyl formate. The stand-out feature is

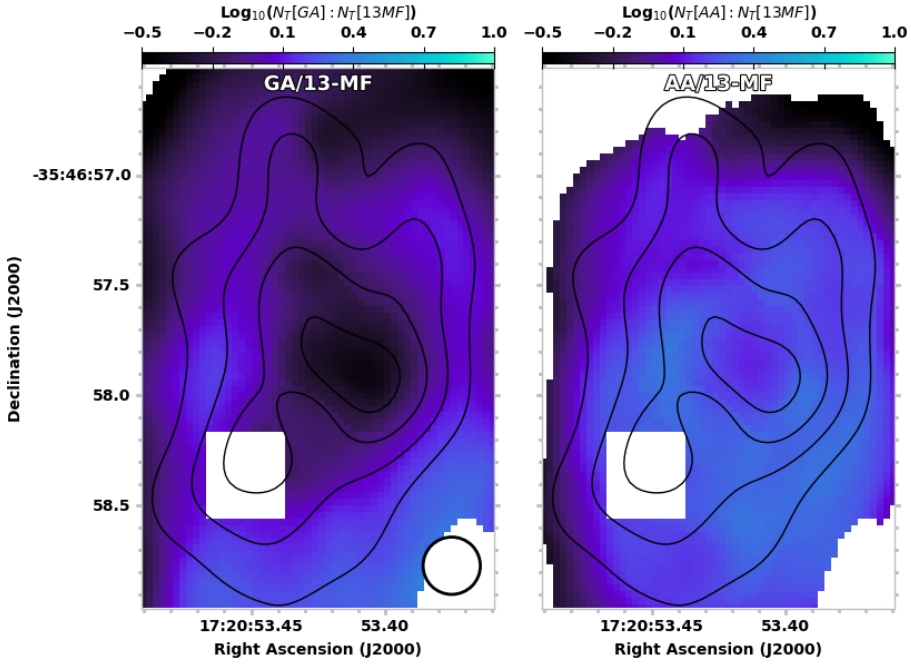


Fig. 3.10.— Images of the ratios of the glycolaldehyde *(left)* and acetic acid *(right)* column densities with those of 13-methyl formate in MM1.

the relative depletion of glycolaldehyde towards the continuum peak; it is conceivable, however, that the glycolaldehyde column density is getting underestimated in the region due to the optical depth of the spectra. The ratio with acetic acid, on the other hand, is remarkably constant over the field of view.

## 3.5 Discussion

### 3.5.1 Previous Findings

Analysis of the $C_2H_4O_2$ isomers has previously been carried out in NGC 6334I by El-Abd et al. (2019) where the relative abundances of the three molecules were compared across select locations toward both MM1 and MM2 along with measurements for other star-forming regions that were found in the literature. While methyl formate

and acetic acid were found to track linearly across all of the star-forming regions in the sample, methyl formate and glycolaldehyde instead displayed a bimodal trend with their abundances. Interestingly, the abundances of these molecules in MM1 and MM2 followed separate trends, an indication of some factor(s) preferentially affecting the production of glycolaldehyde despite the regions' proximity. As these distributions were identified with a relatively small number of data points, we could now test whether the observed trends hold up with a much larger sample size across MM1 and MM2.

### 3.5.2 Collating the Column Density Results

The key finding in El-Abd et al. (2019) was in how ratios of molecular column densities appeared to display distinct trends across multiple sources. This pointed to some physical or chemical factor affecting the production of the selected molecules in a way that had not previously been considered. In that work, the ratio of methyl formate to glycolaldehyde was shown to have two distinct linear trends among a number of star-forming regions. Crucially, NGC 6334I-MM1 and -MM2 lay in separate trends, despite their close proximity. As previously discussed however, these trends were derived from a small number of spectra extracted from each source. The values for other star-forming regions were limited to a single point each. Reproducing such a plot with the plethora of new data points we have produced in this work would serve as an excellent indicator of whether the bimodal trend previously observed was due to the small sample size, or whether it was a true distinction in the data. It should be noted that we are instead using the $^{13}$C isotopologue of methyl formate for this work, as the standard isotopologue was too optically thick for many of the positions in our field of view.

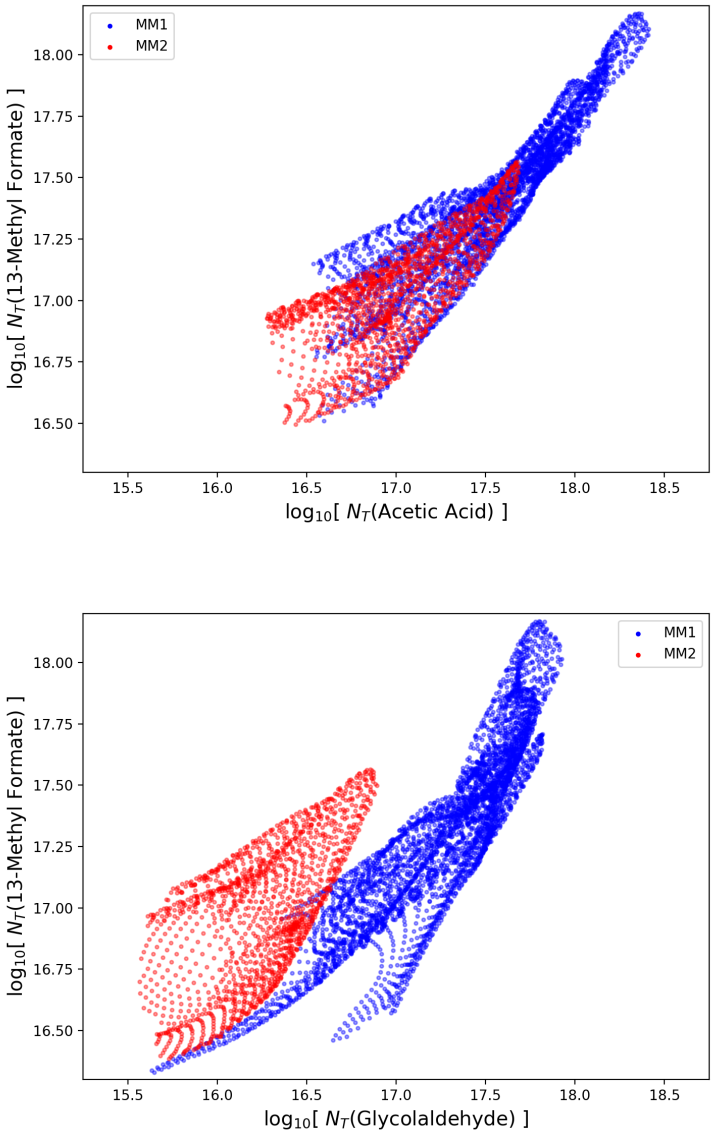


Fig. 3.11.— The column density of 13-methyl formate plotted against acetic acid (top), and glycolaldehyde (bottom). The 13-methyl formate and acetic acid column densities follow a single linear trend across MM1 and MM2, while the glycolaldehyde column density points to two distinct trends between MM1 and MM2. Masked pixels in Figures 3.8 and 3.9 have been excluded from these plots. The trends observed in El-Abd et al. (2019) hold up with the additional data measured in this work.

As can be seen in Figure 3.11, the addition of this new data has broadened the previously-observed trends of the $C_2H_4O_2$ isomers; it also appears that this data now encompasses several distinct regimes in which the production of these molecules may differ from one another within the same source. Despite this, the conclusions of El-Abd et al. (2019) would appear to be upheld; the acetic acid points in MM2 comprise a single trend when combined with data from MM1, while there still appears to be two wholly separate trends in the production of glycolaldehyde relative to 13-methyl formate between the two sources.

Besides the large-scale linear trends in Figure 3.11 there is some finer structure that is particularly visible when the data is colored by the excitation temperature (Figure 3.12). Wilkins et al. (2022) took this approach when comparing the $^{13}CH_3OH$ and $CH_3OD$ column densities in Orion-KL. In the case of acetic acid, the column densities and excitation temperatures match up extremely well in the low excitation temperature regime (below $\sim$ 150 K). There is a distinct trend that is populated by the higher excitation temperature data in MM1, but there is no comparable MM2 data to compare.

The glycolaldehyde plot in Figure 3.12 on the other hand, tells a much more complicated story. Taking each source separately, the glycolaldehyde column density generally increases with the excitation temperature in MM2. In MM1, the same thing happens at lower excitation temperatures (albeit at a faster rate) but the highest excitation temperature data carves out its own trend in the middle of the column density data. Interestingly, it is this high excitation temperature trend that matches the slope of the MM2 data. Overall, however, the column density and excitation temperature data are poorly correlated in the glycolaldehyde data, possibly indicating that there are other factors that play a more prominent role in the interstellar

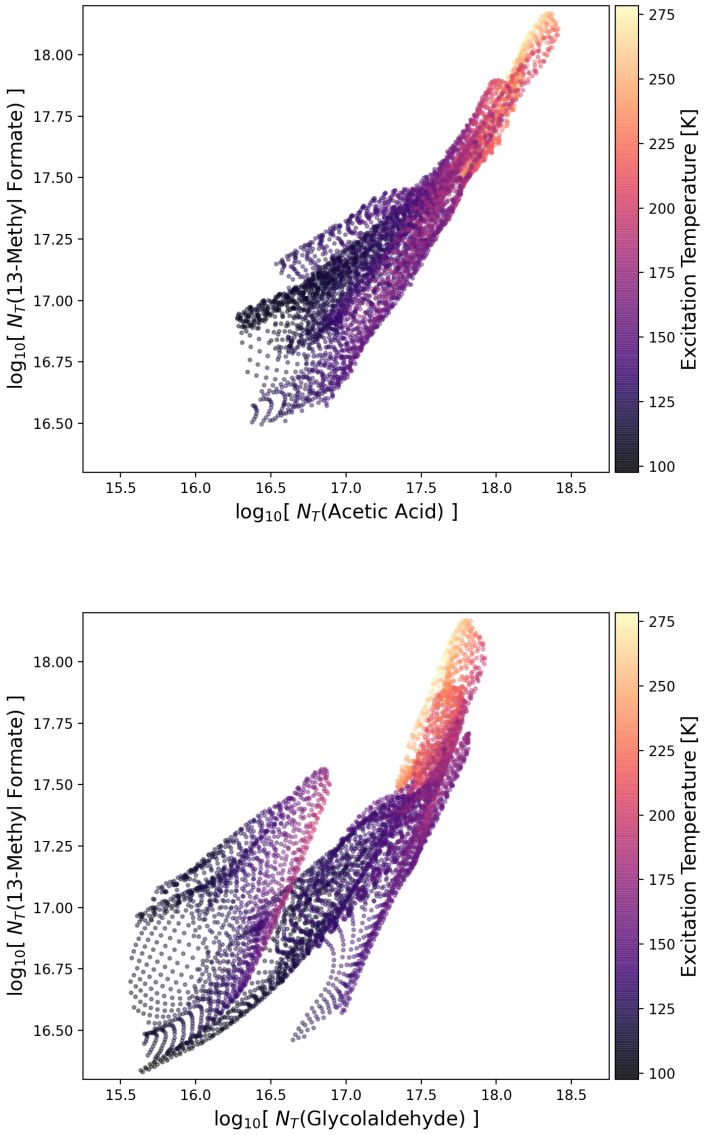


Fig. 3.12.— The same column density data in Figure 3.11, this time colored by the excitation temperature of the fit.

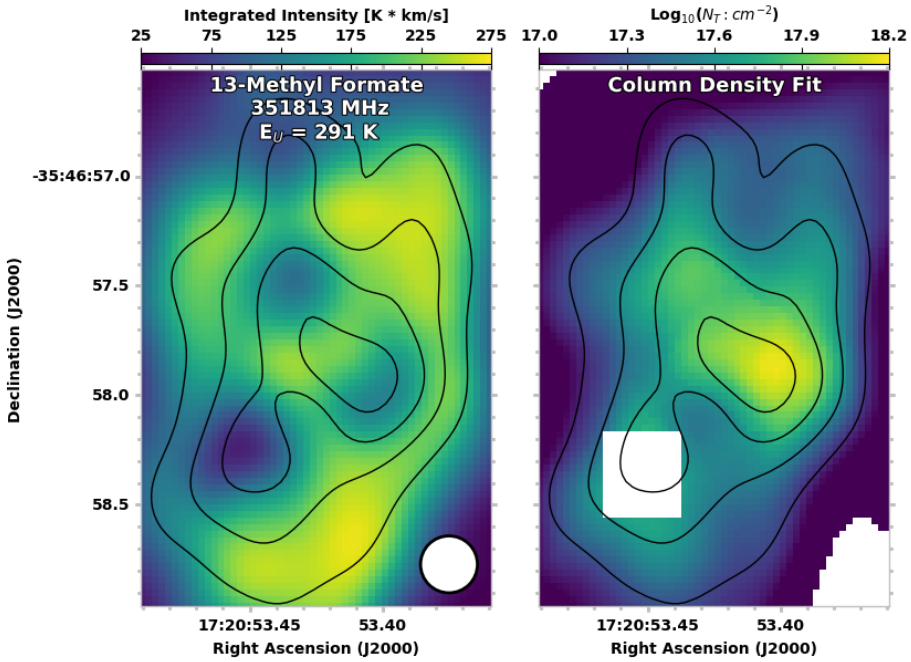


Fig. 3.13.— A side-by-side comparison of an integrated intensity map (left) using a single 13-methyl formate transition and the 13-methyl formate column density image produced by the fitting routine (right) in MM1. The integrated intensity map was produced by integrating over a velocity range of -10.4 to -2.7 km $s^{-1}$.

formation of glycolaldehyde.

### 3.5.3 Comparison with Traditional Moment Maps

In contrast with moment map analyses, the images that are presented as part of this work – for both the physical column densities and the velocity – are derived using the entire set of transitions for each included molecule in our observed bandwidth. Thus, we have removed any ambiguity that comes from the excitation of a single transition - provided there are enough transitions for said molecule in the scope of our observations to appropriately model the column density - as well as alleviated any concerns about the velocity shifting out of a relevant range. The comparison of the two methods in this work was conducted with 13-methyl formate. There are a number of 13-methyl

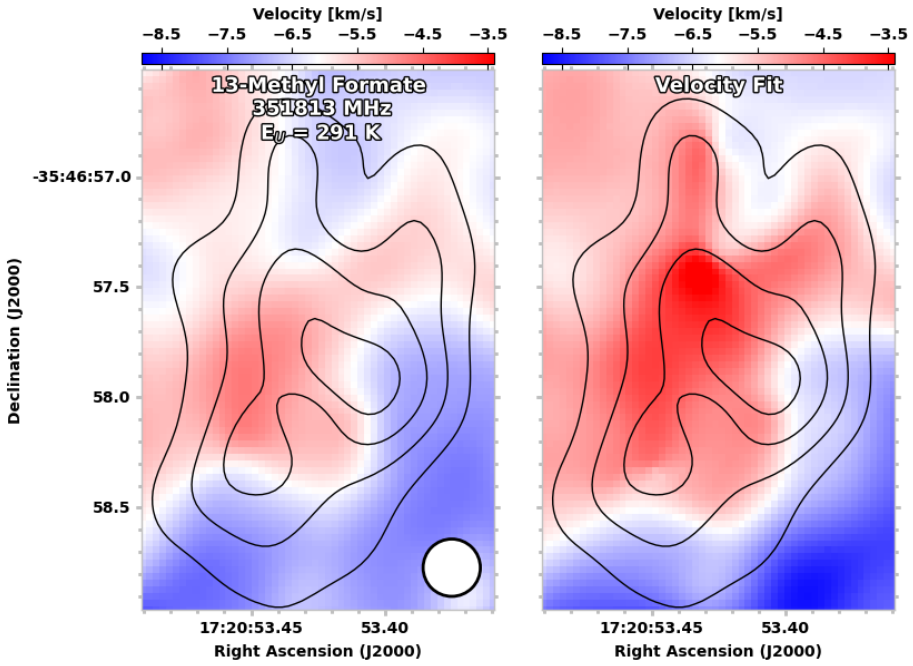


Fig. 3.14.— A side-by-side comparison of a velocity moment map (left) using a single 13-methyl formate transition and the velocity image produced by the fitting routine (right) in MM1.

formate transitions in our frequency range; unfortunately, while the transition used to create these moment maps appeared to be unblended for a number of positions, it also appears to be noticeably optically thick in several positions in MM1. It remains, however, the best of the available options in our data, and serves to illustrate the potential pitfalls when attempting to apply the moment map methodology to such a complex dataset. Even the $^{13}$C isotopologue of an abundant molecule is capable of apparent opacity issues, along with the difficult task of identifying a transition that is perpetually unblended across thousands of pixels in a region with an evolving molecular inventory and varying physical parameters.

**Comparison in MM1**

There are several differences in the morphologies of the integrated intensity maps and column density images of methyl formate (Figure 3.13) that are immediately apparent. Many of the regions that were highlighted in Figure 3.1 coincide with dips in the integrated intensity map; this is most likely a consequence of this particular transition having a high optical depth at these positions. The column density image, as previously discussed, instead varies smoothly across our field of view in a manner that loosely follows the continuum emission. This highlights the challenges of using moment maps as proxies for molecular distributions, as there are clear morphological differences from a true map of the column density.

In contrast, the moment 1 map from this transition and the velocity image from the routine are qualitatively much more similar (Figure 3.14). There still exist discrepancies between the two, however, with the greatest divergence occurring around MM1F on the order of several kilometers per second. Delving into the spectra in some of these pixels, it was clear that the kinematics had not been adequately captured by the channels selected for the moment map (see Appendix A2 for a visual demonstration). This reinforces the difficulty in finding a single range of channels that adequately treats an entire star-forming region for the purposes of generating a velocity field from a moment map. Simply increasing the number of channels to capture the emission in one position would introduce unwanted emission in other positions. In both presented moment maps there are myriad effects which may negatively impact our ability to gain accurate information and are alleviated by the images produced by the fitting routine. The opacity of an individual transition is mitigated by leveraging all of the available transitions for a particular molecule; spectral contamination of an individual transition from molecular variation in different positions also ceases to be

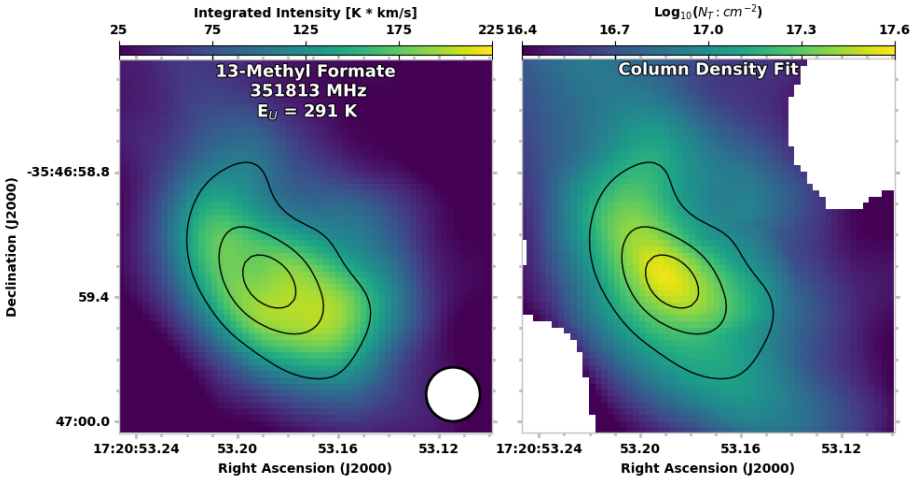


Fig. 3.15.— A side-by-side comparison of an integrated intensity map (left) using a single 13-methyl formate transition and the 13-methyl formate column density image produced by the fitting routine (right) in MM2.

an issue. In addition, the velocity image is not skewed by improperly accounting for the velocity structure in a source - an impossible task for a source as complicated as NGC 6334I.

### Comparison in MM2

The morphologies of the integrated intensity maps and column density images are in much better agreement in MM2 than MM1 (Figure 3.15). The molecule is fairly well matched to the continuum emission in both cases, and there are no regions where the two plots significantly differ, likely due to the generally lower opacity of MM2. The moment 1 map is in fairly good agreement with the velocity image outside of the displayed contours (Figure 3.16), but diverges fairly significantly (again on the order of a few kilometers per second) towards the warmer region. See Appendix A2 for a discussion on how such a discrepancy may arise.

Table 3.1: Molecules Included in the Fitting Routine

| Molecule | Catalogs | Vib. States [1,2] | No. of Transitions [3] | $E_U$ Range [K] | $E_U$ Threshold | Database [4] |
|---|---|---|---|---|---|---|
| $CH_3OH$ | 1 | $\mathbf{v_t = 2}$ | 49 | 573 - 2524 | None | CDMS |
| $^{13}CH_3OH$ | 1 | $\mathbf{v_t = 0 - 1}$ | 57 | 17 - 891 | None | CDMS |
| $CH_3CN$ | 2 | $\mathbf{v = 0, v_8 = 1}$ | 112 | 120 - 2969 | $3 * T_{BG}$ | CDMS |
| $CH_3\ ^{13}CN$ | 1 | $v = 0$ | 29 | 120 - 1721 | None | CDMS |
| $NH_2CN$ | 1 | $v = 0$ | 76 | 101 - 1569 | None | JPL |
| $H_2CCO$ | 1 | $v = 0$ | 29 | 102 - 2323 | None | CDMS |
| $CH_3CHO$ | 1 | $\mathbf{v_t = 0 - 2}$ | 626 | 26 - 2939 | None | JPL |
| $NH_2CHO$ | 2 | $v = 0, v_{12} = 1$ | 145 | 58 - 2472 | $3 * T_{BG}$ | CDMS |
| t-HCOOH | 1 | $v = 0$ | 98 | 24 - 2048 | None | CDMS |
| $CH_3OCH_3$ | 1 | $\mathbf{v = 0}$ | 267 | 32 - 1302 | None | CDMS |
| $C_2H_5OH$ | 1 | $v = 0$ | 1143 | 49 - 2688 | None | CDMS |
| $C_2H_5CN$ | 1 | $v = 0$ | 348 | 25 - 2886 | None | CDMS |
| $CH_3COCH_3$ | 1 | $\mathbf{v_t = 0 - 2}$ | 1486 | 46 - 2241 | None | JPL |
| $CH_3OCHO$ | 1 | $\mathbf{v_t = 0 - 1}$ | 993 | 38 - 1749 | None | JPL |
| $HCOCH_2OH$ | 1 | $v_t = 0 - 3$ | 2142 | 27 - 4916 | None | CDMS |
| $CH_3COOH$ | 2 | $\mathbf{v_t = 0, v_t = 1}$ | 2790 | 36 - 2398 | None | CDMS |
| $CH_3O^{13}CHO$ | 1 | $\mathbf{v_t = 0 - 1}$ | 1435 | 25 - 1485 | None | CDMS |
| a$-(CH_2OH)_2$ | 1 | $v = 0$ | 951 | 60 - 1696 | None | CDMS |
| g$-(CH_2OH)_2$ | 1 | $v = 0$ | 1104 | 59 - 1912 | None | CDMS |
| $CH_3OCH_2OH$ | 1 | $v = 0$ | 421 | 67 - 1105 | None | CDMS |
| $SO_2$ | 2 | $\mathbf{v = 0, v_2 = 1}$ | 90 | 29 - 5355 | None | CDMS |
| $CH_3OH^{\ddagger}$ | 1 | $\mathbf{v_t = 0 - 1}$ | 216 | 17 - 2640 | N/A | CDMS |
| $CH_3\ ^{18}OH^{\ddagger}$ | 1 | $\mathbf{v_t = 0 - 2}$ | 160 | 29 - 2620 | N/A | CDMS |
| $HNCO^{\ddagger}$ | 1 | $v = 0$ | 14 | 143 - 1536 | N/A | CDMS |
| $SO^{\ddagger}$ | 2 | $v = 0, v = 1$ | 7 | 26 - 1718 | N/A | CDMS |
| $HC_3N^{\ddagger}$ | 1 | $\mathbf{v = 0}$ | 2 | 217 - 307 | N/A | CDMS |
| $OCS^{\ddagger}$ | 2 | $v = 0, v_2 = 1$ | 6 | 161 - 924 | N/A | CDMS |

[1]Vibrational states in separate catalogs are denoted by commas.
[2]Bolded text indicates entries where vibrational contributions to the partition function are included.
Column density estimates for the non-bolded entries are potentially slightly underestimated in the case
an updated partition function is calculated. All entries use the most up-to-date partition functions as of publication.
[3]This number refers to all of the transitions in the catalog in our frequency range, not all detected transitions.
[4]The catalogs were obtained from both the CDMS (Müller et al. 2005a) and JPL (Pickett et al. 1998b) spectroscopic databases.
‡Channels containing emission from these molecules are excluded from the fit.

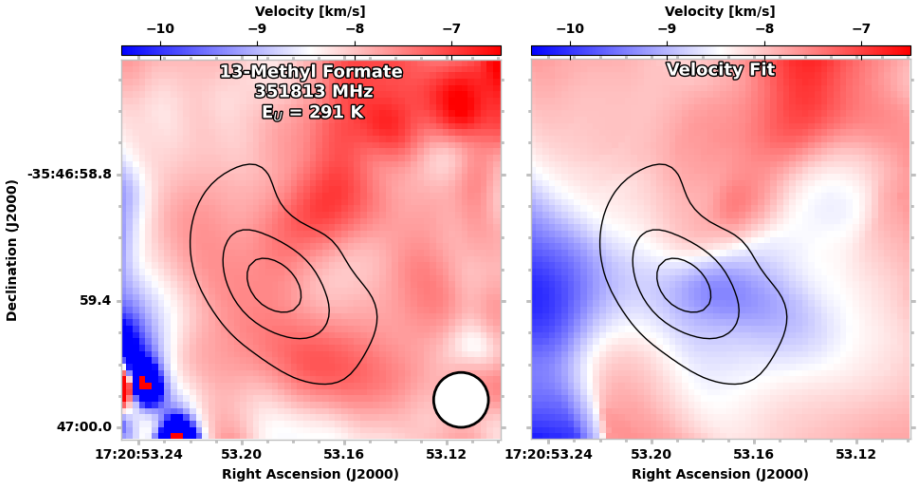


Fig. 3.16.— A side-by-side comparison of a velocity moment map (left) using a single 13-methyl formate transition and the velocity image produced by the fitting routine (right) in MM2. Note that the speckled portion in the bottom left of the moment map corresponds to a region with very weak 13-methyl formate emission (see Figure 3.15).

## 3.6 Conclusions

Star-forming regions are physically complicated environments; if we are to better understand the effects that evolving protostars have on their environments, and how those environments in turn affect the formation of the protostars, we must first be able to understand the wide range of physical conditions present in these sources. While this problem is of a scale that would be intractable to solve by treating individual pixels, we have demonstrated the feasibility of an automated approach to the measurement of the physical conditions and molecular column densities in NGC 6334I-MM1 and -MM2. The observed trends with respect to the bifurcation of the relative column densities of the $C_2H_4O_2$ isomers were in agreement with the work of El-Abd et al. (2019). Comparisons were conducted with the results of the fitting routine and the closest moment map analogues. In comparing the moment 1 map and velocity image the fitting routine more accurately represented the velocity of the

emission. Comparing the moment 0 maps and column density images demonstrated shortcomings in attempting to use the moment 0 map as a proxy for the column density.

This paper makes use of the following ALMA data: #2015.A.00022.T. ALMA is a partnership of ESO (representing its member states), NSF (USA) and NINS (Japan), together with NRC (Canada) and NSC and ASIAA (Taiwan) and KASI (Republic of Korea), in cooperation with the Republic of Chile. The Joint ALMA Observatory is operated by ESO, AUI/NRAO and NAOJ. The National Radio Astronomy Observatory is a facility of the National Science Foundation operated under cooperative agreement by Associated Universities, Inc. This research made use of NASA's Astrophysics Data System Bibliographic Services, Astropy, a community-developed core Python package for Astronomy (Astropy Collaboration et al. 2022), and APLpy, an open-source plotting package for Python (Robitaille & Bressert 2012). Support for this work was provided by the NSF through the Grote Reber Fellowship Program administered by Associated Universities, Inc./National Radio Astronomy Observatory. We would like to thank the referee for their comments regarding this work.

# Chapter 4

# Initial Application of SAMER to a Survey of High Mass Star-Forming Regions

## 4.1 Introduction

A major ongoing problem in the field of massive star formation is the absence of a large-scale survey of massive star-forming regions. Much of our understanding of this process instead comes from in-depth case studies of a handful of individual sources such as Orion-KL and Sagittarius B2. What makes these sources compelling objects of study, however, does not necessarily mean they are representative of the typical massive star formation process. In the case of Sgr B2, its uncommonly rich molecular spectra and subsequent brightness in the radio regime have made it a favored observational target for many years, but there is little reason to believe its observed properties would translate to a better understanding of other sources.

The Complex Chemistry in hot Cores with ALMA (CoCCoA) project (PI: B.

McGuire) was designed to fill this need of the astronomical community by observing a large number of massive star-forming regions across the same frequency range and similar distances in order to ensure as homogeneous a dataset as possible for the selected sources. This allows for the most robust comparison of physical parameters and molecular properties between the sources. This is a necessary step in order to provide proper constraints on the physical conditions in which these molecules are found for chemical models aiming to reproduce the observed chemical abundances.

Following the proof-of-concept work in El-Abd et al. (2024) where physical parameters were derived for the massive star-forming region NGC 6334I using an automated fitting routine, we describe the initial results of our application of this routine - the Simultaneous Autonomous Molecular Emission Resolver (SAMER) - to one of the sources selected for the CoCCoA survey, G34.41+0.24.

## 4.2 G34.41+0.24

G34.41+0.24 is one of several hot cores associated with the parent infrared dark cloud G34.43+0.24 (Rathborne et al. 2006; Sakai et al. 2013). This core was first discovered by Shepherd et al. (2004) just north of an ultra-compact HII region containing newly-formed stars. Kurayama et al. (2011) used very long baseline interferometry maser parallax observations to measure the distance of this cloud to be 1.6 kpc. Shepherd et al. (2007) found evidence for multiple outflows from both G34.41+0.24 and the UC HII region.

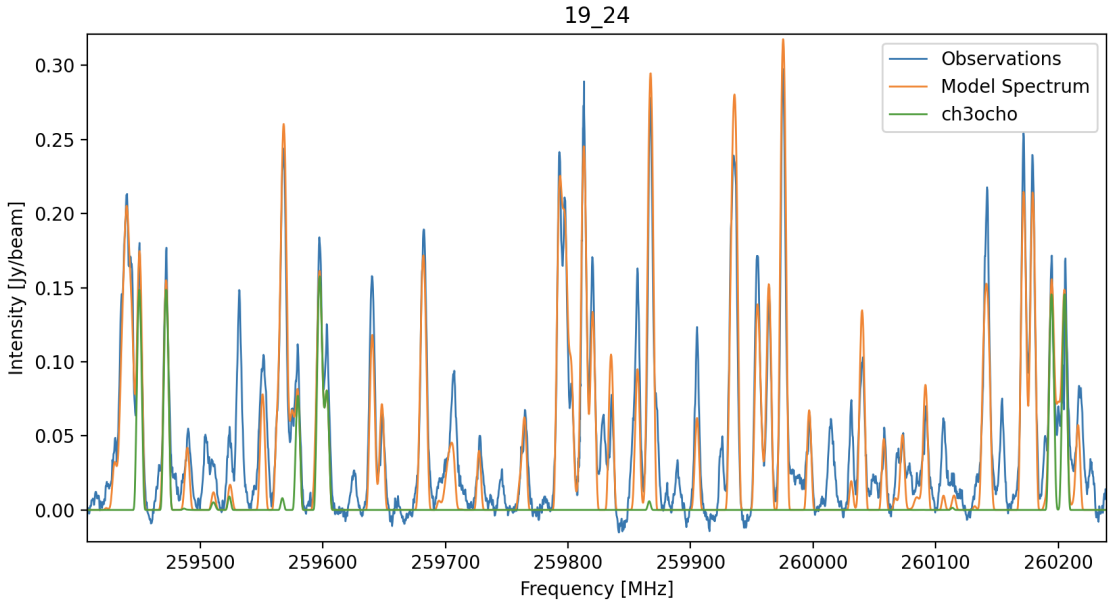


Fig. 4.1.— A sample of a spectrum from G34.41+0.24 showcasing the clean lineshapes and excellent fit of the model (orange) to observations (blue). The simulated methyl formate emission has been highlighted in green.

## 4.3 Observations

The data toward G34.41+0.24 were observed as part of the Complex Chemistry in hot Cores with ALMA (CoCCoA) survey of high-mass star-forming regions, project code 2019.1.00426.S. These data were observed on March 31 and April 2 of 2021 with an angular and spectral resolution of 0.″33 and 0.488 MHz, respectively. The central frequencies of the spectral windows are 258.453, 259.383, 260.313, and 261.243 GHz. For additional details on the observations, see Chen et al. (2023).

## 4.4 Methods

The physical parameters for each of the molecules in our model were derived with the automated fitting routine described in El-Abd et al. (2024) which was developed

as a module for `molsim` (Lee et al. 2023) hereafter referred to as SAMER. For an individual pixel all of the molecules share a single excitation temperature, linewidth, and velocity; the column density is unique to each molecule. The nature of our data for G34.41, however, did not require the use of the techniques developed by El-Abd et al. (2024) for extreme opacity to measure the excitation temperature and linewidth. The source treated in that work possessed several optically thick transitions for all of the pixels in the field of view which allowed for a direct calculation of the excitation temperature when combined with knowledge of the background temperature. G34.41 contains few enough optically thick transitions that the minimizer is largely capable of converging on a reasonable value for the excitation temperature given a spectrum that is well-populated with molecular transitions. There are a fair number of pixels around the outer edges of our field of view that contain very little emission from any molecules and are thus masked as there is no meaningful data to extract from such positions. The spectra of G34.41 are also crowded to a lesser degree than the spectra of NGC 6334I; when combined with the narrower bandwidth of our G34.41 observations, this resulted in a small enough sample of lines that we could not derive a robust estimate of the linewidth using the histogram that was previously employed. We therefore rely on the least-squares minimizer for this quantity as well. The velocity and column density measurements are derived using the least-squares minimization just as they were previously measured in El-Abd et al. (2024). The combined treatment of these parameters results in very good fits for the majority of pixels of interest in our field of view - see Figure 4.1.

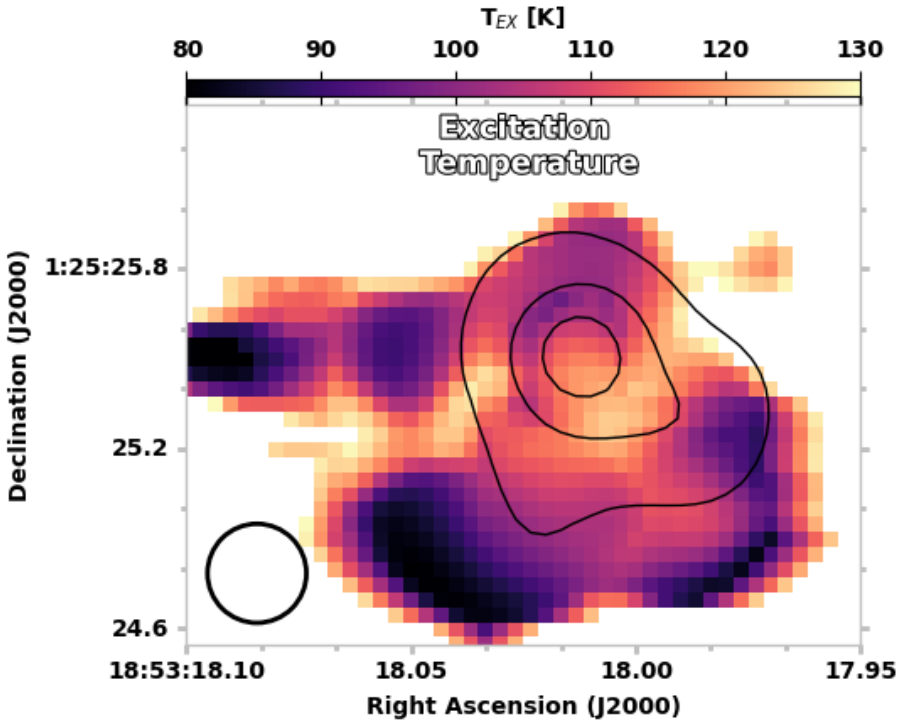


Fig. 4.2.— Excitation temperature image for G34.41+0.24. Much of the image has been masked due to unreliable measurements of this quantity which was unavoidable due to the limited number of lines with which to make a measurement. The contours mark continuum temperatures of 15, 30, and 45 K.

## 4.5 Results

### 4.5.1 Excitation Temperature

The excitation temperature image for G34.41 (Figure 4.2) shows structure that is fairly distinct from the continuum emission. The temperature is brightest near the continuum peak, but it should be noted that the temperature is likely getting underestimated in the the pixels with the brightest continuum, as the opacity and self-absorption effects visible in the spectra negatively impacted the calculation of the excitation temperature.

While we have extracted spectra from the entire presented field of view, the spec-

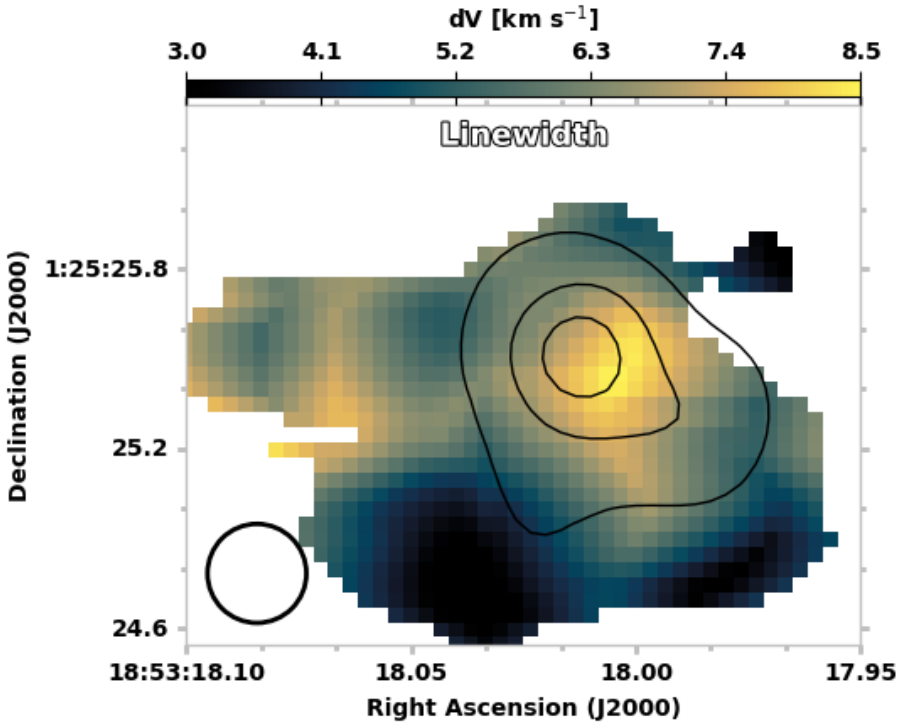


Fig. 4.3.— Linewidth image of G34.41+0.24. The structure here reflects the excitation temperature image fairly well. Many of the enhancements may also indicate the presence of multiple velocity components.

tral line density falls off dramatically outside of the lowest (15 K, black) continuum contours; in these pixels the automated routine increased the excitation temperature to unrealistic values as there was little emission with which to measure the value. Estimates of the excitation temperature were deemed unreliable for these pixels and the results were subsequently masked for pixels with an excitation temperature exceeding 130 K as this value empirically captured the majority of the affected regions. This mask was applied to all of the maps presented in this work.

### 4.5.2 Linewidth

The linewidth image (Figure 4.3) mirrors much of the structure that can be seen in the excitation temperature image. Chen et al. (2023) found potential evidence for multiple velocity components in the spectra of G34.41; examining the spectra from pixels exhibiting the broadest linewidths in our image, that appears to be the case for pixels in the eastern portion of the image. The broadening toward the continuum peak appears to be a simple case of true line broadening as opposed to capturing multiple velocity structures. This presents an avenue of refinement for future iterations of the fitting routine, as we do not currently have the tools in place to deal with multiple velocity components from the same molecule and SAMER instead broadens the lines to capture both components.

That the warmest regions of the image also exhibit the broadest linewidths indicates that the turbulence in these regions is greater than in colder regions. Shepherd et al. (2007) use CO emission to determine that there is “marginal evidence" for an outflow oriented in this direction using observations with much lower spatial resolution than what is used for this work. These regions that exhibit both brighter excitation temperatures and broader lines lie on an axis that is roughly parallel to the axis of rotation of the cloud that is shown in Figure 4.4 - this is potential evidence for a narrow outflow that was driven by the central hot core.

### 4.5.3 Velocity

The velocity image (Figure 4.4) shows a distinct turnover from blueshifted to redshifted velocities when taken relative to the central measured velocity value. This turnover cuts through the peak continuum value and likely indicates that the velocity image has captured the bulk rotation of the cloud surrounding the hot core.

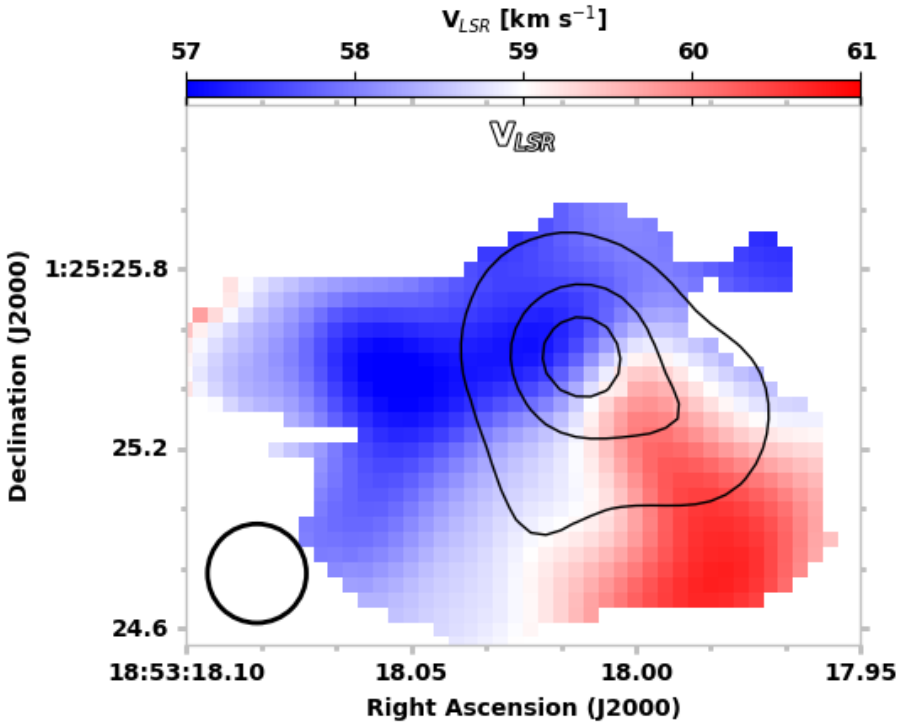


Fig. 4.4.— Velocity image of G34.41+0.24. The turnover from blueshifted to redshifted velocities indicates that we have likely captured the rotation of the cloud around the core.

We previously discussed the presence of multiple velocity components in this source in Section 4.5.2. These features are only visible well away from the peak continuum emission which is evidence for the relatively low opacity in the spectra at those positions. If we are seeing deeper into the cloud, then we are possibly seeing both the near- and far-side motions of the cloud supplying the star-formation material. From the regular motions of the velocity image and spectra, there is little evidence for multiple star-forming cores in this source.

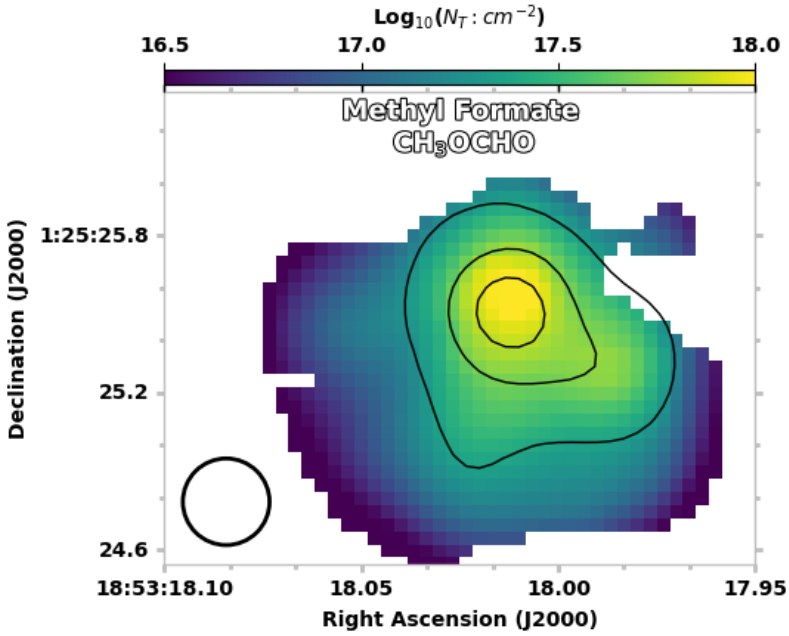


Fig. 4.5.— The spatial morphology of methyl formate column densities produced by SAMER.

### 4.5.4 Molecule Images

Many of the molecules in our model show a strong enhancement toward the peak of the continuum emission, with some minor variations. As the size of the features in these images roughly matches the size of the beam of our observations, this is a likely indication that we are not resolving the source of the emission. This is in stark contrast with the images that were produced of NGC 6334I, another massive star-forming region at a comparable distance that was observed with a smaller beam, where the molecule images showed distinct structures within the two regions that were analyzed. Figures 4.5-4.7 show the images for a number of the molecules in our emission model.

An additional mask has been applied to each individual molecule map that covers pixels containing less than two transitions exceeding a $3\sigma$ rms noise threshold. This is

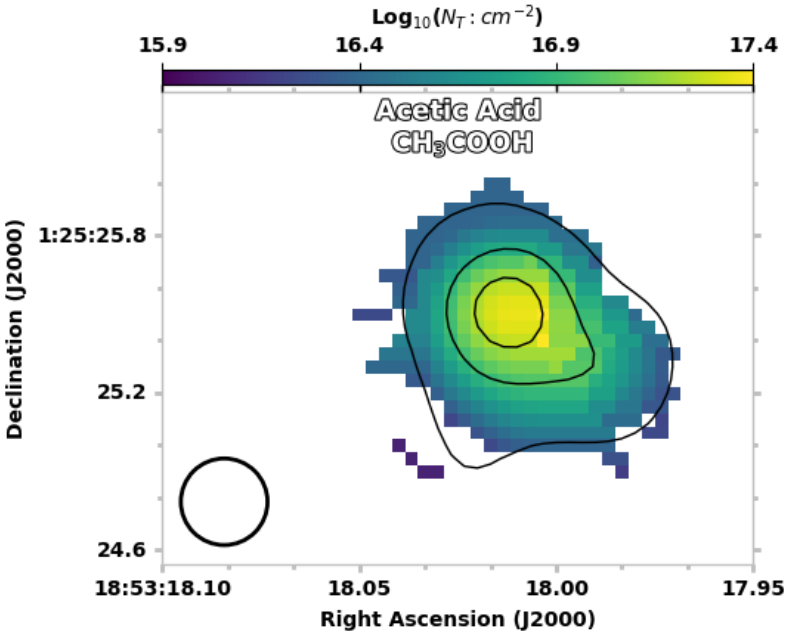


Fig. 4.6.— The spatial morphology of acetic acid column densities produced by SAMER. Note the sharp falloff of this molecule outside of the continuum contours.

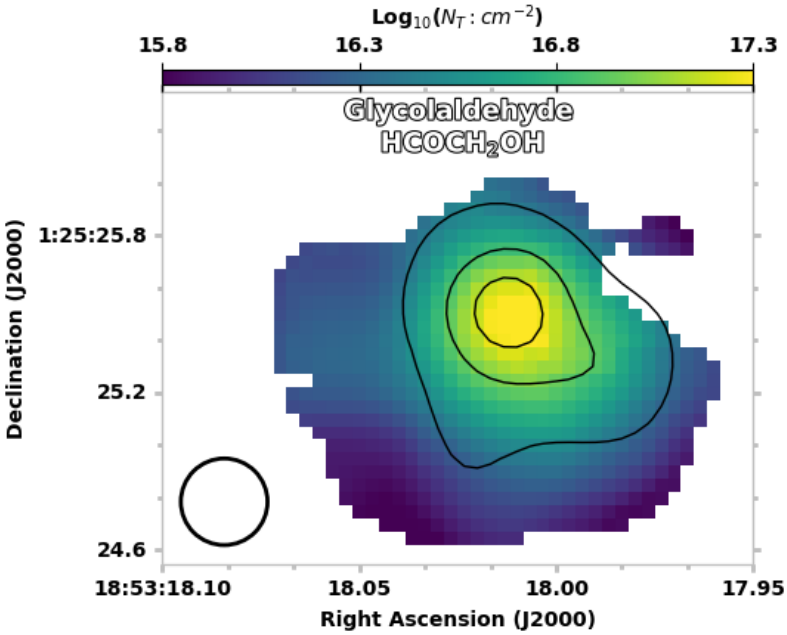


Fig. 4.7.— The spatial morphology of glycolaldehyde column densities produced by SAMER.

especially visible in Figure 4.6 which shows the spatial morphology of acetic acid; the abundance of this molecule falls off significantly more quickly than other molecules in colder regions. This is in agreement with the maps of these molecules in El-Abd et al. (2024), where the acetic acid image was also more closely tied to the continuum temperature in NGC 6334I. It is difficult to say, however, whether this speaks more to some gas-phase process enabled by the higher temperature or the increased sublimation of this molecule from grain surfaces.

## 4.6 Conclusions

The initial applications of SAMER to a high mass star-forming region from the CoCCoA survey are very promising. The spectra are by and large well-populated with molecular emission lines that are easily identifiable and capable of being fit with the models produced by `molsim`. The output from SAMER was used to measure physical conditions and kinematics of the region and showed evidence for both bulk rotation of the cloud and outflows driven by the hot core which had previously been speculated upon. The column densities for a number of molecules were measured and, once combined with the column density data from other hot cores in the CoCCoA survey, should prove to be extremely useful for fine-tuning chemical and physical models of such sources.

This work makes use of the following ALMA data: #2019.1.00426.S. ALMA is a partnership of ESO (representing its member states), NSF (USA) and NINS (Japan), together with NRC (Canada) and NSC and ASIAA (Taiwan) and KASI (Republic of Korea), in cooperation with the Republic of Chile. The Joint ALMA Observatory is operated by ESO, AUI/NRAO and NAOJ. The National Radio Astronomy Observatory is a facility of the National Science Foundation operated under cooperative agreement by Associated Universities, Inc. This research made use of NASA's Astrophysics Data System Bibliographic Services, Astropy, a community-developed core Python package for Astronomy (Astropy Collaboration et al. 2022), and APLpy, an open-source plotting package for Python (Robitaille & Bressert 2012). Support for this work was provided by the NSF through the Grote Reber Fellowship Program administered by Associated Universities, Inc./National Radio Astronomy Observatory.

# Chapter 5

# Conclusions

It is possible to use the interplay between the observable properties of massive star-forming regions and their molecular inventory to constrain the physical conditions and mechanisms of the massive star formation process.

In Chapter 2 we demonstrated that structural isomers may be useful tools to constrain the evolving physical conditions of the star-forming environment by observing a bifurcation in the relative abundances of the three $C_2H_4O_2$ isomers: methyl formate, glycolaldehyde, and acetic acid. As these molecules are composed from the same atoms, any difference in their formation mechanisms can be attributed to the physical environment in which they are found as opposed to the initial atomic inventory. No cause for this observed trend is immediately apparent, however, as methyl formate and acetic acid do not share a singular precursor species that plays a major role in their formation, though all three of these isomers compete for products from the photo-dissociation of methanol. A difference in temperature that causes the different isomers to evaporate from the grains at different times is also unlikely to be wholly responsible for this trend given the available data. While evidence for this bimodal distribution was compelling, it was identified using data from a disparate

set of sources in the literature combining measurements from both single-dish and interferometric observations, along with our own measurements in two regions of NGC 6334I. The relatively small number of data points, combined with the patchwork nature of the data used, meant that expanding on this initial analysis necessitated a different approach - a larger number of measurements with a self-consistent set of observations.

The thorough molecular emission models that were constructed for NGC 6334I were useful for a number of purposes and resulted in several collaborations. The most prolific use case proved to be searches for new interstellar molecules; this includes the novel detection of methoxymethanol by McGuire et al. (2017b, , including S. El-Abd) as well as the non-detection of HCCSH and $H_2CCS$ (McGuire et al. 2019, , including S. El-Abd), which used my emission models to identify unblended transitions of the target molecules. The models were also used in a study of the amide species in NGC 6334I, which highlighted their potential as biomolecule precursors (Ligterink et al. 2020, ,including S. El-Abd).

In Chapter 3 we present the initial results from our newly-developed automated fitting routine - the Simultaneous Autonomous Molecular Emission Resolver (SAMER) - designed to treat the crowded molecular line spectra from star-forming regions. We have demonstrated that the optically-thick line forests of NGC 6334I could be adequately treated by such a routine while greatly accelerating the rate at which measurements could be made for parameters such as the excitation temperature, velocity, and column density. We have also shown how making measurements of these parameters on a per-pixel basis is necessary to accurately describe the spatial variation in these quantities as opposed to the widely-adopted methodology of creating moment maps from a single molecular transition. Star-forming regions are kinematically

complex due to energetic processes like outflows and accretion outbursts; attaining a better understanding of the impact such processes have on the surrounding medium is a necessary step to understanding the wider picture of massive star formation. Applying this routine to NGC 6334I-MM1 and -MM2 provided additional evidence that the previously-observed bifurcation in the abundances of the $C_2H_4O_2$ isomers was an accurate representation, and not a consequence of the small sample size of data points. That this trend is still apparent between two star-forming regions separated by only $\sim 4000$ au provides potential constraints on how the physical conditions differ between these two regions. Efforts to reproduce the observed methyl formate : glycolaldehyde ratios in this work were carried out by collaborators who were able to successfully simulate the appropriate abundances in chemical models (Shope et al., submitted, including S. El-Abd). SAMER has already proven effective in other applications such as the detection of new interstellar molecules, as shown by the novel detection of methoxyethanol (Fried et al., accepted for publication, including S. El-Abd). The routine is freely available to the astronomical community as part of the `molsim` Python package.

In Chapter 4 we present a preliminary application of SAMER to a new high-mass star-forming region, G34.41+0.24. Images of the excitation temperature, linewidth, and velocity were presented, in which we found evidence for both measuring the bulk rotation of the cloud and an outflow that is being driven by the hot core of G34.41+0.24. Images of the $C_2H_4O_2$ isomers were presented and qualitatively matched the findings of our previous work. Acetic acid, in particular, appears to show the same morphology in both this source and NGC 6334I. This was promising evidence that SAMER is a suitable tool for exploring the data that will be produced by future surveys of star-forming regions.

## 5.1 Next Steps

The next logical step from this work is to apply SAMER to a self-consistent, interferometric survey of massive star-forming regions to better constrain their physical conditions and processes through a more thorough exploration of their molecular emission spectra. Characterizing the molecular emission across the entirety of a large set of regions on a pixel-by-pixel basis would previously have been an unrealistic task due to the time-consuming nature of fitting spectra by hand; with our development of SAMER, however, we are now better equipped to deal with such a large amount of data and produce maps of physical parameters that are unbiased by a select number of data points. To this end, we have recently had a proposal accepted for just such a survey with ALMA, titled Complex Chemistry in hot Cores with ALMA (CoCCoA). The data for this project are still being observed, but preliminary results have already been published for fourteen sources in which complex molecular species have been measured (Chen et al. 2023), in addition to the analysis of G34.41+0.24 presented in Chapter 4 of this work. Once all of the observations and data have been taken for each of the sources in our sample, we will be able to efficiently derive physical properties for all of the sources, which will greatly simplify the task of identifying trends across a number of molecules in a similar manner to what we have done here for the $C_2H_4O_2$ isomers, if such trends exist. Other parameters such as temperature and internal motions of the gas are factors that astronomers have not previously observed across a large sample of high-mass star-forming regions with consistent observational properties; these measurements should prove invaluable for identifying the physical conditions that give rise to massive stars. Generating such a wealth of data should greatly aid models of hot core chemistry in placing constraints on the formation routes and physical conditions that give rise to observed chemical abundances, improving

our understanding of the massive star formation process. The data we generate may even have applications as training sets for machine learning models which will provide new methods of astronomical analysis.

# Chapter 6

# Appendices

# A1 Appendix for Chapter 2

## A1.1 Beam Corrections

Fuente et al. (2014) provide column densities for both methyl formate and glycolaldehyde in NGC 7129 FIRS 2. For methyl formate, sufficient transitions were observed to allow the source size to vary, and they fit a source size of $0.12''$ (Table 3 of Fuente et al. 2014). For glycolaldehyde, sufficient transitions were seen to derive a column density, but not to fit a source size, and Fuente et al. (2014) provided instead a beam-averaged column density. Here, we have made the assumption that the glycolaldehyde and methyl formate will have a similar spatial distribution, and have corrected the reported glycolaldehyde abundance assuming a source size of $0.12''$, matching that of methyl formate.

## A1.2 Full NGC 6334I Simulations for Selected Positions

As described in §2.2.2, we conducted an exhaustive search of the databases to identify all lines belonging to known interstellar species in the spectra from NGC 6334I MM1 and MM2 in an attempt to simultaneously identify those lines of methyl formate, glycolaldehyde, and acetic acid most appropriate (unblended and optically thin) for conducting a column density analysis. The full results of the model are beyond the scope of this paper, and for all the species except these targets, the analysis was done by-eye: the primary goal was line identification, not quantification. Nevertheless, the resulting agreement of the model with the observations is excellent, even with the assumption of a uniform $T_{ex}$, $\Delta V$, and $v_{lsr}$ for all species.

The results are shown in the following pages. Figures 6.1 through 6.8 display the observational spectra toward MM1-i, and Figures 6.9 through 6.16 display those to-

ward MM2-ii, with the total simulation as well as the individual simulations of methyl formate, glycolaldehyde (MM1-i only), and acetic acid overlaid. The total simulation includes these species. While the simulation accounts for opacity effects, there are several issues that cannot be properly accounted for without a full radiative transfer model that is beyond the scope of this analysis. These are seen most prominently in the optically thick lines of $CH_3OH$. First, for many of these lines there is substantial self-absorption that the model does not account for, resulting in 'flat-topped' profiles in the model that do not match the observations for the highest optical-depth lines. Second, these molecules are so abundant that their emission appears to also include non-trivial contributions from populations with $T_{ex}$ differing from 135 K by about $\pm$20 K. As a result, some of these optically thick lines are over-predicted, and some under-predicted (depending on the species), by this comparatively simple model.

Thus, while the overall model is not perfect for the optically thick lines, it serves its purpose well: it is a zeroth-order analysis intended to help identify unblended lines. Given the assumptions of uniform excitation and lineshapes for every species, and the by-eye analysis, we feel the fit is excellent, and completely fulfills its purpose. These spectra demonstrate not only how line-rich the source is, but also how many lines are not easily assigned to known interstellar species.

The transitions of methyl formate, glycolaldehyde, and acetic acid used for the column density analysis are marked with asterisks. As described in the Main Text, these were chosen as they appeared the least blended with other lines (including shoulders), and were not extremely optically thick.

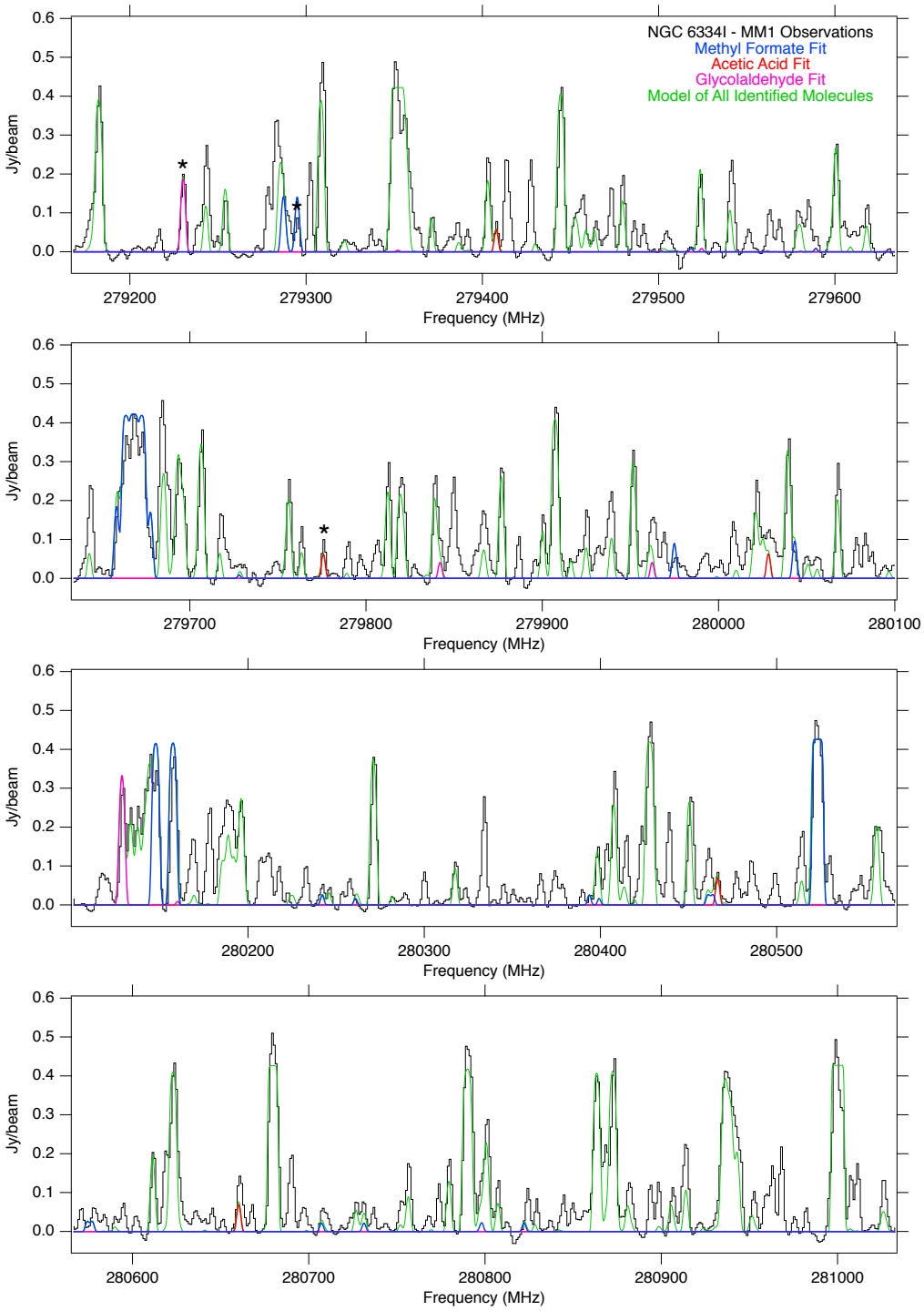


Fig. 6.1.— Spectra extracted toward NGC 6334I MM1-i (black). Overlaid in green is the full model of all assigned molecules in the spectrum (see text), and methyl formate, glycolaldehyde, and acetic acid are shown in color. Transitions marked with an asterisk were identified as the least blended and optically thin, and were used for the column density analysis (see Table 2.2). Spectra were offset to a $v_{lsr}$ = -7 km s$^{-1}$.

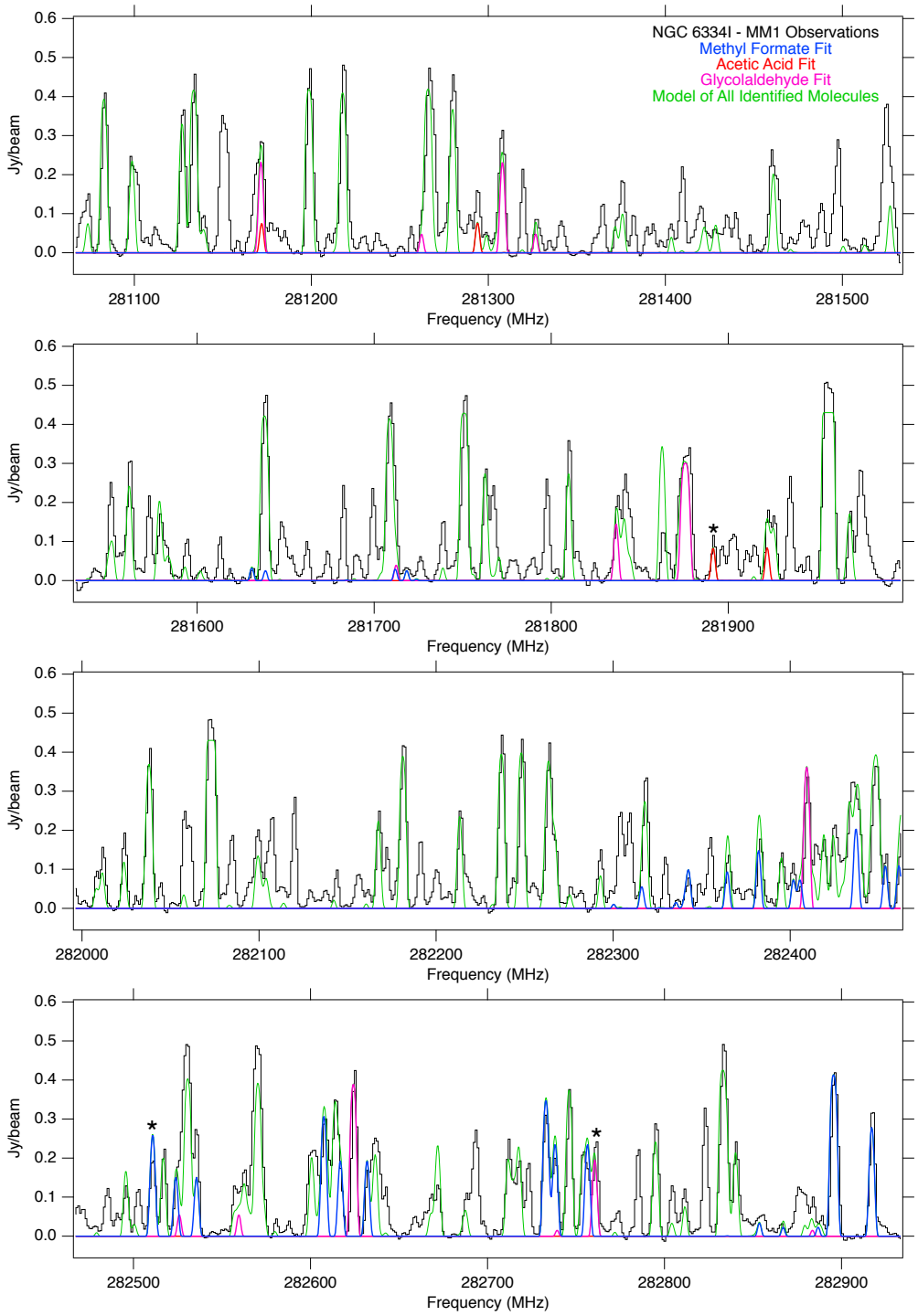


Fig. 6.2.— Spectra extracted toward NGC 6334I MM1-i (black). Overlaid in green is the full model of all assigned molecules in the spectrum (see text), and methyl formate, glycolaldehyde, and acetic acid are shown in color. Transitions marked with an asterisk were identified as the least blended and optically thin, and were used for the column density analysis (see Table 2.2). Spectra were offset to a $v_{lsr}$ = -7 km s$^{-1}$.

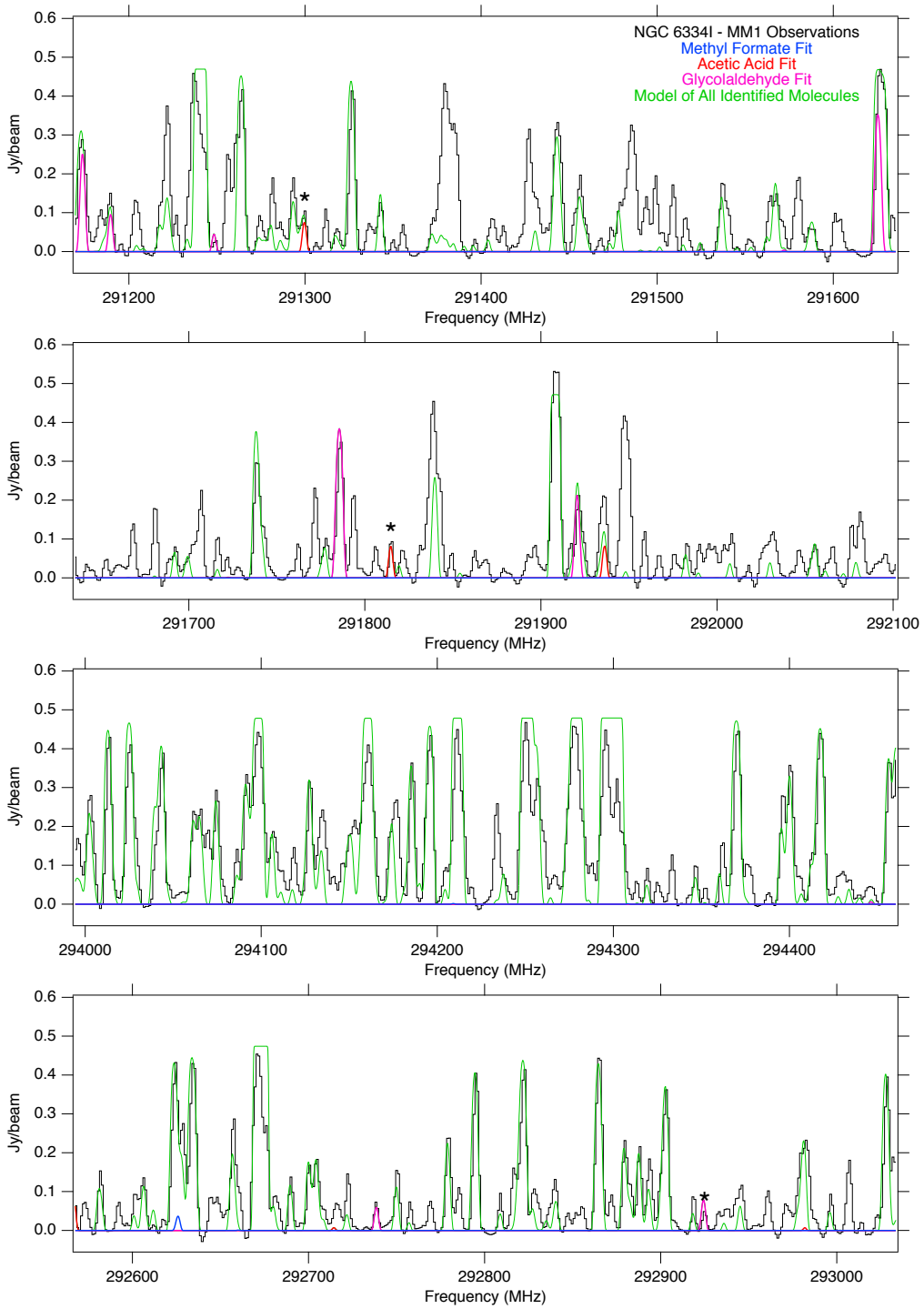


Fig. 6.3.— Spectra extracted toward NGC 6334I MM1-i (black). Overlaid in green is the full model of all assigned molecules in the spectrum (see text), and methyl formate, glycolaldehyde, and acetic acid are shown in color. Transitions marked with an asterisk were identified as the least blended and optically thin, and were used for the column density analysis (see Table 2.2). Spectra were offset to a $v_{lsr}$ = -7 km s$^{-1}$.

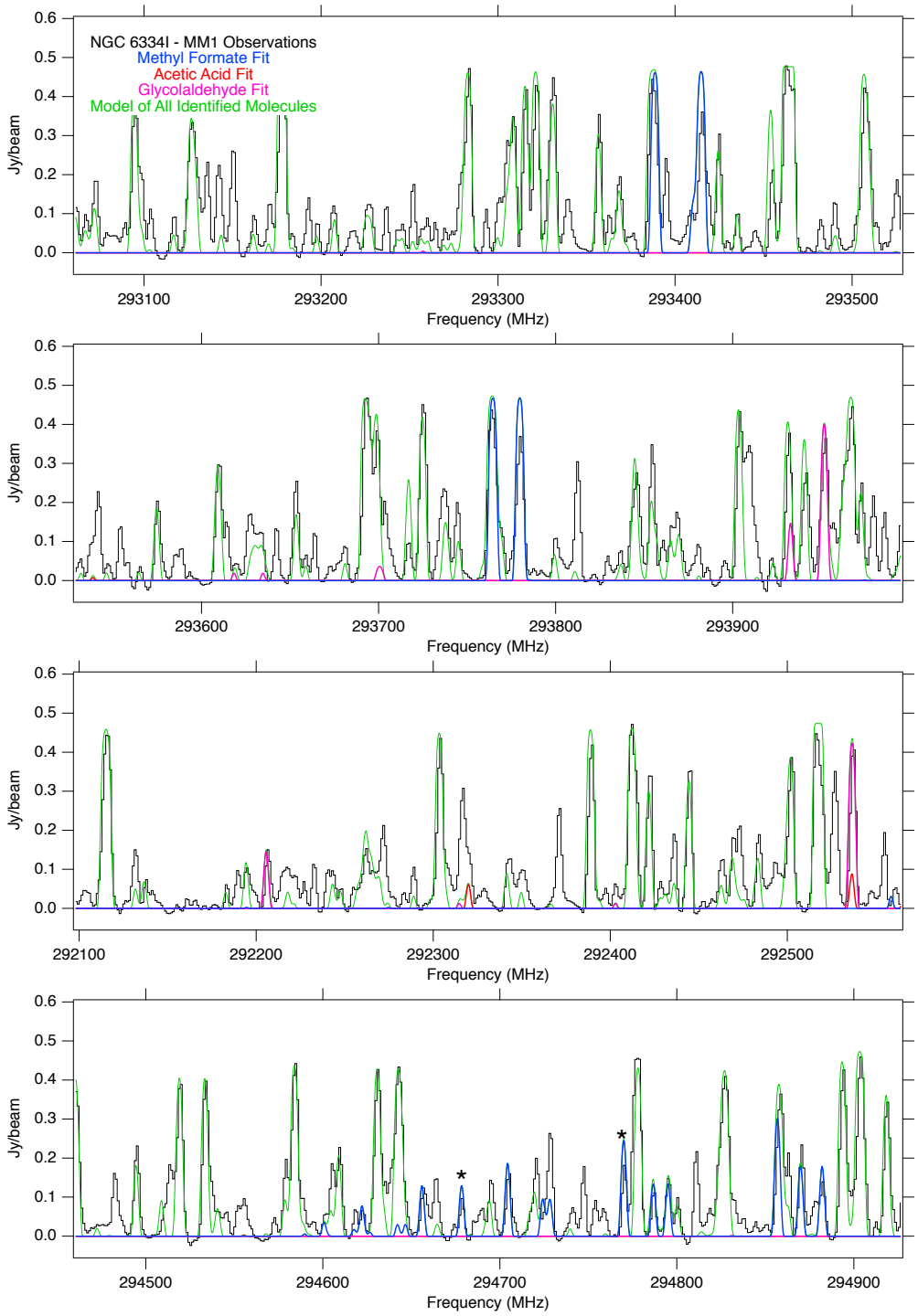


Fig. 6.4.— Spectra extracted toward NGC 6334I MM1-i (black). Overlaid in green is the full model of all assigned molecules in the spectrum (see text), and methyl formate, glycolaldehyde, and acetic acid are shown in color. Transitions marked with an asterisk were identified as the least blended and optically thin, and were used for the column density analysis (see Table 2.2). Spectra were offset to a $v_{lsr}$ = -7 km s$^{-1}$.

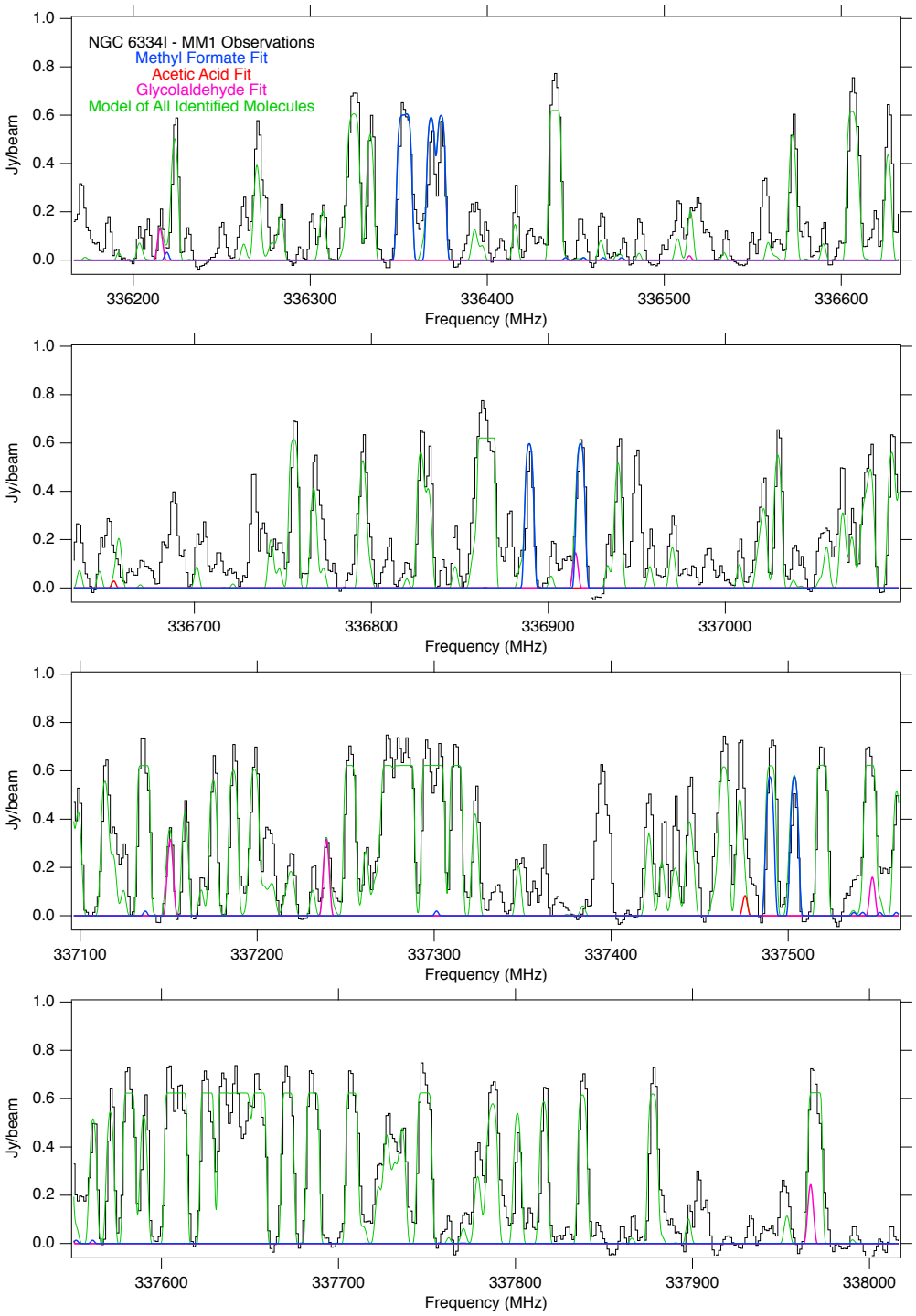


Fig. 6.5.— Spectra extracted toward NGC 6334I MM1-i (black). Overlaid in green is the full model of all assigned molecules in the spectrum (see text), and methyl formate, glycolaldehyde, and acetic acid are shown in color. Transitions marked with an asterisk were identified as the least blended and optically thin, and were used for the column density analysis (see Table 2.2). Spectra were offset to a $v_{lsr}$ = -7 km s$^{-1}$.

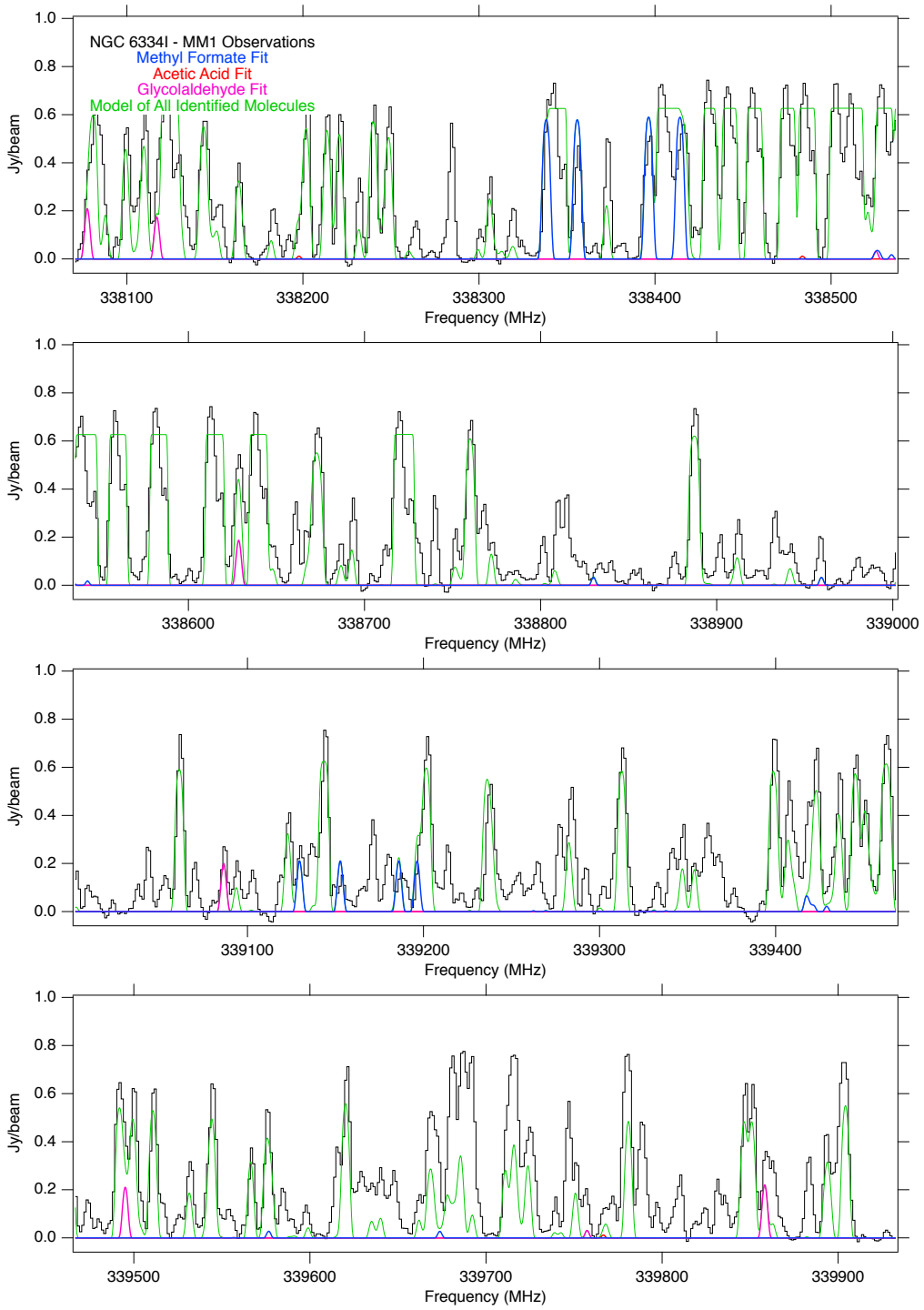


Fig. 6.6.— Spectra extracted toward NGC 6334I MM1-i (black). Overlaid in green is the full model of all assigned molecules in the spectrum (see text), and methyl formate, glycolaldehyde, and acetic acid are shown in color. Transitions marked with an asterisk were identified as the least blended and optically thin, and were used for the column density analysis (see Table 2.2). Spectra were offset to a $v_{lsr}$ = -7 km s$^{-1}$.

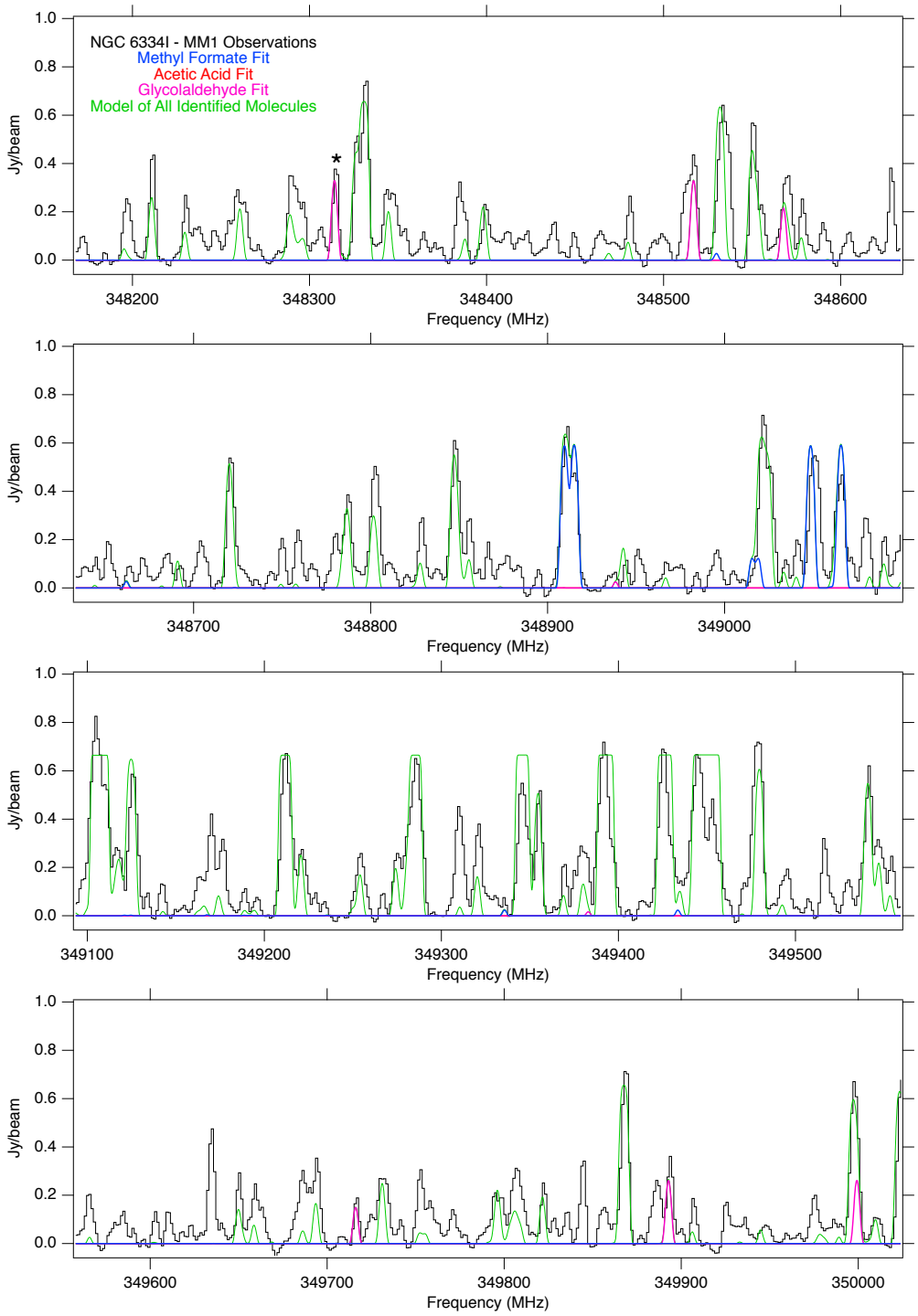


Fig. 6.7.— Spectra extracted toward NGC 6334I MM1-i (black). Overlaid in green is the full model of all assigned molecules in the spectrum (see text), and methyl formate, glycolaldehyde, and acetic acid are shown in color. Transitions marked with an asterisk were identified as the least blended and optically thin, and were used for the column density analysis (see Table 2.2). Spectra were offset to a $v_{lsr}$ = -7 km s$^{-1}$.

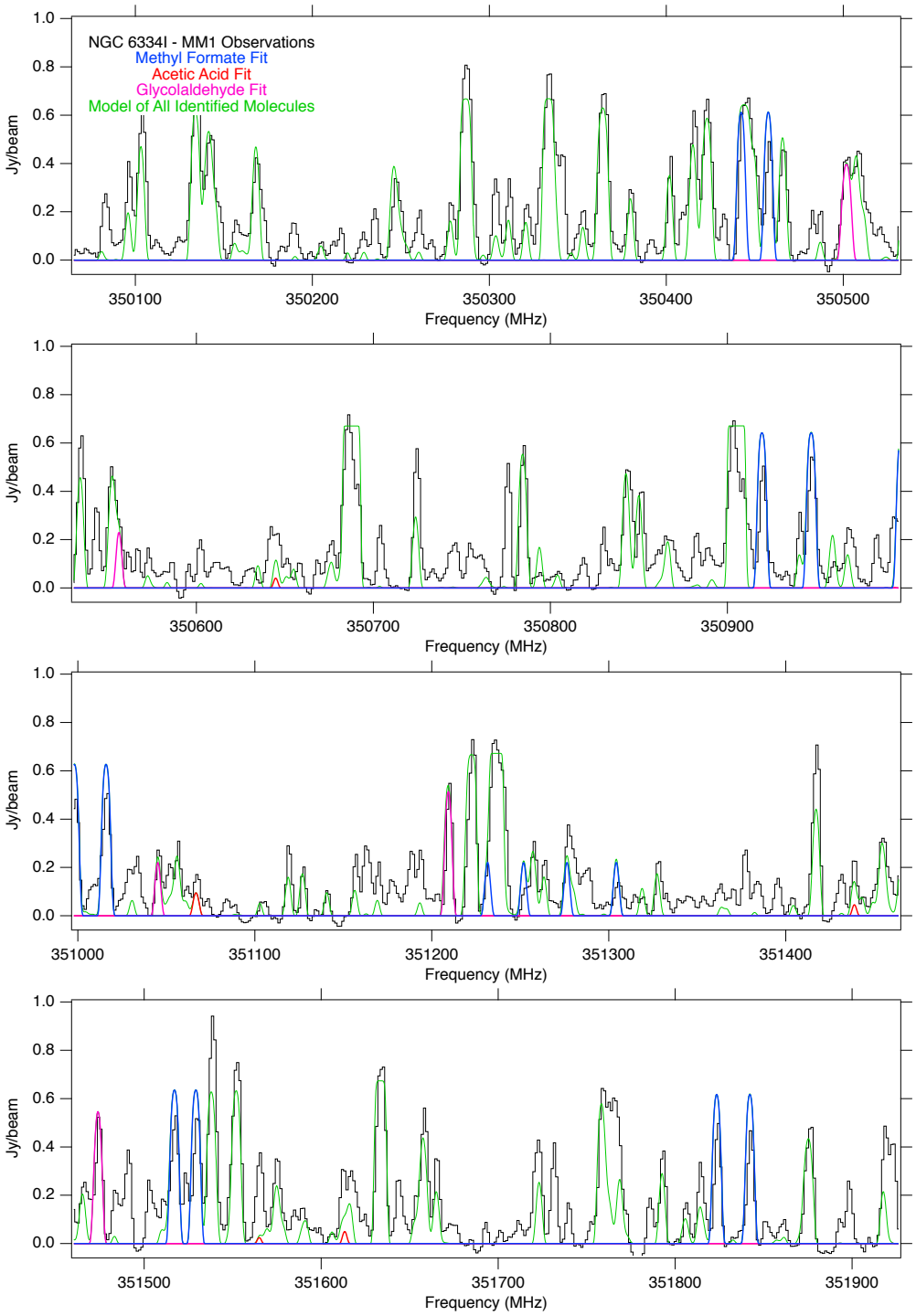


Fig. 6.8.— Spectra extracted toward NGC 6334I MM1-i (black). Overlaid in green is the full model of all assigned molecules in the spectrum (see text), and methyl formate, glycolaldehyde, and acetic acid are shown in color. Transitions marked with an asterisk were identified as the least blended and optically thin, and were used for the column density analysis (see Table 2.2). Spectra were offset to a $v_{lsr}$ = -7 km s$^{-1}$.

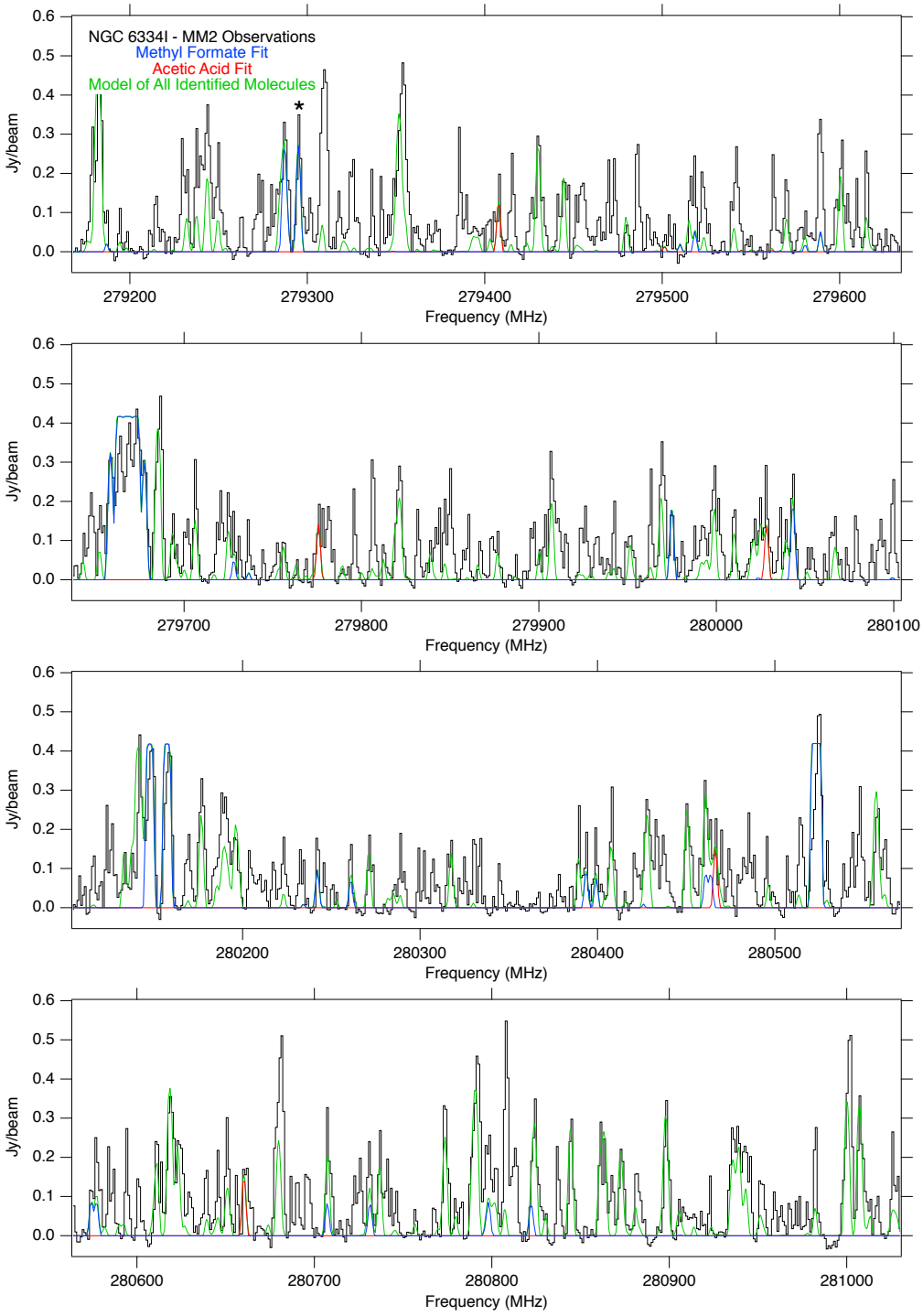


Fig. 6.9.— Spectra extracted toward NGC 6334I MM2-ii (black). Overlaid in green is the full model of all assigned molecules in the spectrum (see text), and methyl formate and acetic acid are shown in color. Transitions marked with an asterisk were identified as the least blended and optically thin, and were used for the column density analysis (see Table 2.2). Spectra were offset to a $v_{lsr}$ = -9 km s$^{-1}$.

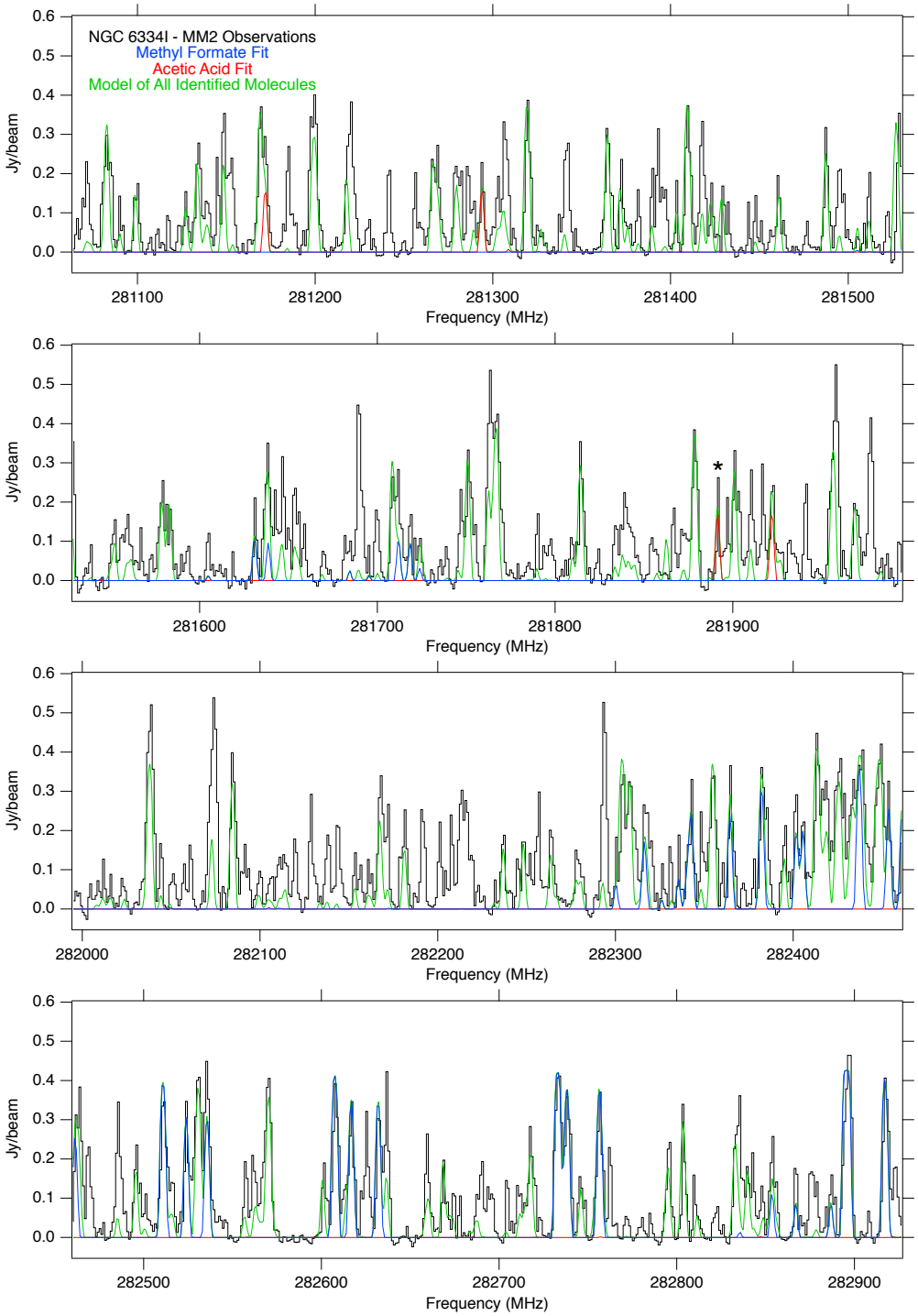


Fig. 6.10.— Spectra extracted toward NGC 6334I MM2-ii (black). Overlaid in green is the full model of all assigned molecules in the spectrum (see text), and methyl formate and acetic acid are shown in color. Transitions marked with an asterisk were identified as the least blended and optically thin, and were used for the column density analysis (see Table 2.2). Spectra were offset to a $v_{lsr}$ = -9 km s$^{-1}$.

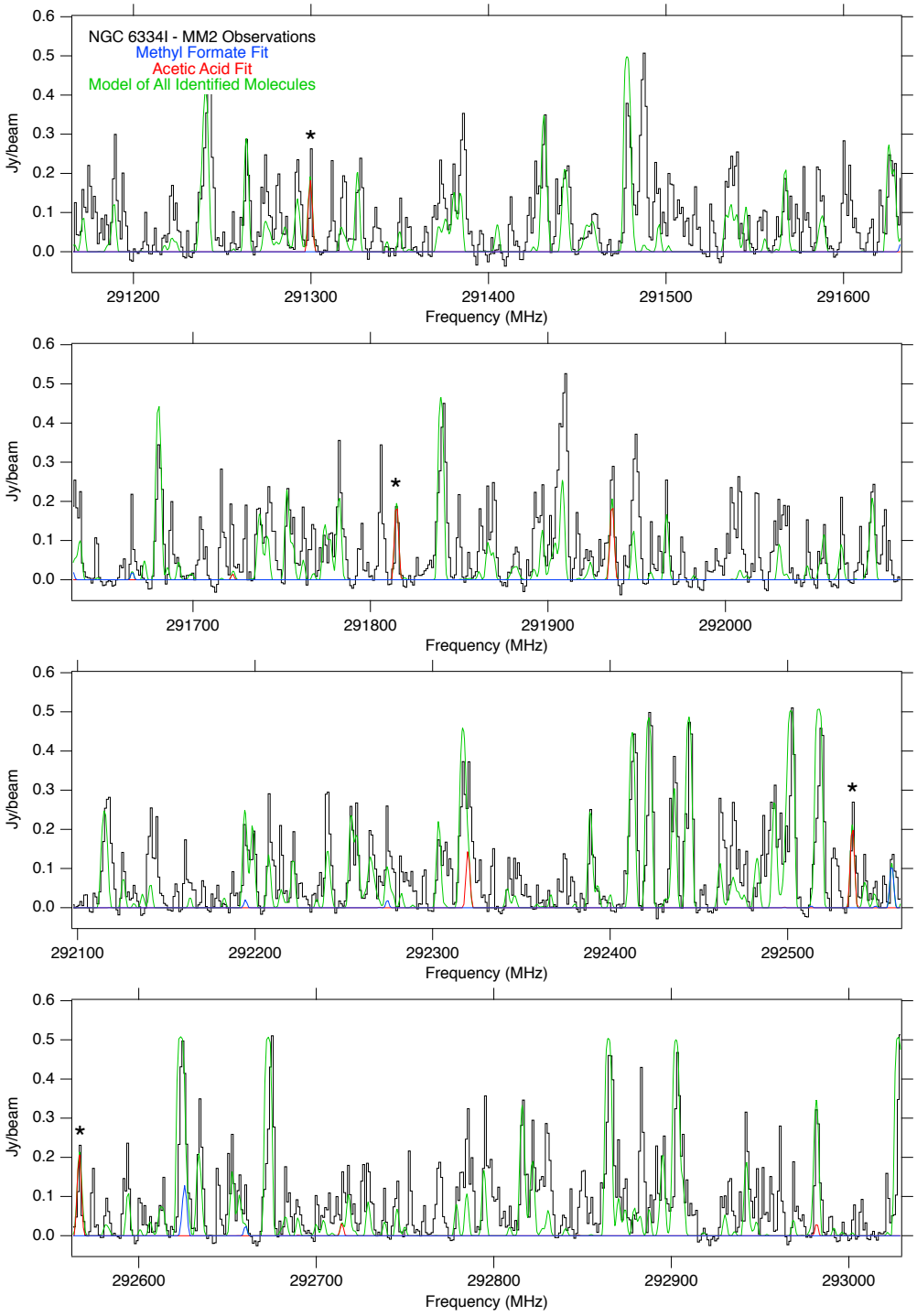


Fig. 6.11.— Spectra extracted toward NGC 6334I MM2-ii (black). Overlaid in green is the full model of all assigned molecules in the spectrum (see text), and methyl formate and acetic acid are shown in color. Transitions marked with an asterisk were identified as the least blended and optically thin, and were used for the column density analysis (see Table 2.2). Spectra were offset to a $v_{lsr}$ = -9 km s$^{-1}$.

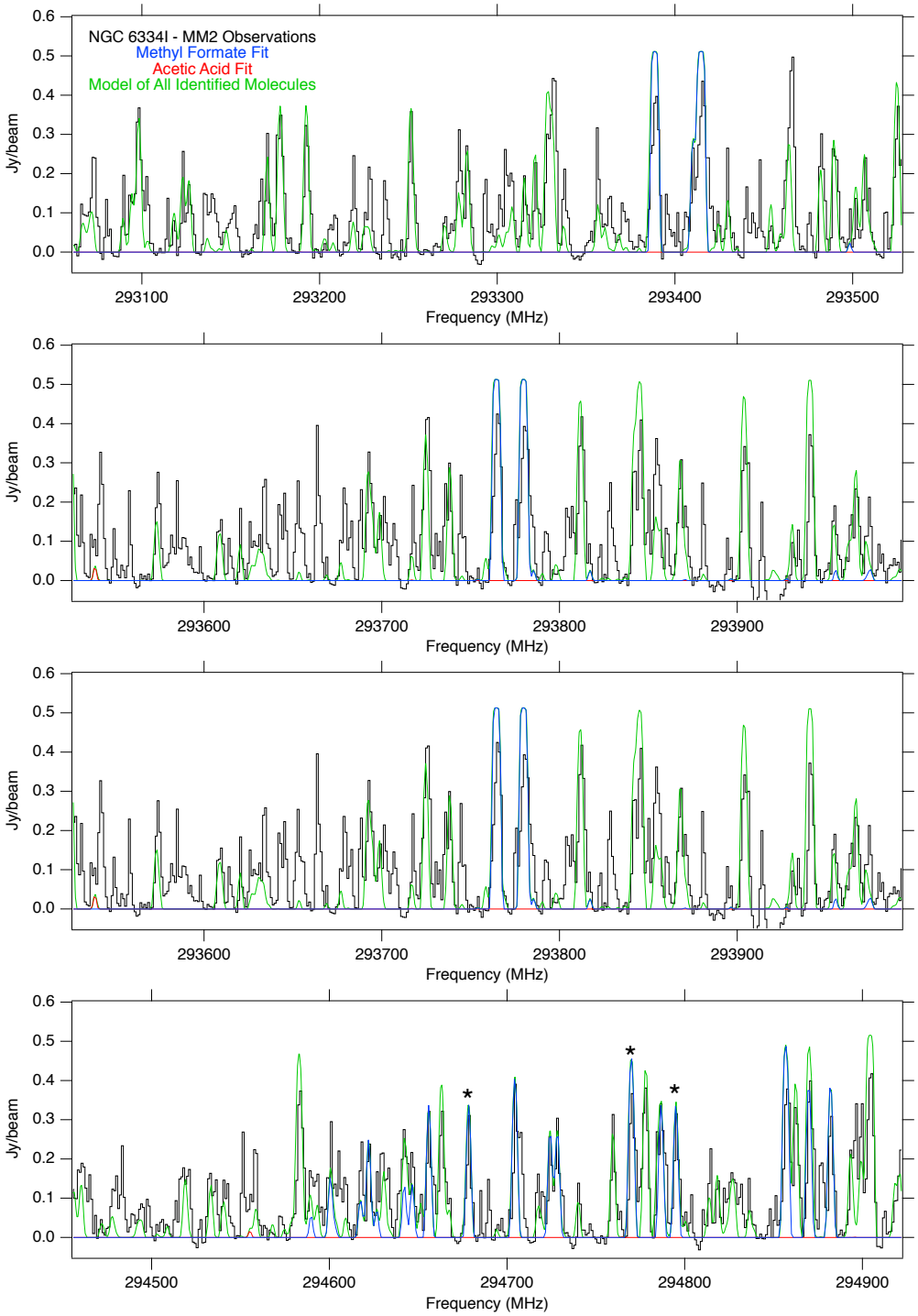


Fig. 6.12.— Spectra extracted toward NGC 6334I MM2-ii (black). Overlaid in green is the full model of all assigned molecules in the spectrum (see text), and methyl formate and acetic acid are shown in color. Transitions marked with an asterisk were identified as the least blended and optically thin, and were used for the column density analysis (see Table 2.2). Spectra were offset to a $v_{lsr}$ = -9 km s$^{-1}$.

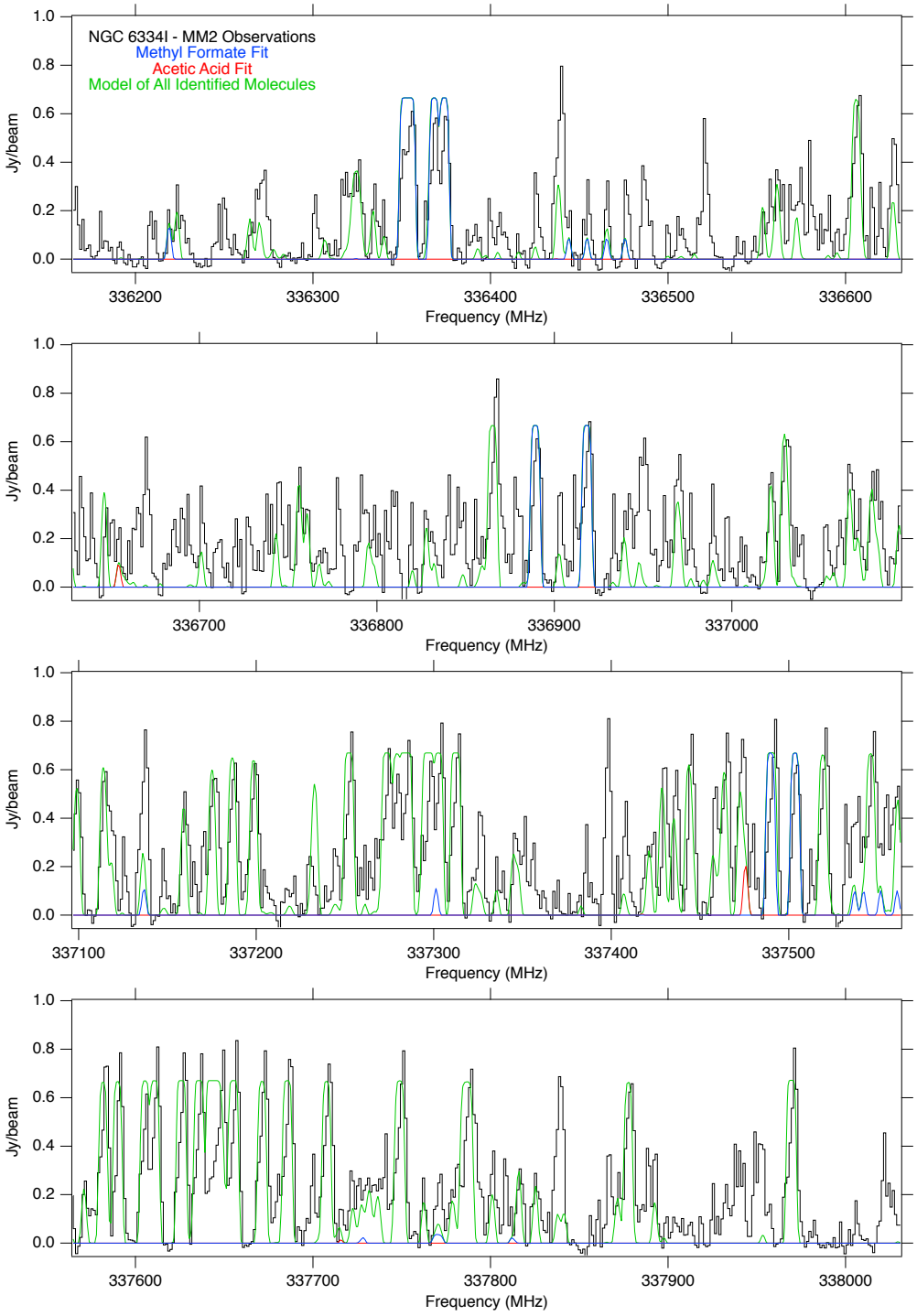


Fig. 6.13.— Spectra extracted toward NGC 6334I MM2-ii (black). Overlaid in green is the full model of all assigned molecules in the spectrum (see text), and methyl formate and acetic acid are shown in color. Transitions marked with an asterisk were identified as the least blended and optically thin, and were used for the column density analysis (see Table 2.2). Spectra were offset to a $v_{lsr}$ = -9 km s$^{-1}$.

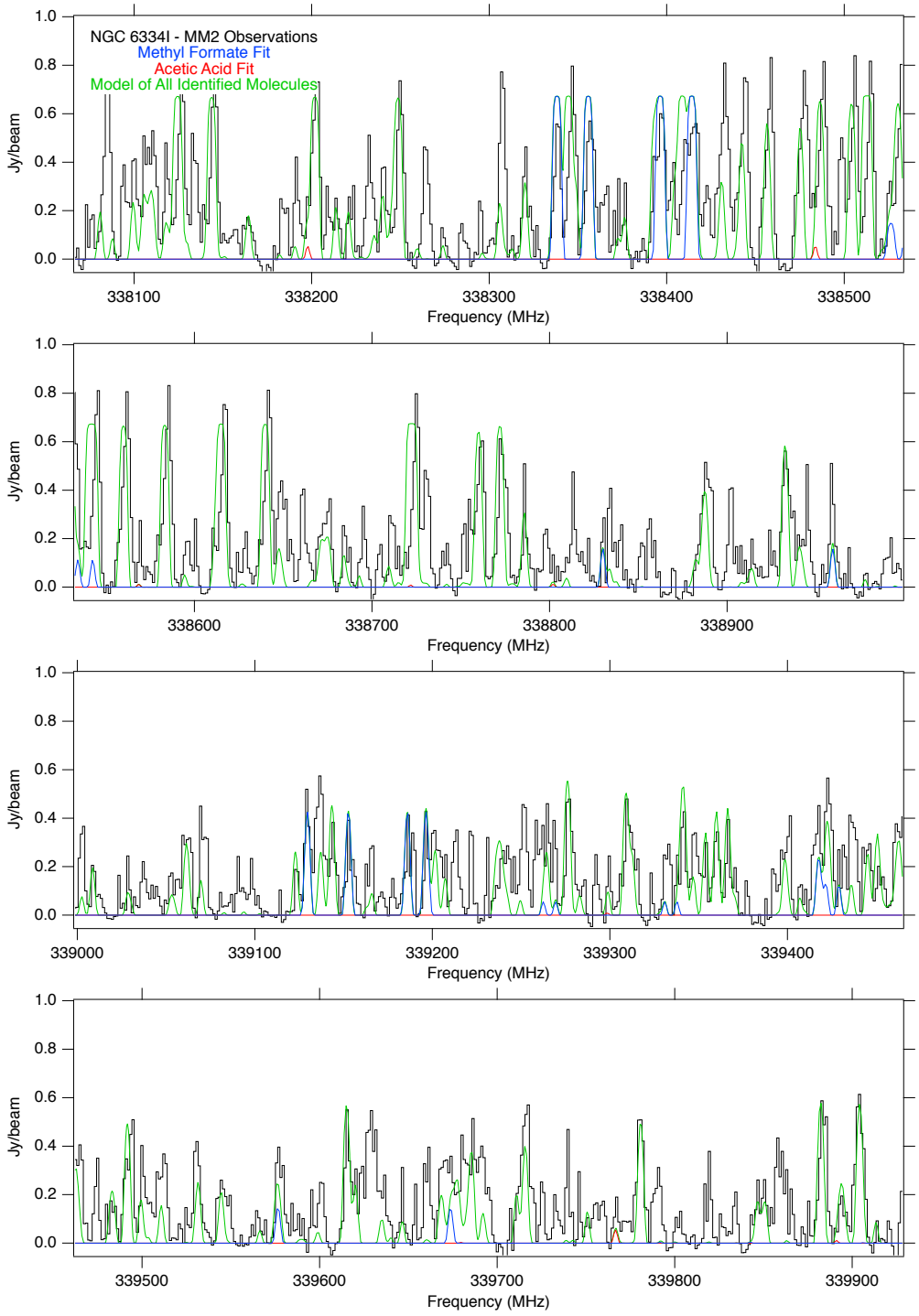


Fig. 6.14.— Spectra extracted toward NGC 6334I MM2-ii (black). Overlaid in green is the full model of all assigned molecules in the spectrum (see text), and methyl formate and acetic acid are shown in color. Transitions marked with an asterisk were identified as the least blended and optically thin, and were used for the column density analysis (see Table 2.2). Spectra were offset to a $v_{lsr}$ = -9 km s$^{-1}$.

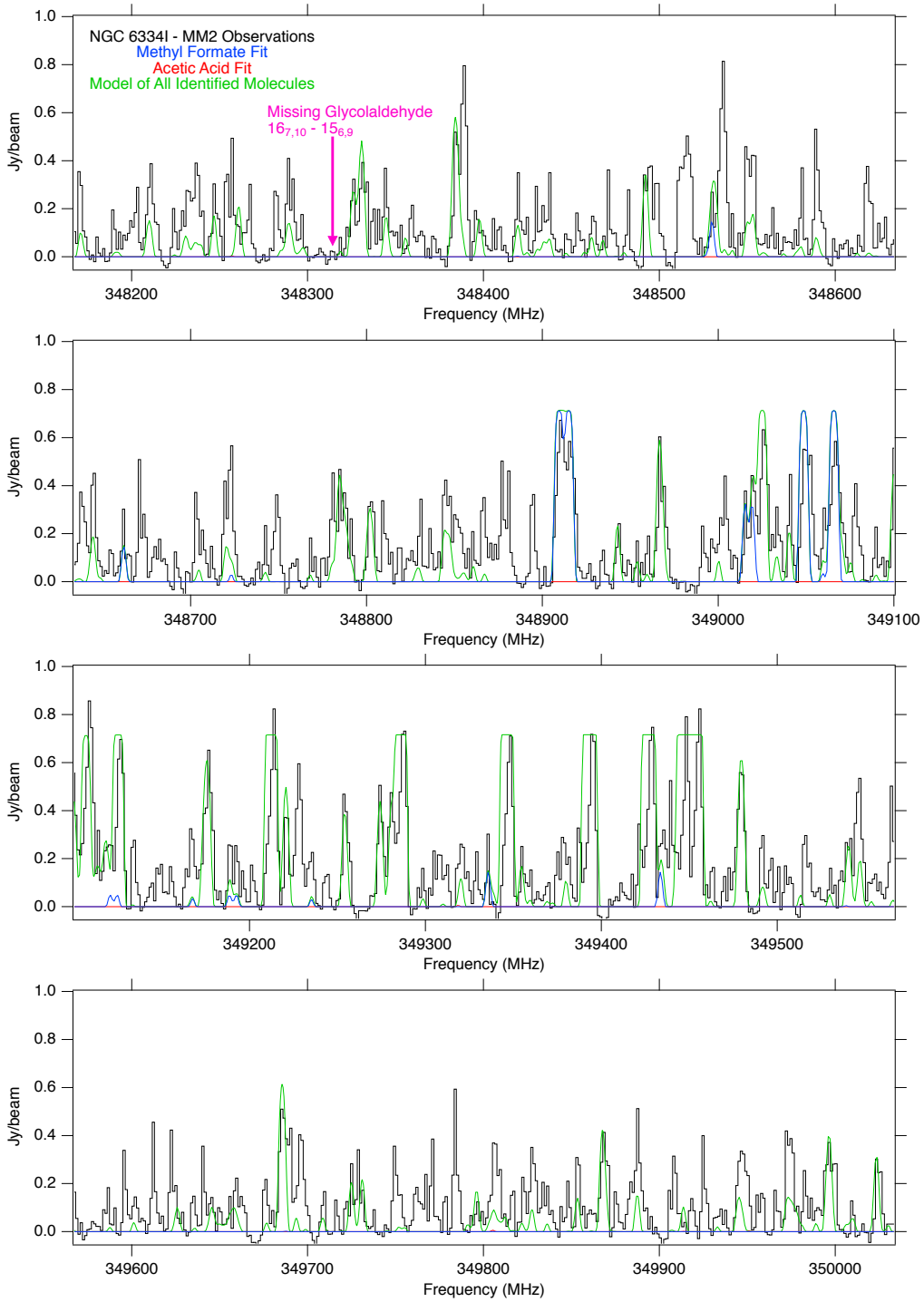


Fig. 6.15.— Spectra extracted toward NGC 6334I MM2-ii (black). Overlaid in green is the full model of all assigned molecules in the spectrum (see text), and methyl formate and acetic acid are shown in color. Transitions marked with an asterisk were identified as the least blended and optically thin, and were used for the column density analysis (see Table 2.2). The location of the missing glycolaldehyde transition used to determine the upper limit is marked with an arrow. Spectra were offset to a $v_{lsr}$ = -9 km s$^{-1}$.

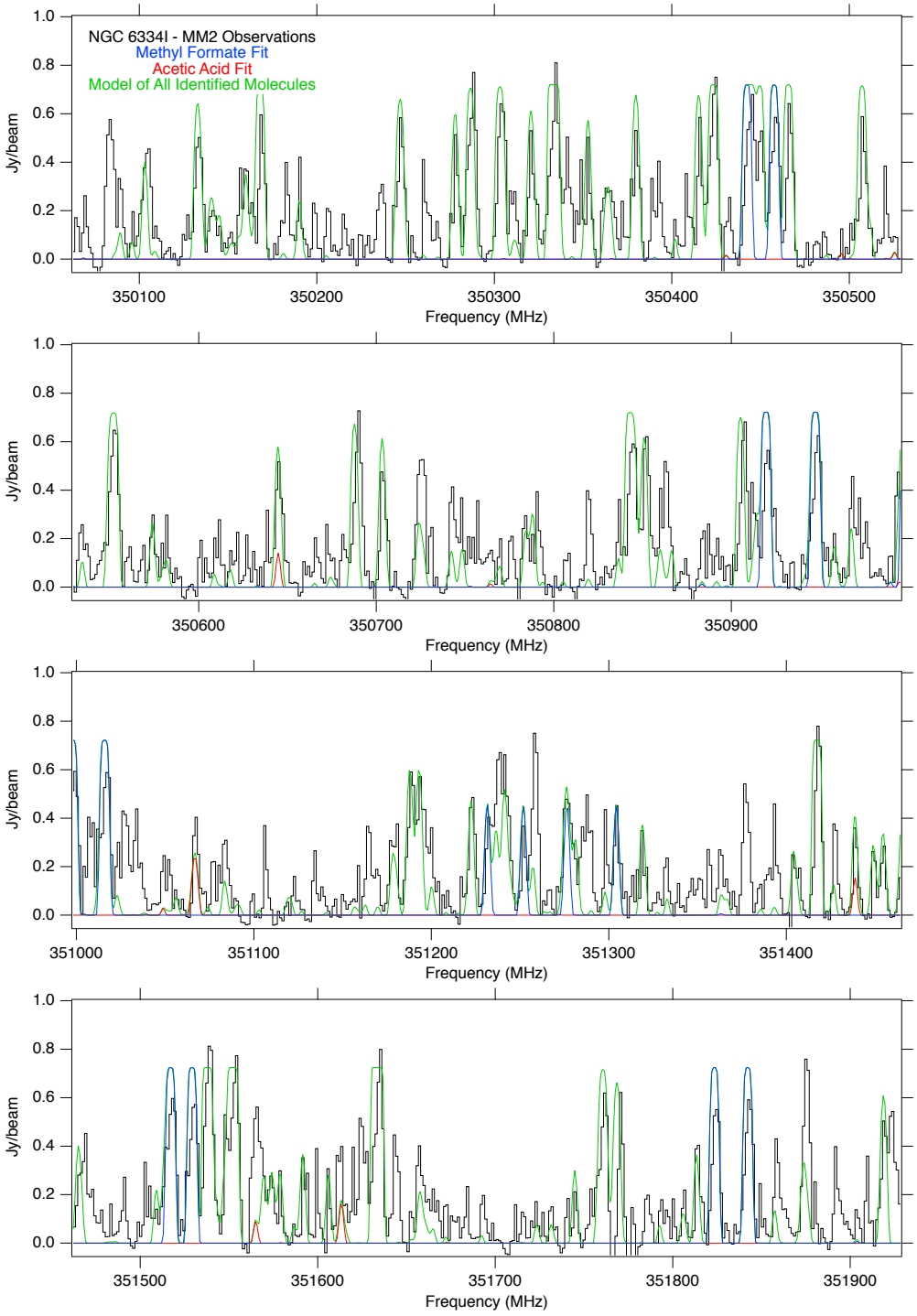


Fig. 6.16.— Spectra extracted toward NGC 6334I MM2-ii (black). Overlaid in green is the full model of all assigned molecules in the spectrum (see text), and methyl formate and acetic acid are shown in color. Transitions marked with an asterisk were identified as the least blended and optically thin, and were used for the column density analysis (see Table 2.2). Spectra were offset to a $v_{lsr}$ = -9 km s$^{-1}$.

# A2 Data for Chapter 3:

## A2.1 Appendix A - Sample Spectra

The spectra from NGC 6334I-MM1 and -MM2 are remarkably varied in both the level of spectral crowding and the overall intensity of the molecular emission. We have selected a number of positions from which to extract spectra to demonstrate this fact in Figures 6.19–6.21, with emission from the $C_2H_4O_2$ isomers highlighted.

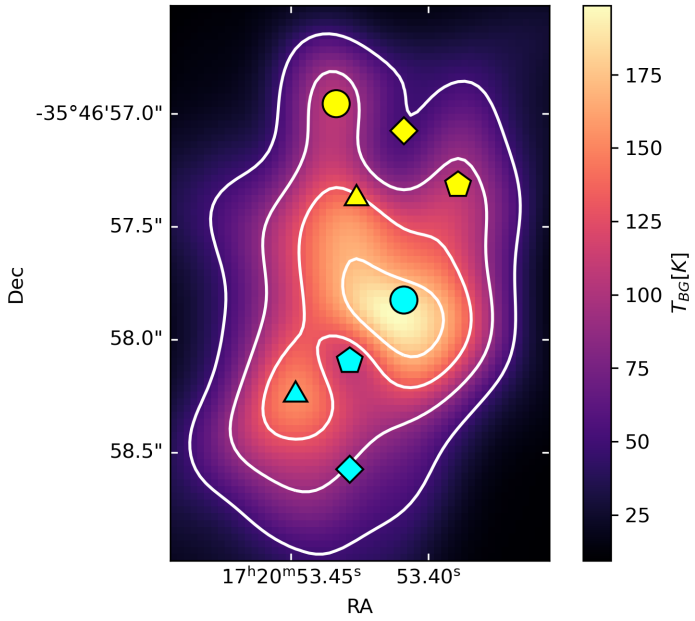


Fig. 6.17.— A sample of spectra were extracted from the marked positions to display the variety in physical conditions across MM1 in Figures 6.19 and 6.20.

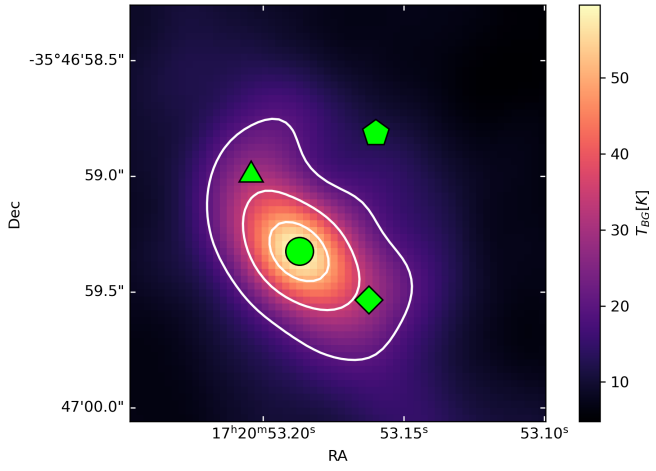


Fig. 6.18.— A sample of spectra were extracted from the marked positions to display the variety in physical conditions across MM2 in Figure 6.21.

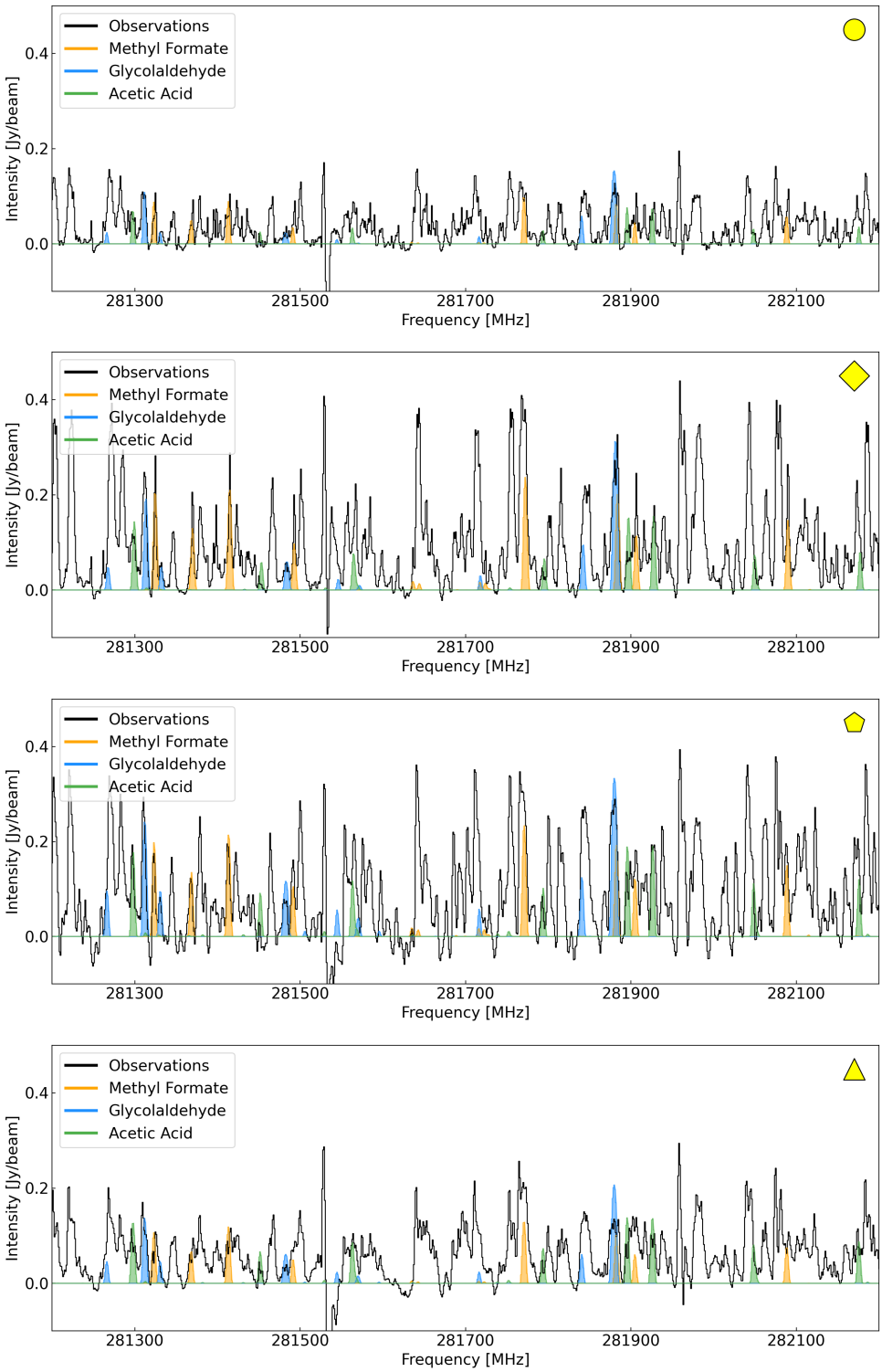


Fig. 6.19.— Spectra of MM1 extracted from the positions marked in Figure 6.17.

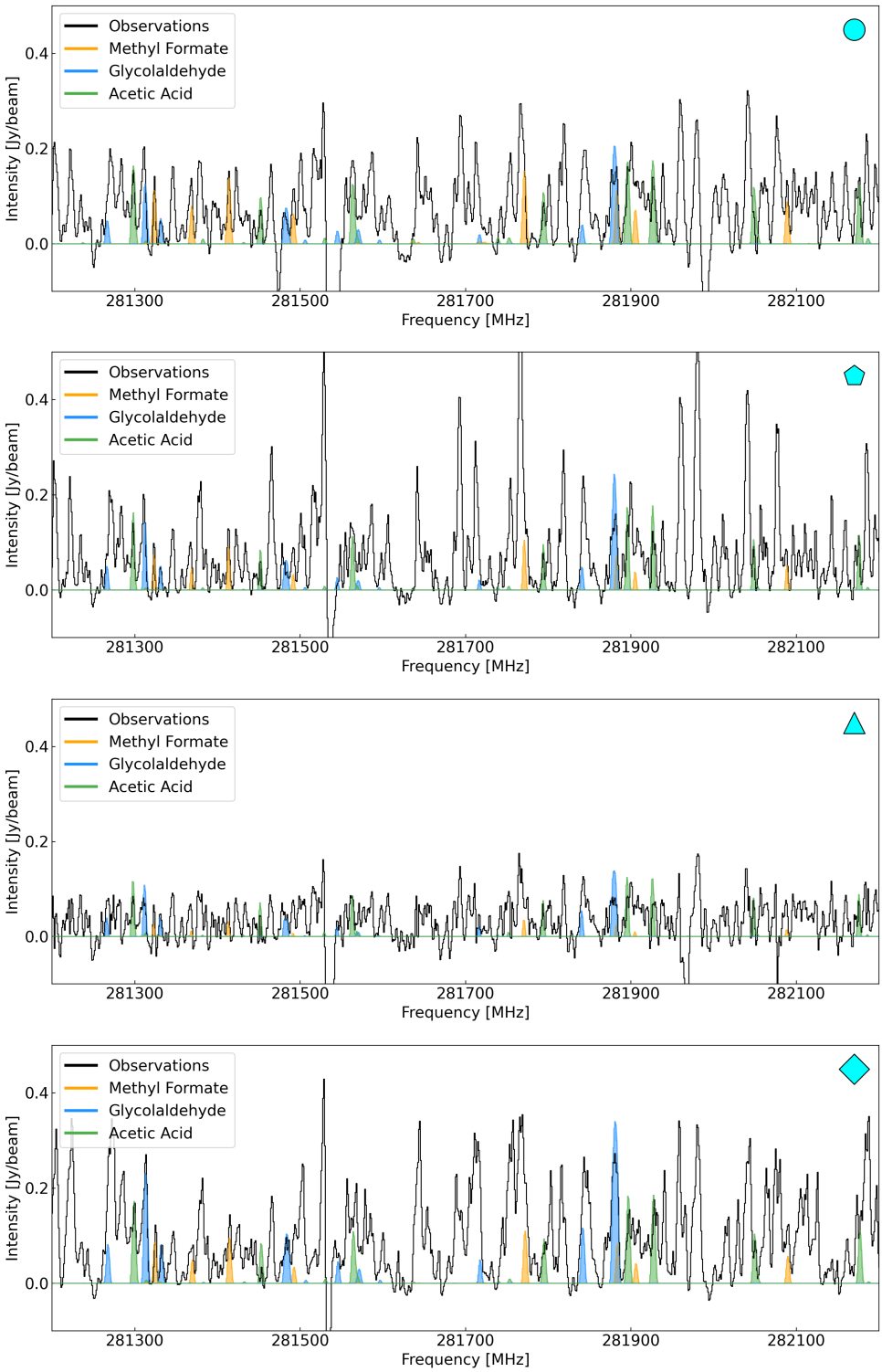


Fig. 6.20.— Spectra of MM1 extracted from the positions marked in Figure 6.17.

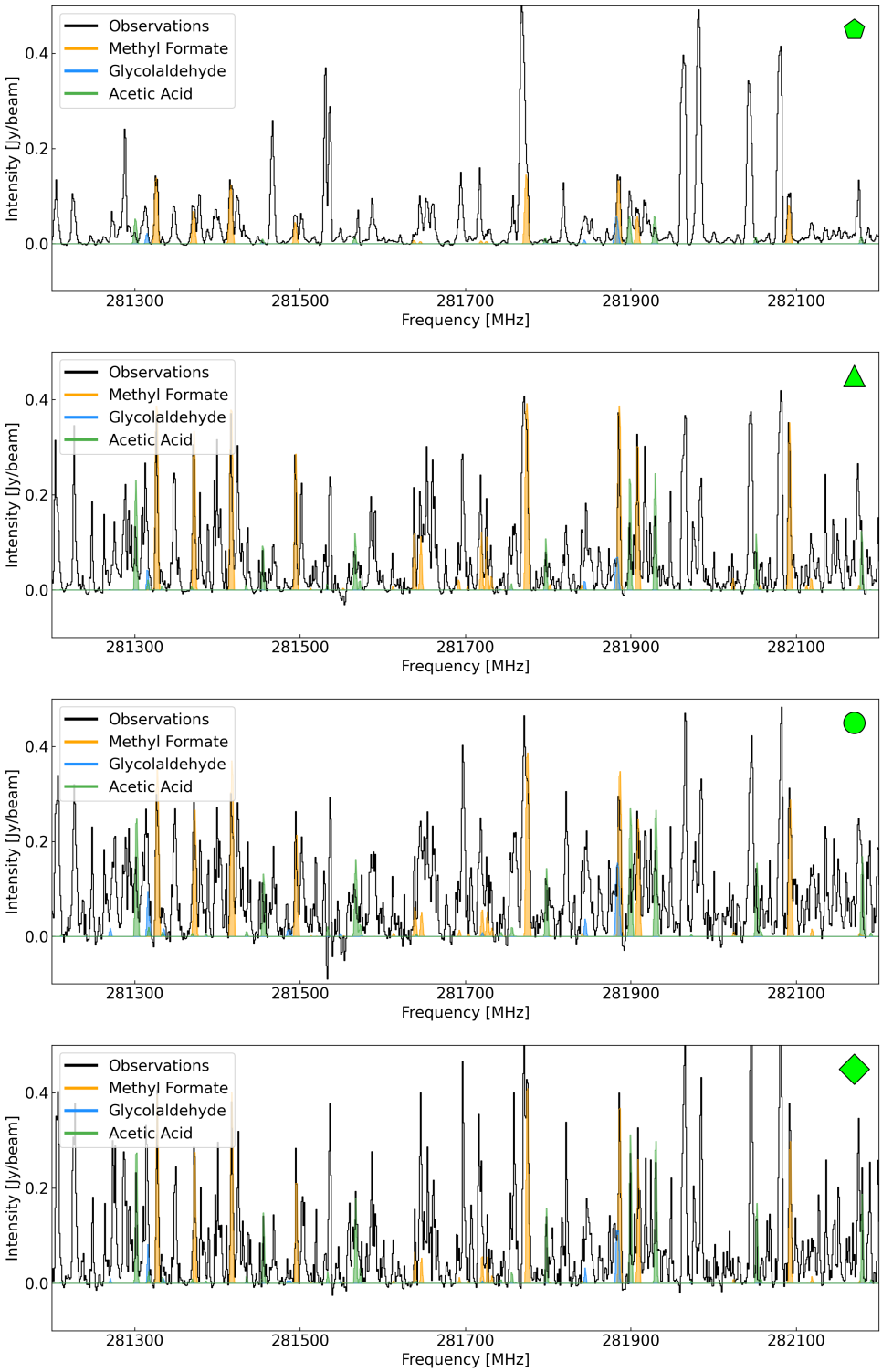


Fig. 6.21.— Spectra of MM2 extracted from the positions marked in Figure 6.18.

## A2.2 Appendix B - Complete Molecule Results and Uncertainties

Images for each of the parameters derived using the fitting routine along with the associated uncertainties are presented in Figures 6.22–6.69 for all of the molecules in the emission model. Note that while each column density image spans 1.2 orders of magnitude, the range is unique for each molecule. The column density uncertainty images cover a uniform range for all molecules and are expressed as a percentage of the value for each pixel. The uncertainty images for the other parameters are expressed in physical units. The same masks described in Section 3.4.2 have been applied to these images.

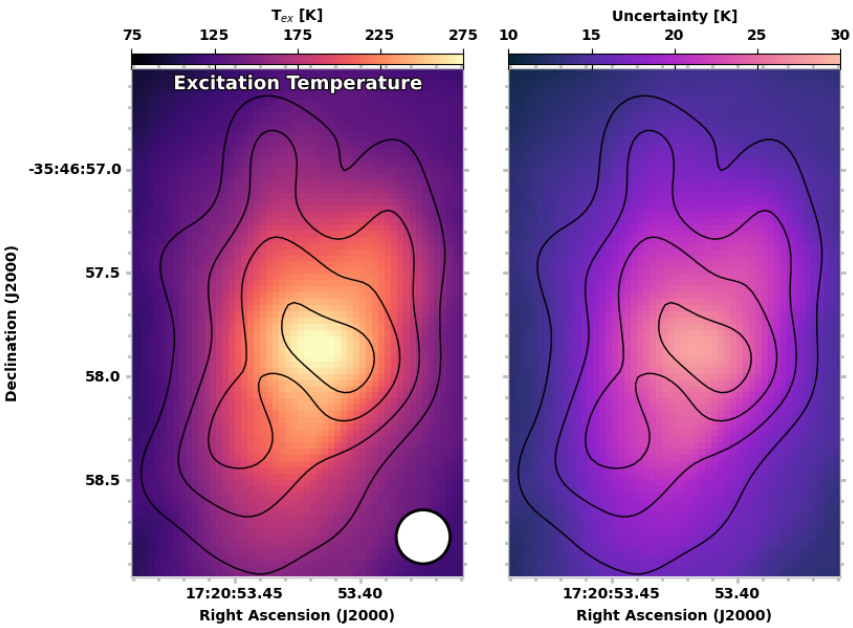


Fig. 6.22.— Excitation temperature (left) and excitation temperature uncertainty (right) images produced by the automated fitting routine for NGC 6334I-MM1.

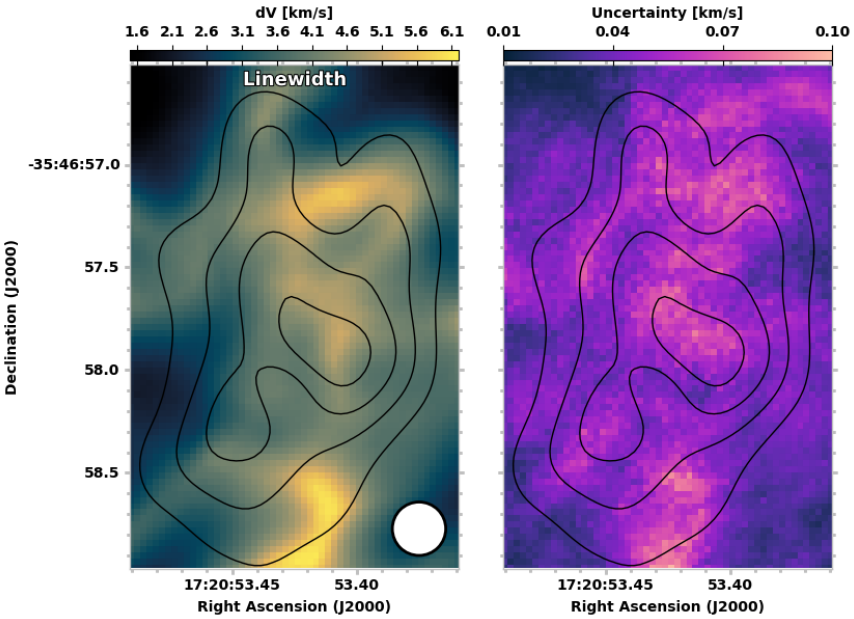


Fig. 6.23.— Linewidth (left) and linewidth uncertainty (right) images produced by the automated fitting routine for NGC 6334I-MM1.

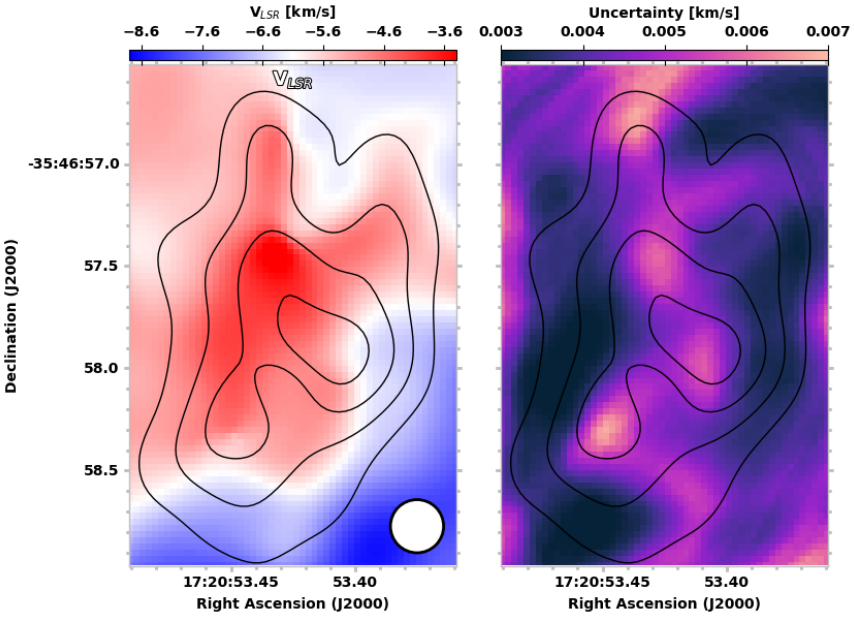


Fig. 6.24.— Velocity (left) and velocity uncertainty (right) images produced by the automated fitting routine for NGC 6334I-MM1.

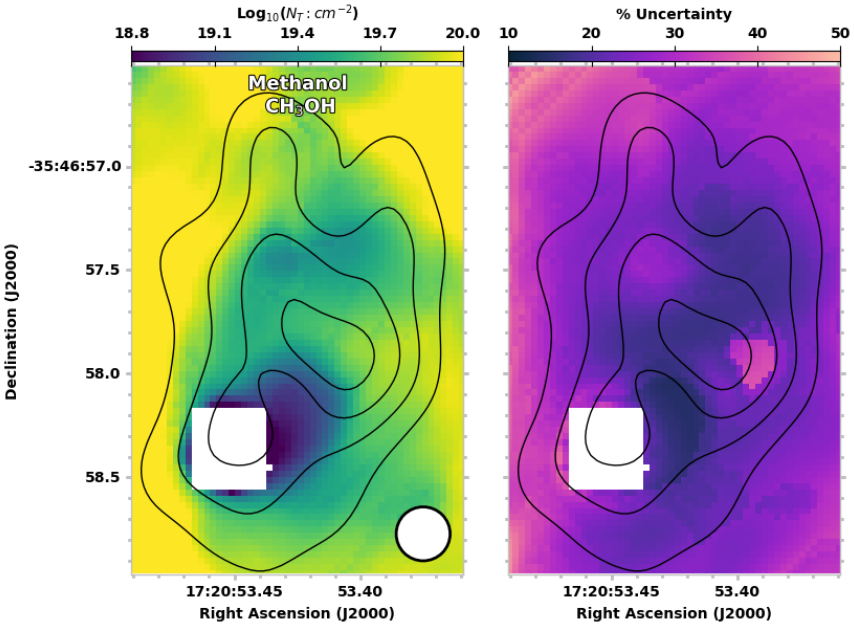


Fig. 6.25.— Column density (left) and column density uncertainty (right) images produced by the automated fitting routine for methanol in NGC 6334I-MM1.

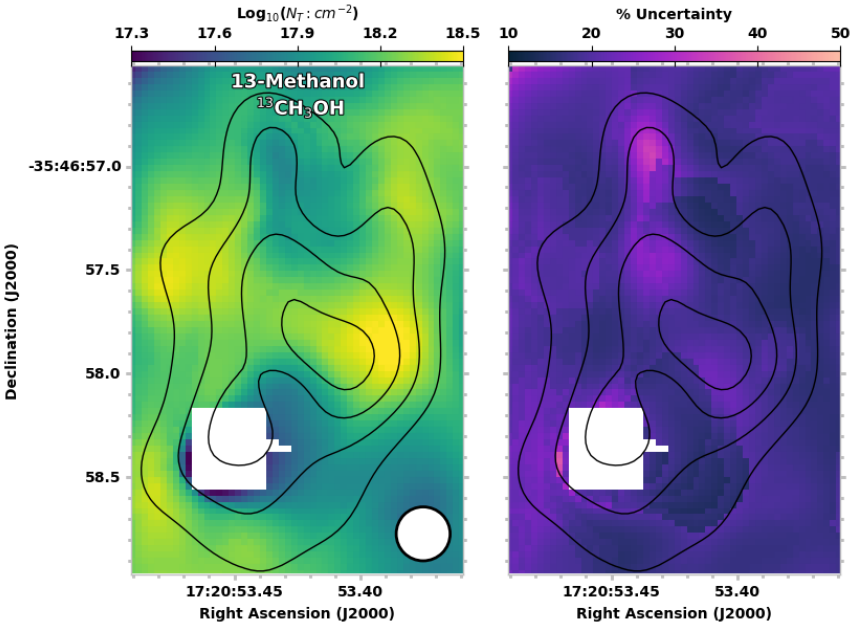


Fig. 6.26.— Same as Figure 6.25 but for 13-methanol.

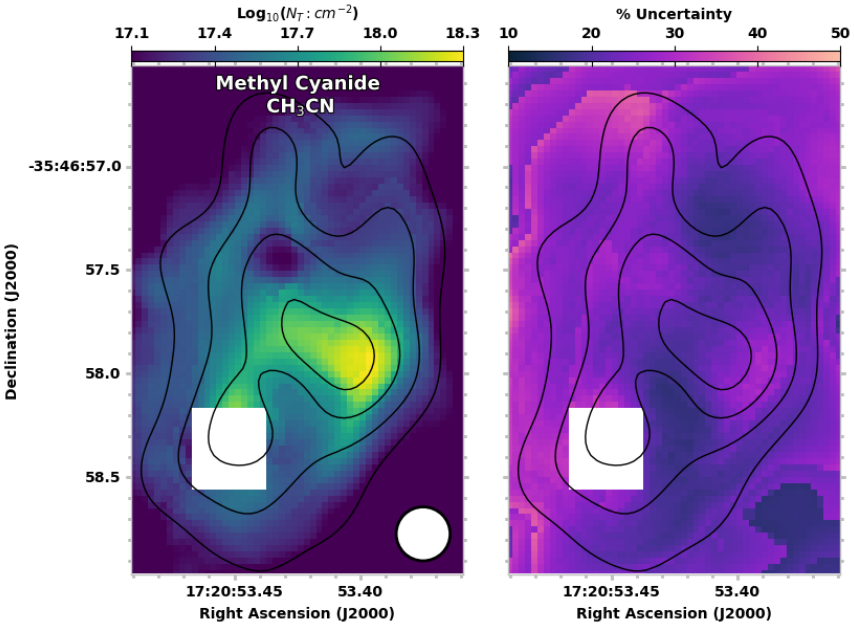


Fig. 6.27.— Same as Figure 6.25 but for methyl cyanide. See Section 3.3.3 for a description of some effects which may be impacting this image.

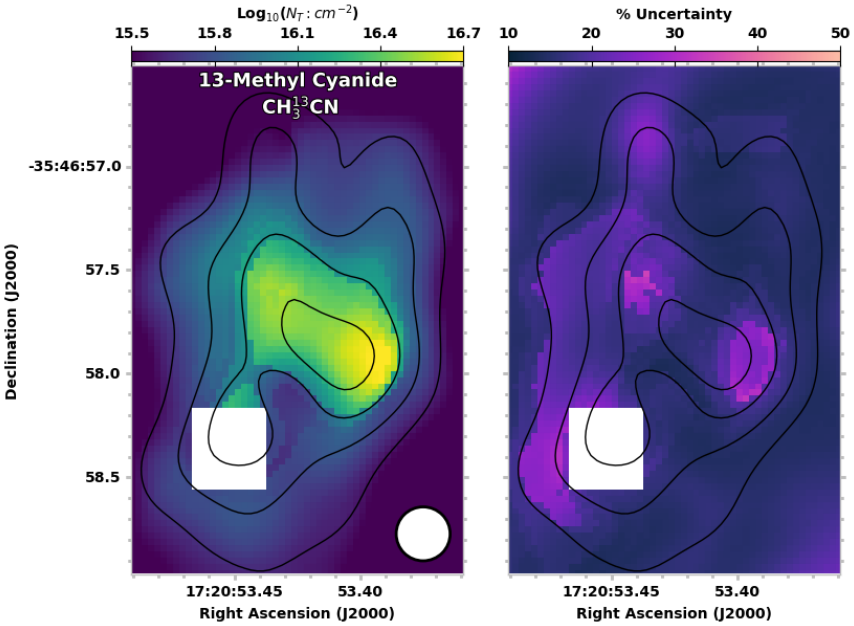


Fig. 6.28.— Same as Figure 6.25 but for 13-methyl cyanide.

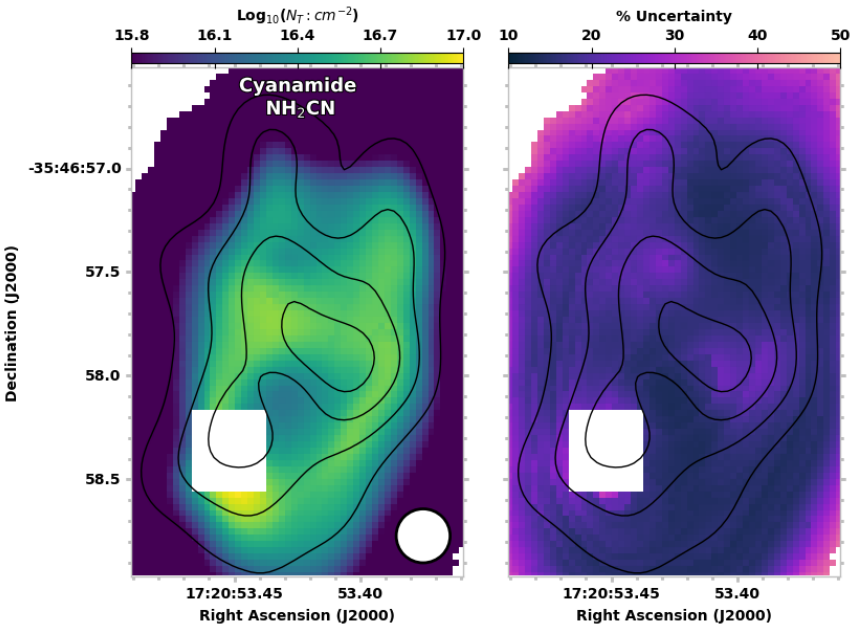


Fig. 6.29.— Same as Figure 6.25 but for cyanamide.

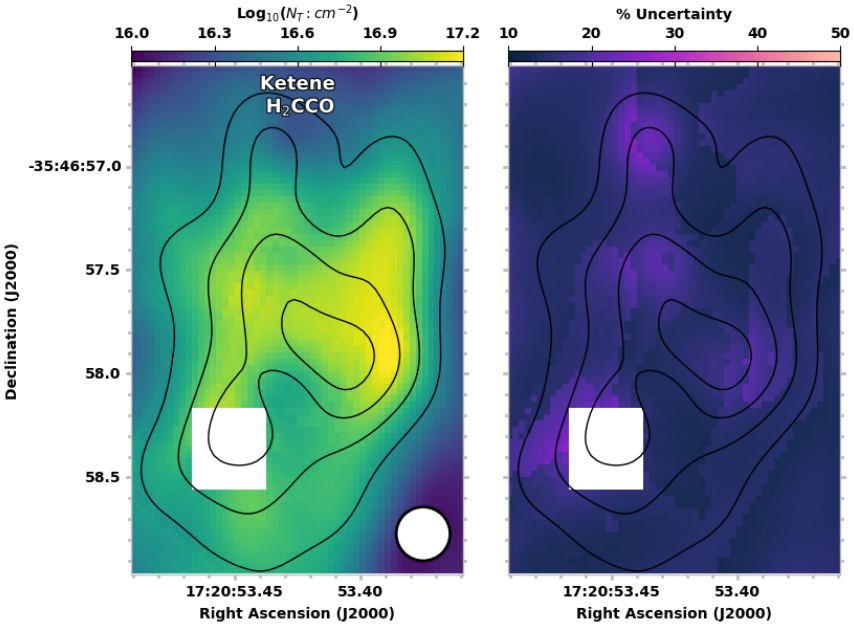


Fig. 6.30.— Same as Figure 6.25 but for ketene.

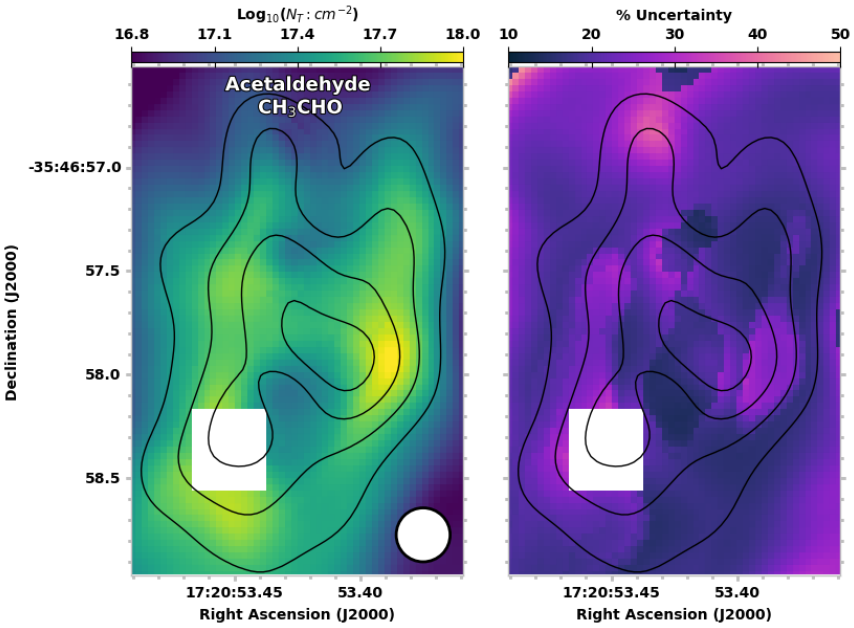


Fig. 6.31.— Same as Figure 6.25 but for acetaldehyde.

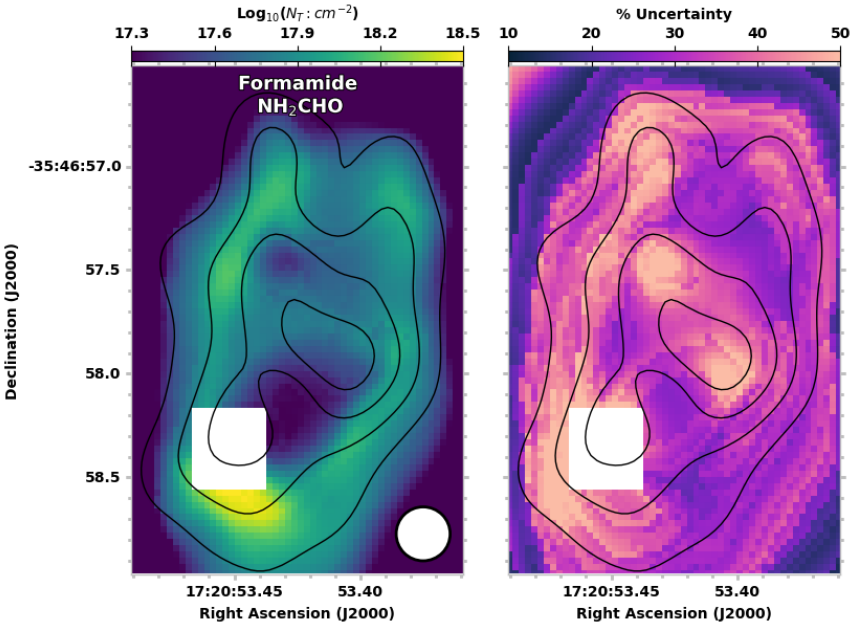


Fig. 6.32.— Same as Figure 6.25 but for formamide. See Section 3.3.3 for a description of some effects which may be impacting this image.

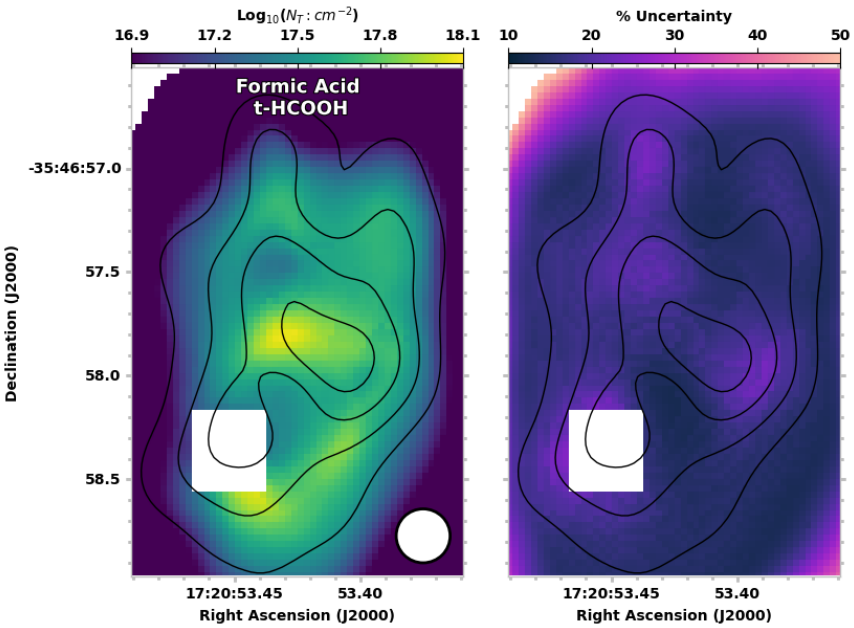


Fig. 6.33.— Same as Figure 6.25 but for the trans conformer formic acid.

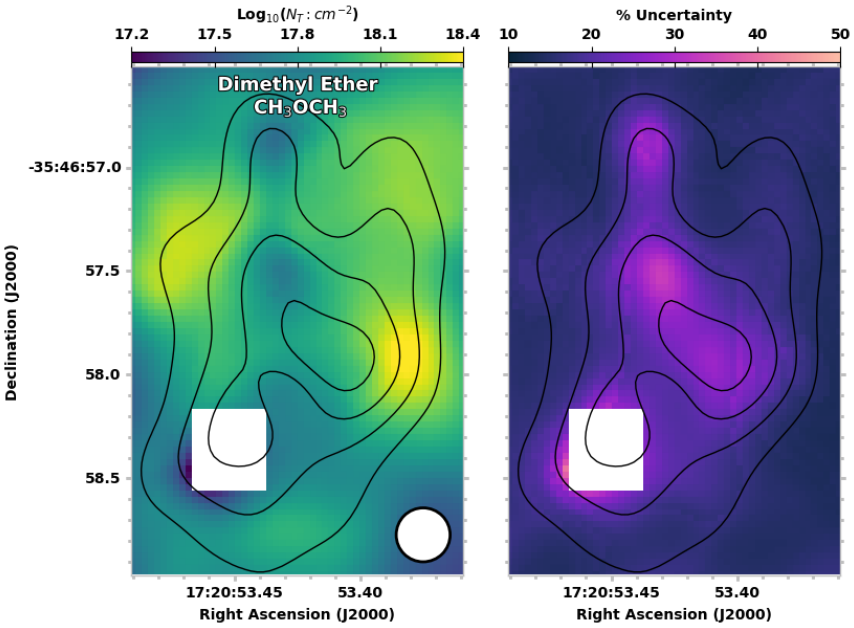


Fig. 6.34.— Same as Figure 6.25 but for dimethyl ether.

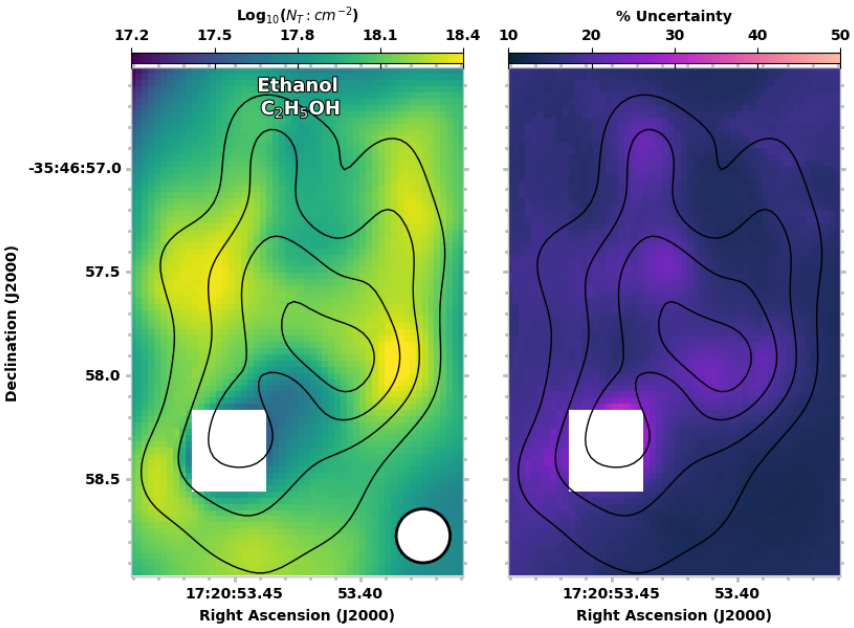


Fig. 6.35.— Same as Figure 6.25 but for ethanol.

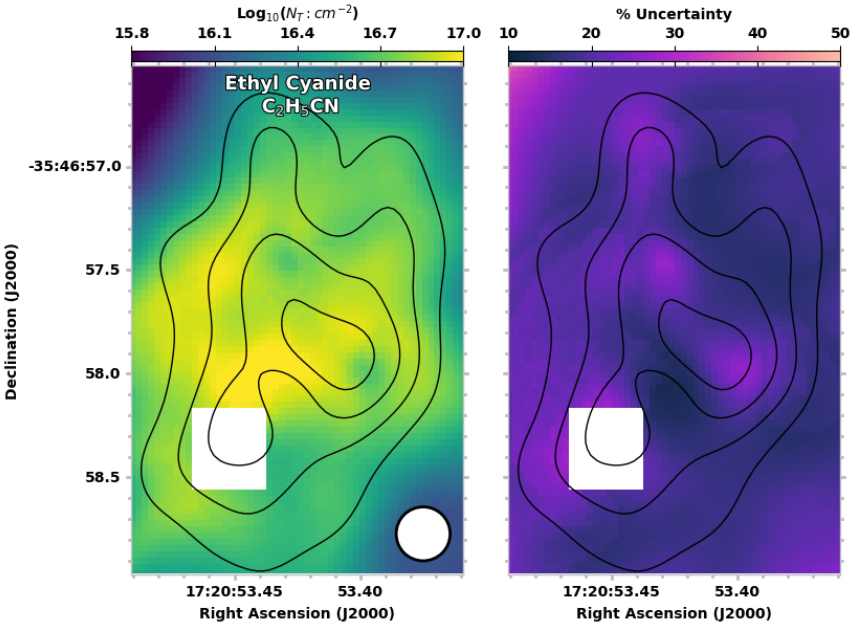


Fig. 6.36.— Same as Figure 6.25 but for ethyl cyanide.

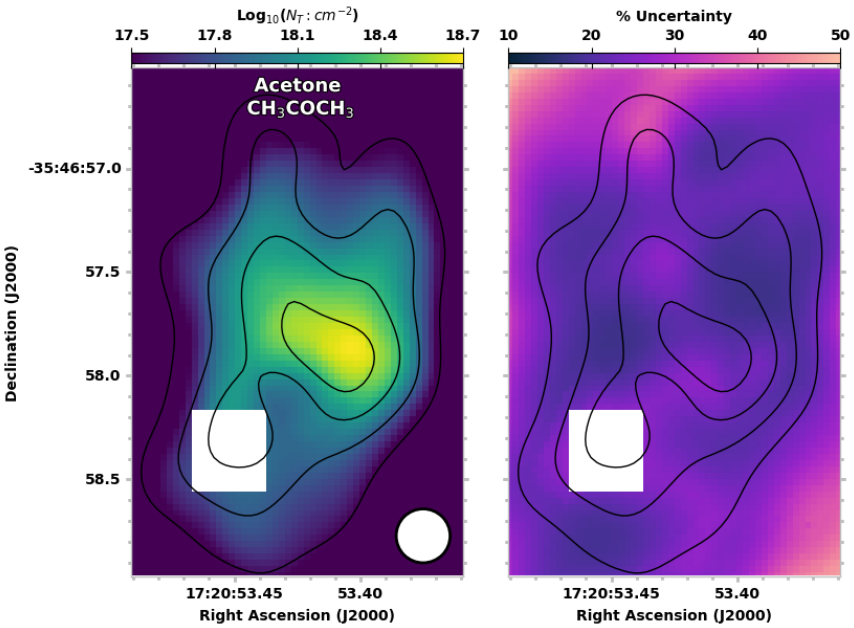


Fig. 6.37.— Same as Figure 6.25 but for acetone.

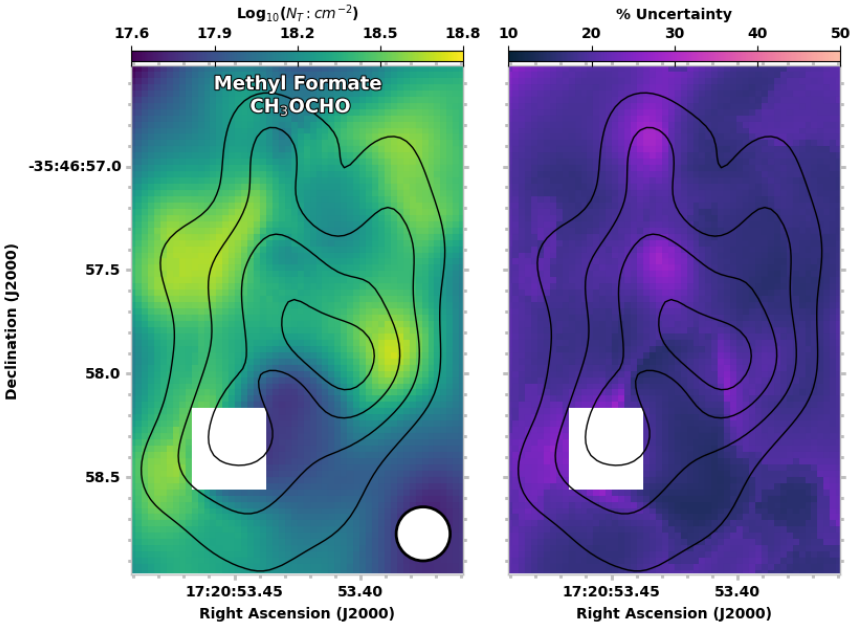


Fig. 6.38.— Same as Figure 6.25 but for methyl formate.

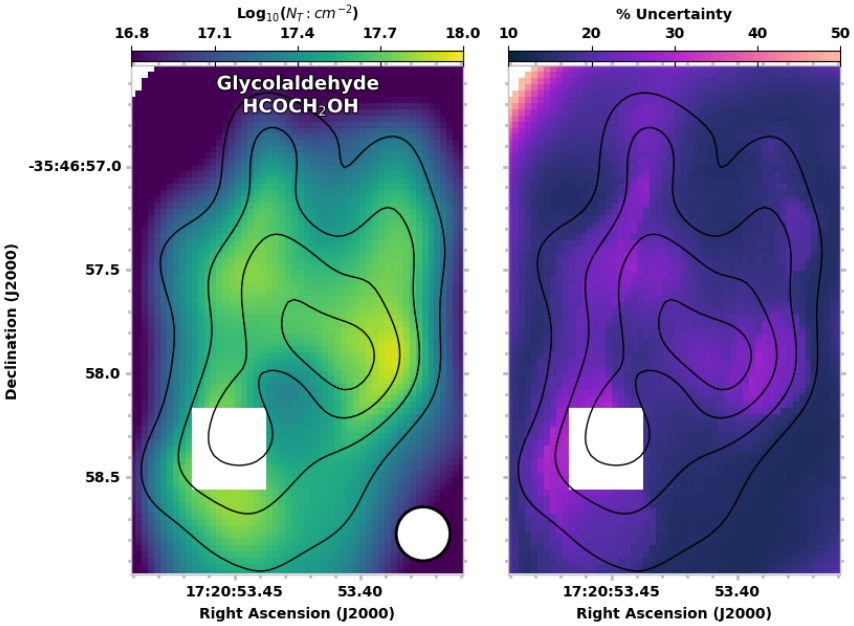


Fig. 6.39.— Same as Figure 6.25 but for glycolaldehyde.

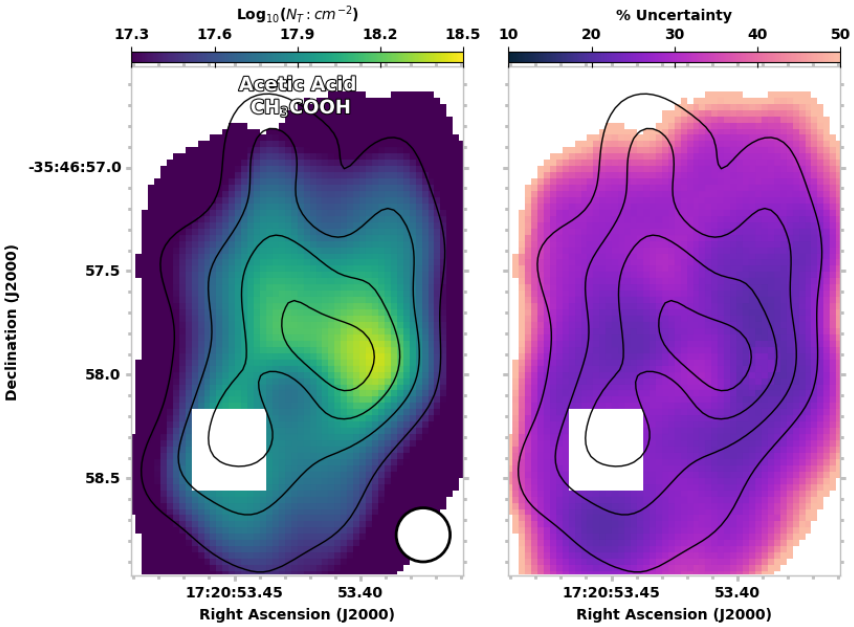


Fig. 6.40.— Same as Figure 6.25 but for acetic acid.

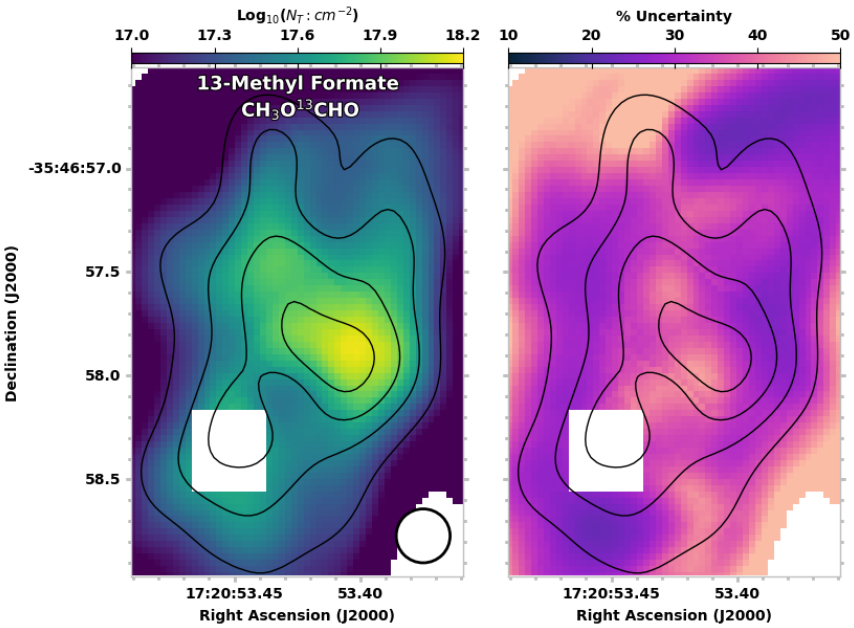


Fig. 6.41.— Same as Figure 6.25 but for 13-methyl formate.

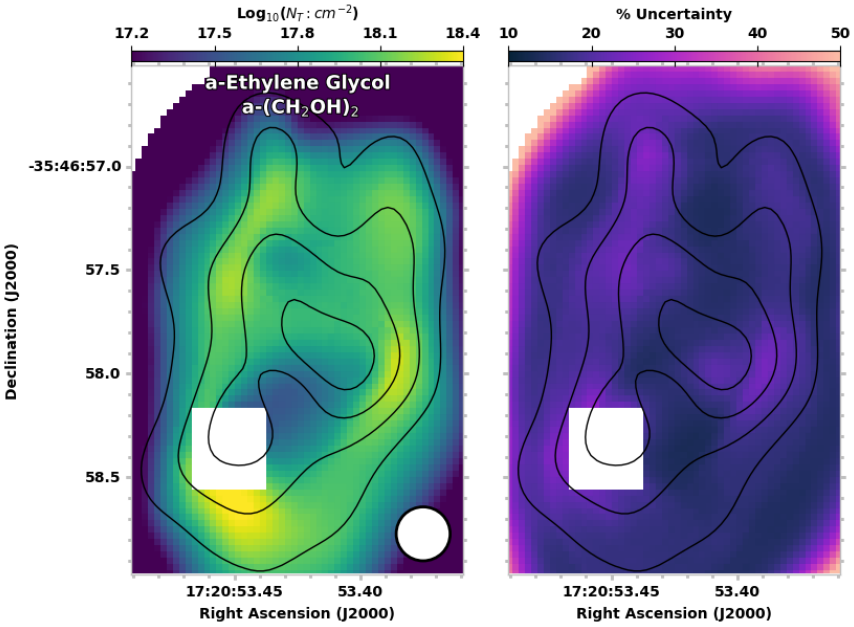


Fig. 6.42.— Same as Figure 6.25 but for a-ethylene glycol.

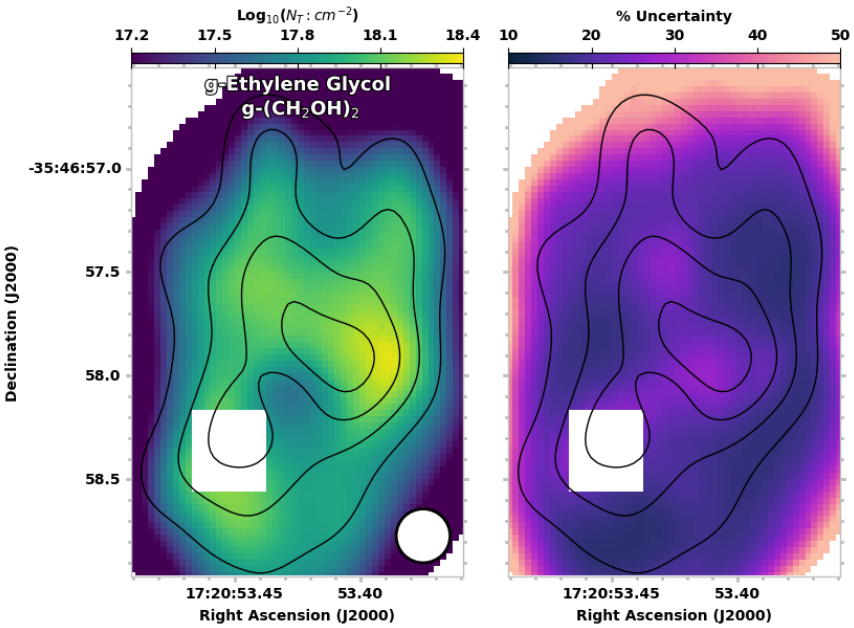


Fig. 6.43.— Same as Figure 6.25 but for g-ethylene glycol.

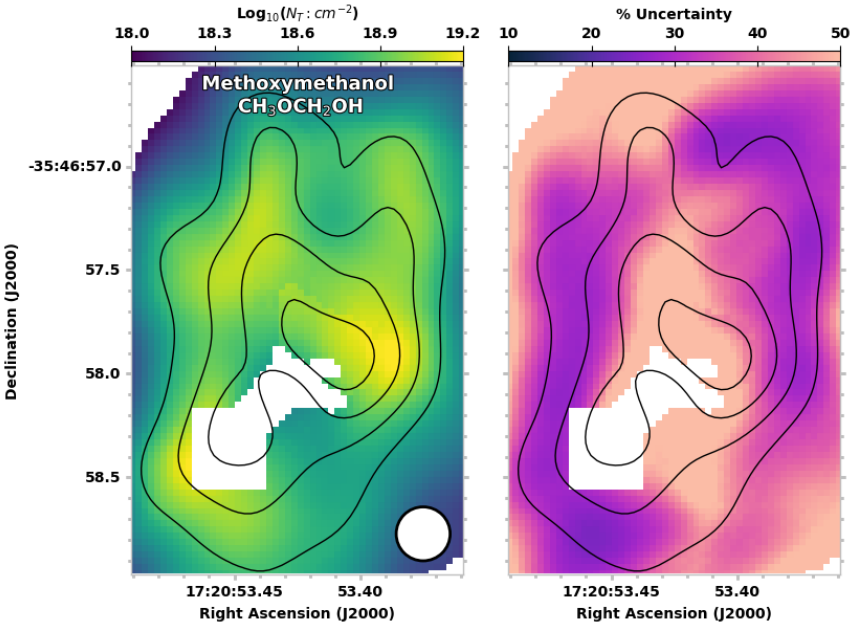


Fig. 6.44.— Same as Figure 6.25 but for methoxymethanol.

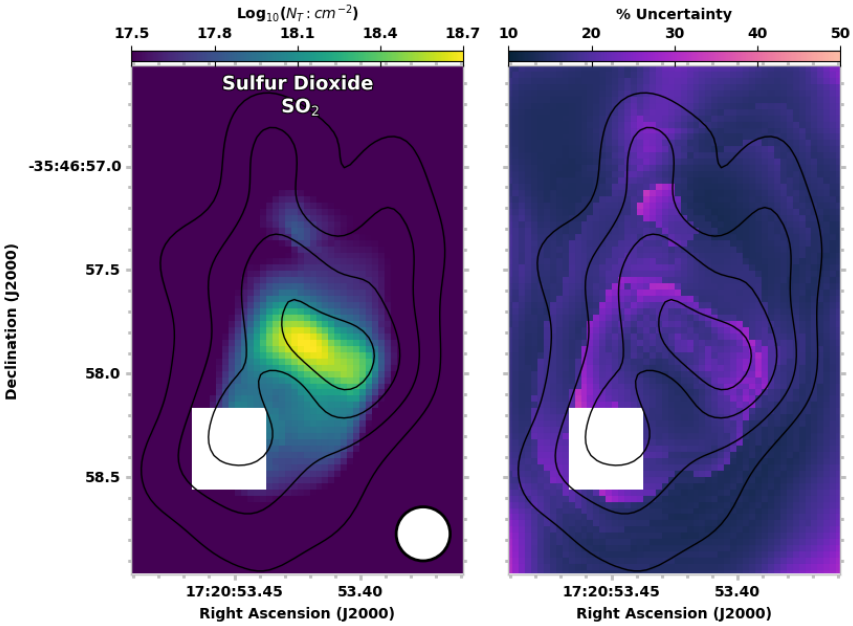


Fig. 6.45.— Same as Figure 6.25 but for sulfur dioxide.

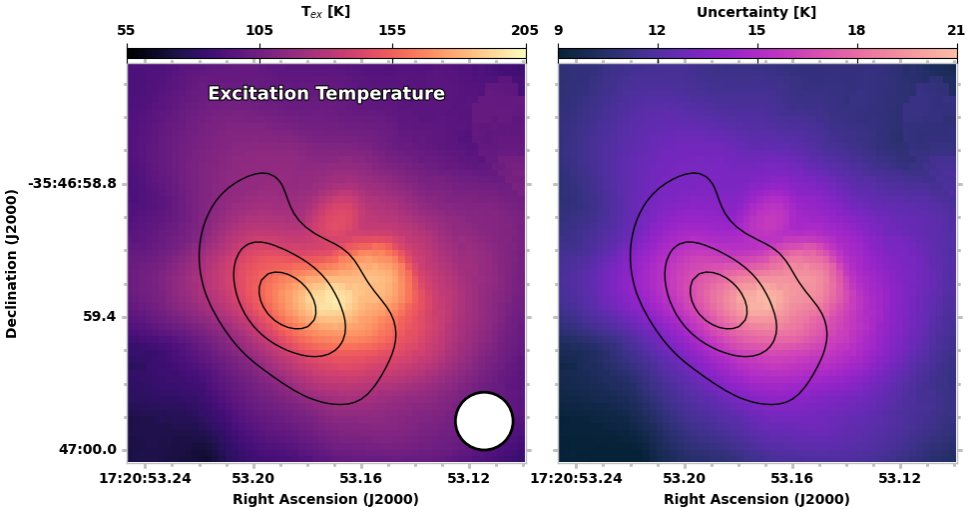


Fig. 6.46.— Excitation temperature (left) and excitation temperature uncertainty (right) images produced by the automated fitting routine for NGC 6334I-MM2.

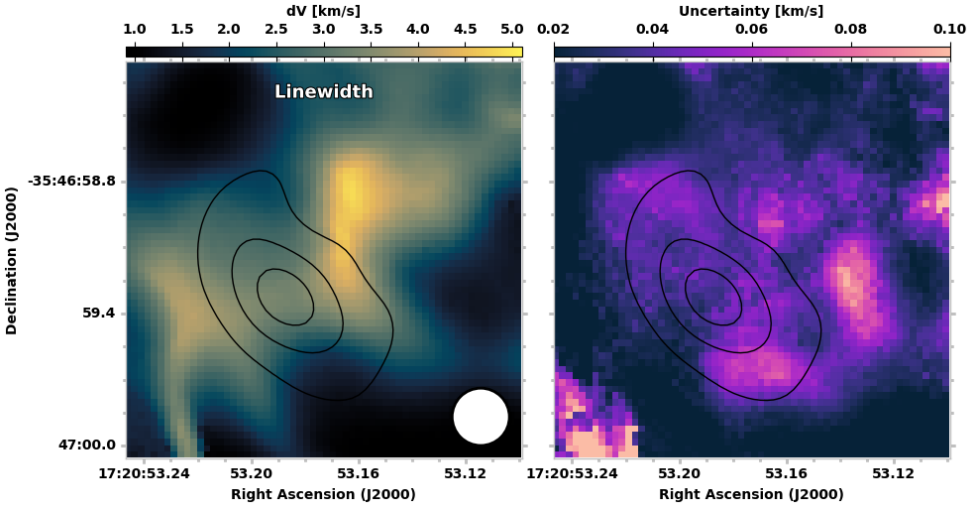


Fig. 6.47.— Linewidth (left) and linewidth uncertainty (right) images produced by the automated fitting routine for NGC 6334I-MM2.

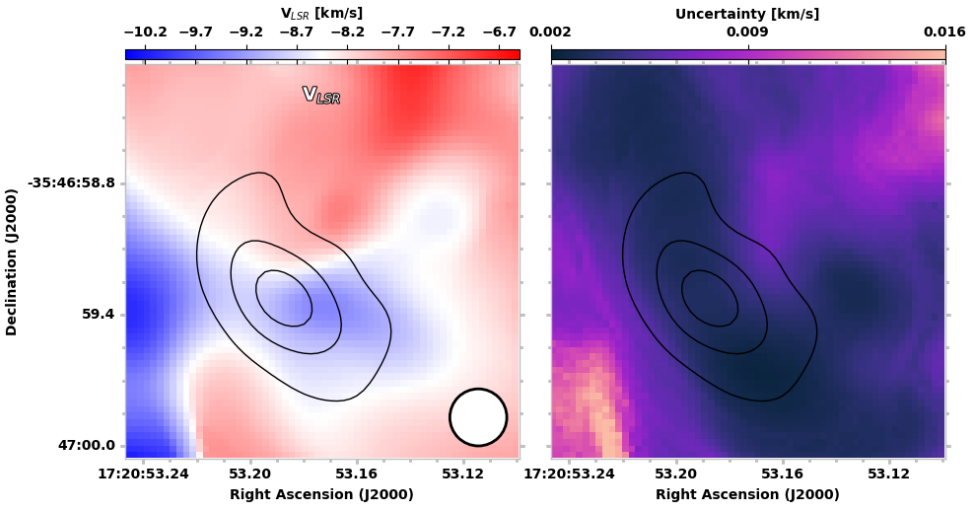


Fig. 6.48.— Velocity (left) and velocity uncertainty (right) images produced by the automated fitting routine for NGC 6334I-MM2.

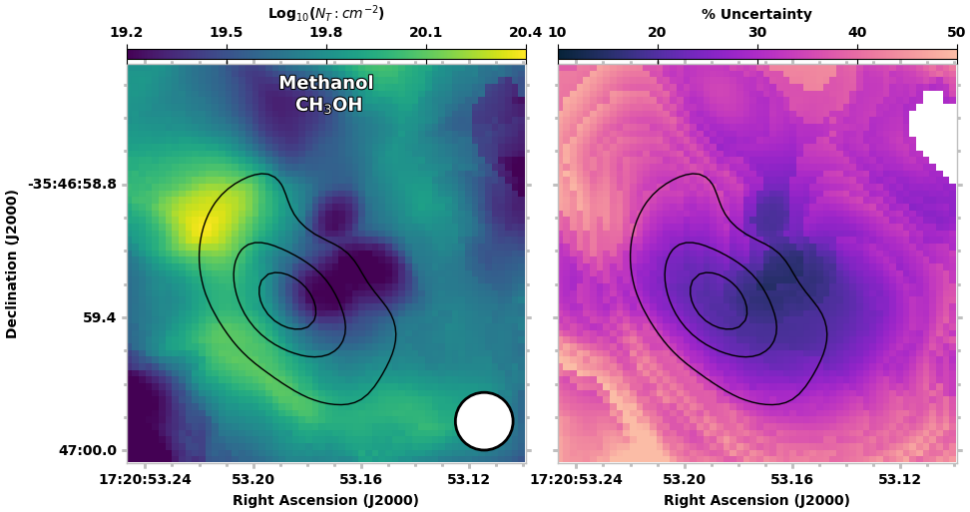


Fig. 6.49.— Column density (left) and column density uncertainty (right) images produced by the automated fitting routine for methanol in NGC 6334I-MM2.

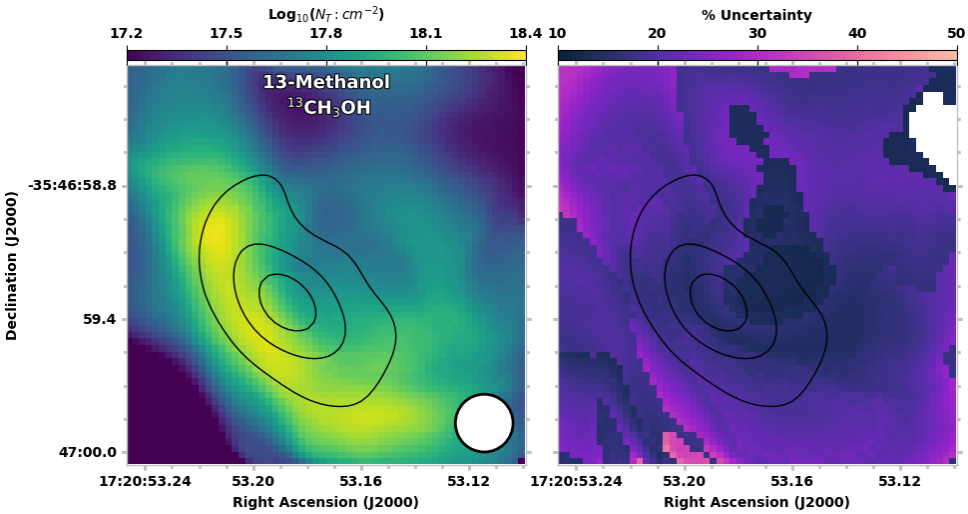


Fig. 6.50.— Same as Figure 6.49 but for 13-methanol.

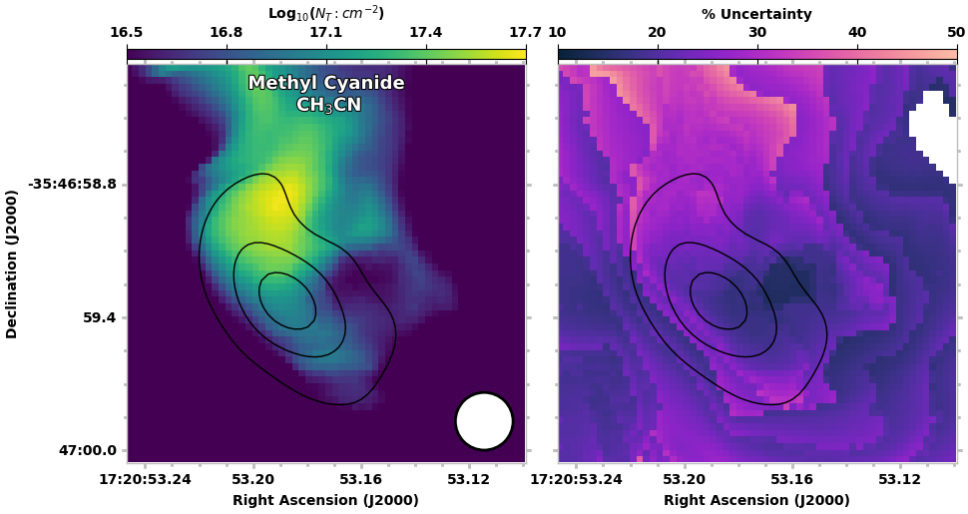


Fig. 6.51.— Same as Figure 6.49 but for methyl cyanide.

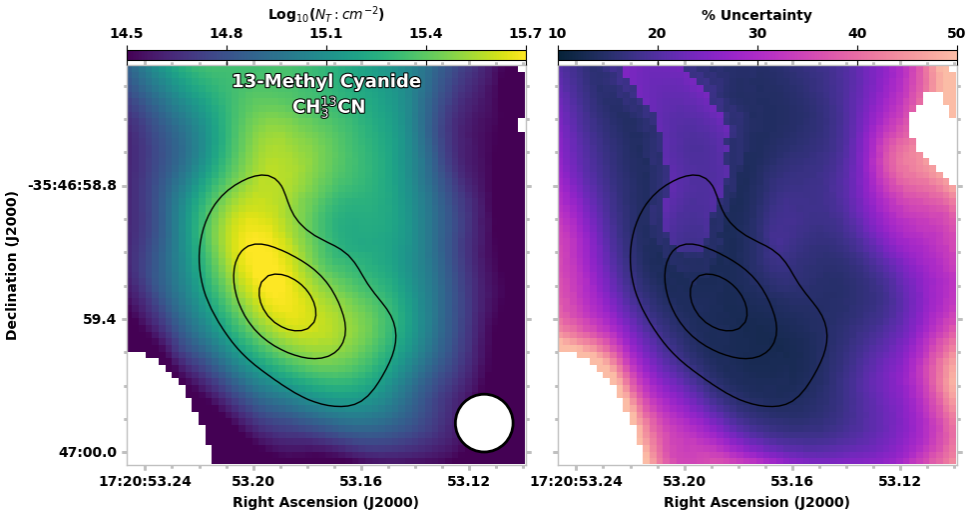


Fig. 6.52.— Same as Figure 6.49 but for 13-methyl cyanide.

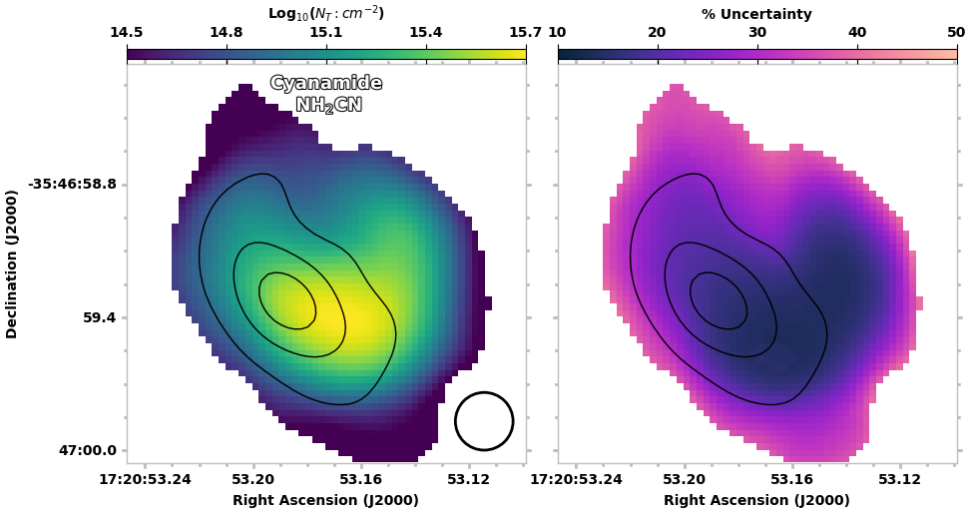


Fig. 6.53.— Same as Figure 6.49 but for cyanamide.

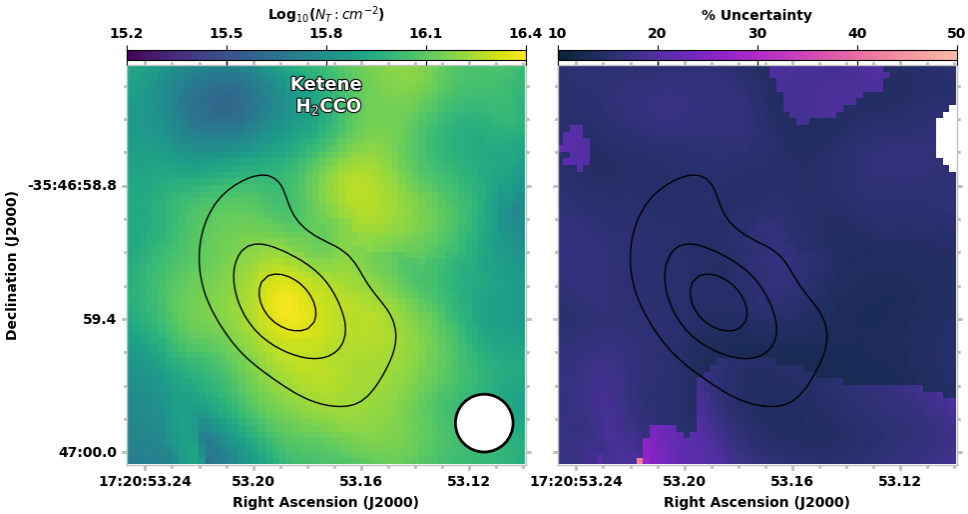


Fig. 6.54.— Same as Figure 6.49 but for ketene.

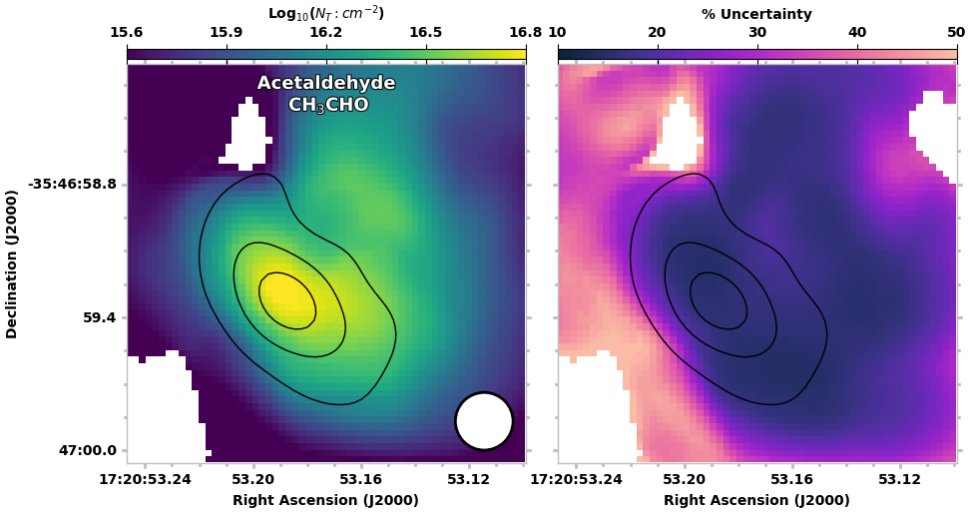


Fig. 6.55.— Same as Figure 6.49 but for acetaldehyde.

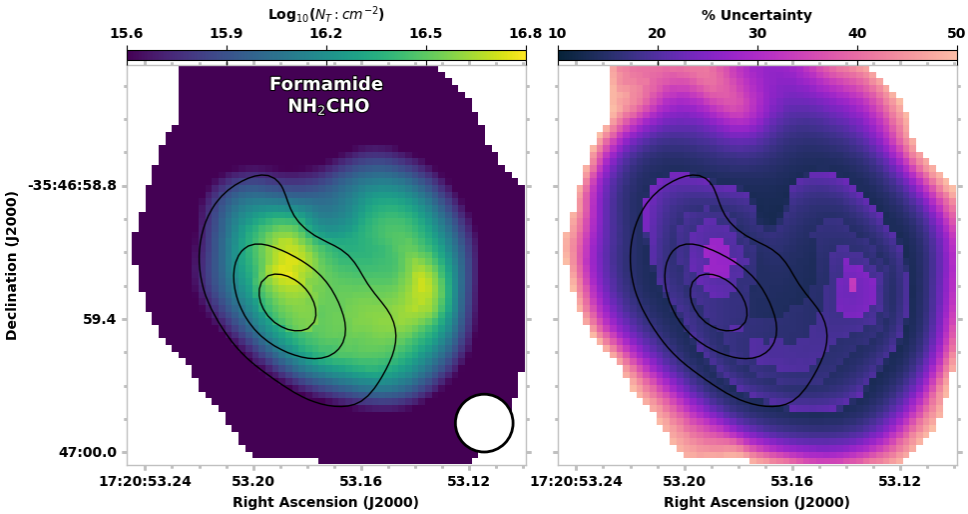


Fig. 6.56.— Same as Figure 6.49 but for formamide.

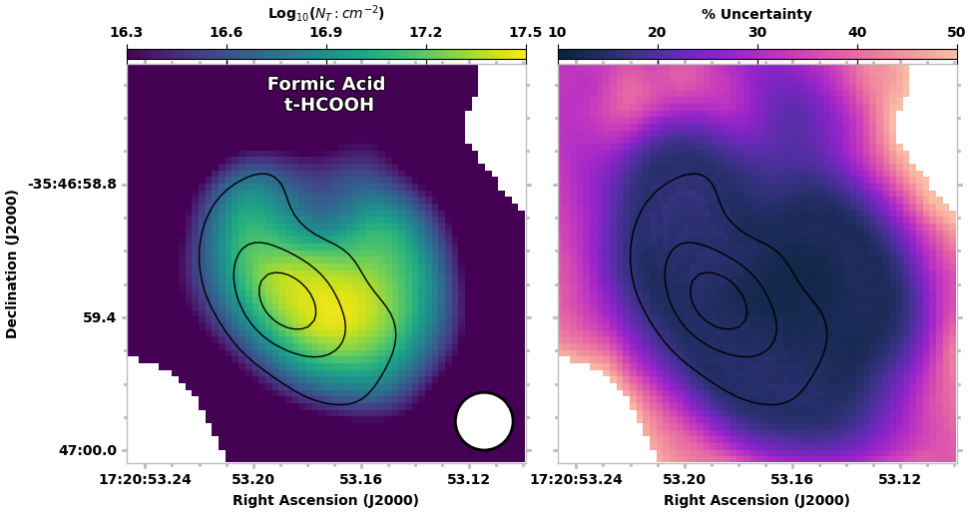


Fig. 6.57.— Same as Figure 6.49 but for the trans conformer of formic acid.

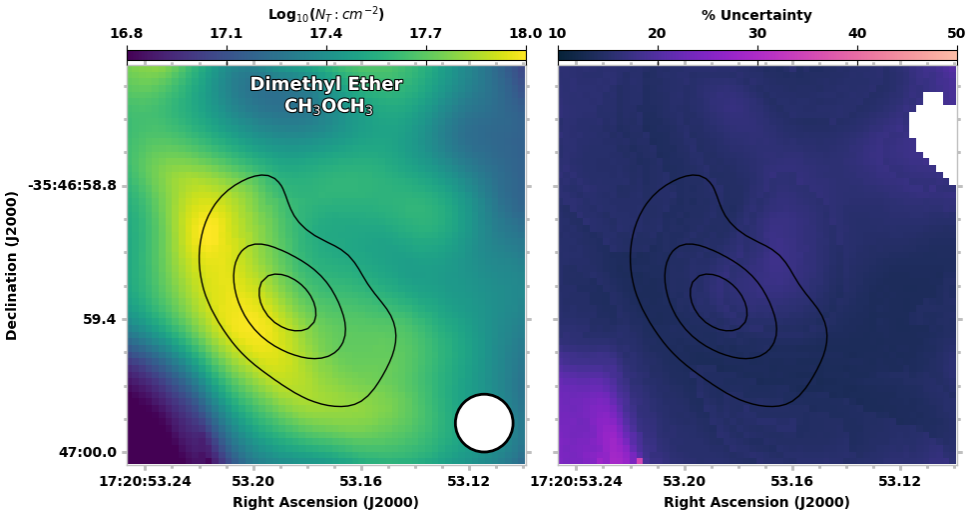


Fig. 6.58.— Same as Figure 6.49 but for dimethyl ether.

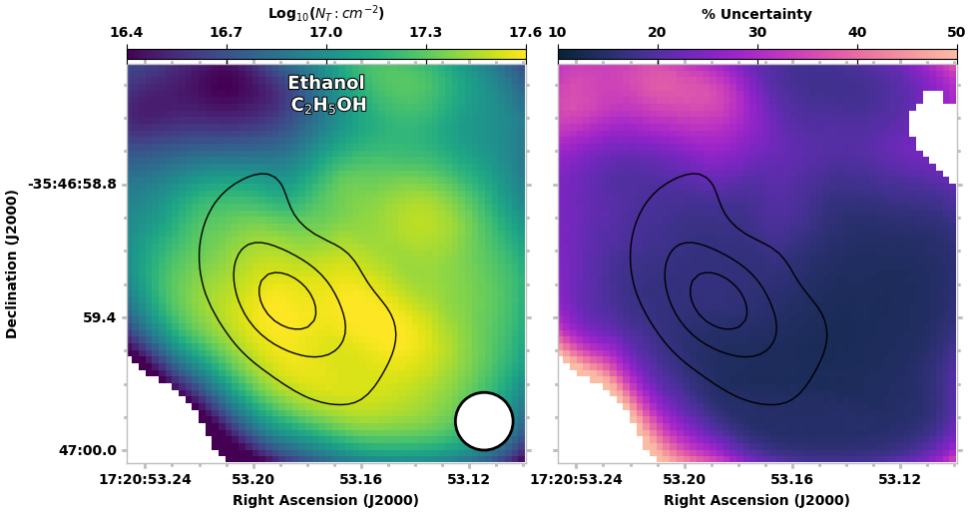


Fig. 6.59.— Same as Figure 6.49 but for ethanol.

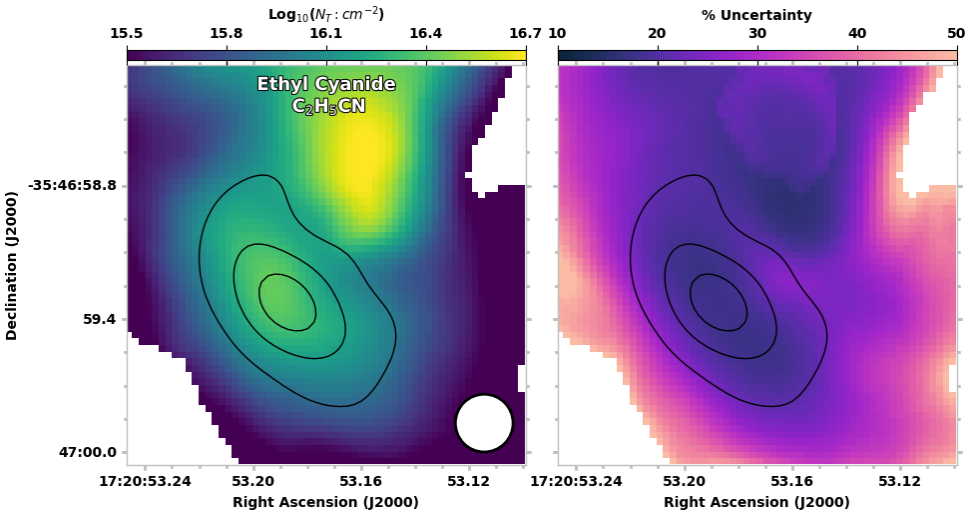


Fig. 6.60.— Same as Figure 6.49 but for ethyl cyanide.

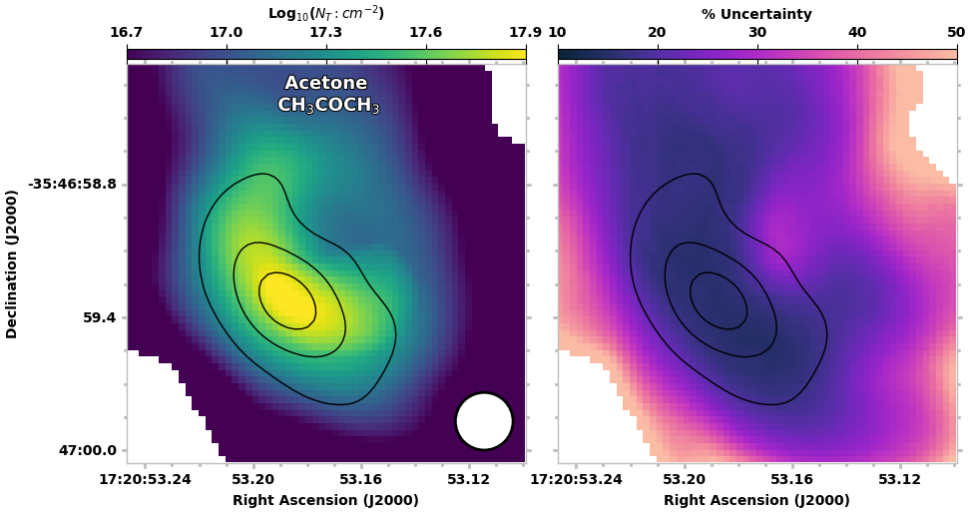


Fig. 6.61.— Same as Figure 6.49 but for acetone.

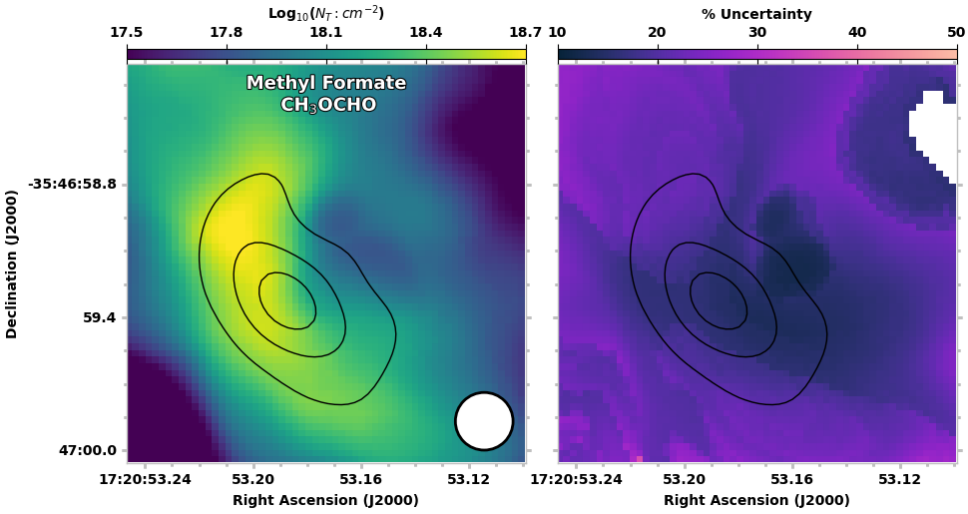


Fig. 6.62.— Same as Figure 6.49 but for methyl formate.

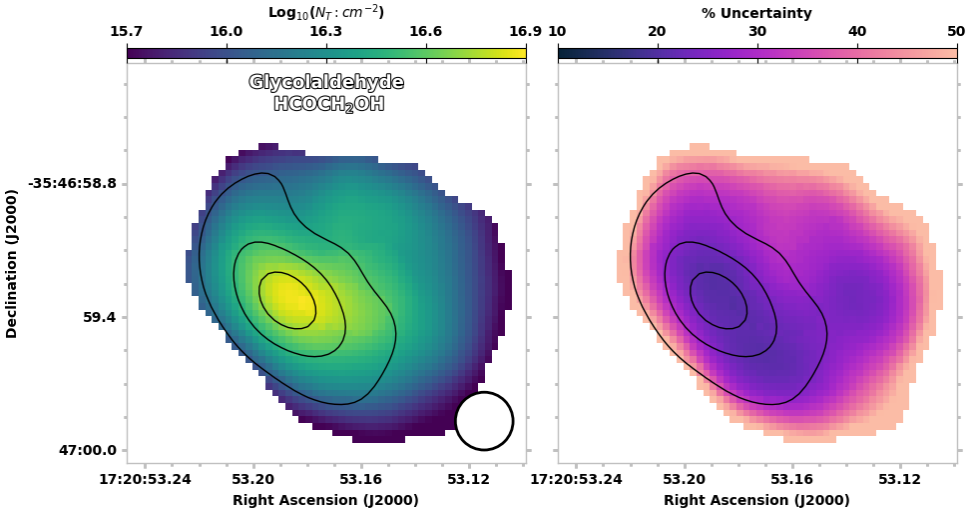


Fig. 6.63.— Same as Figure 6.49 but for glycolaldehyde. Due to the weak emission of this molecule in this source these values should be treated as an upper limit.

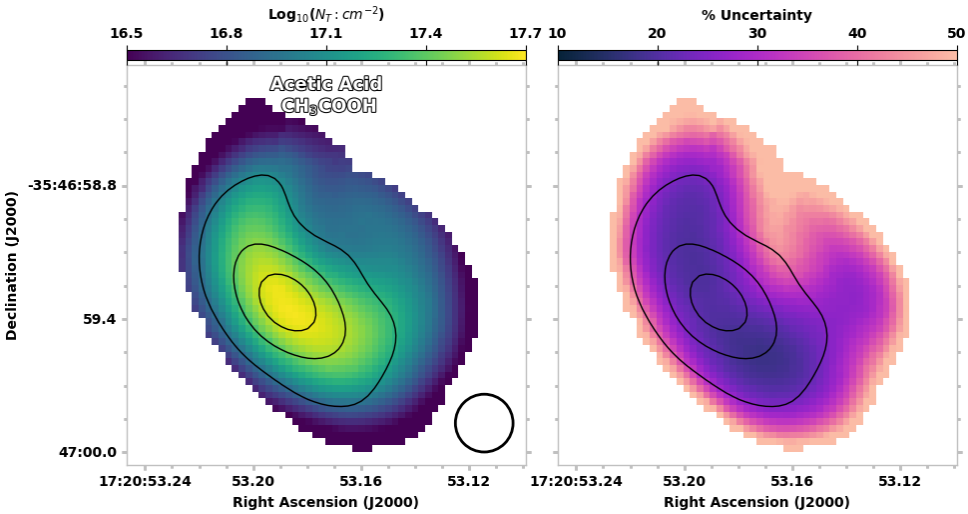


Fig. 6.64.— Same as Figure 6.49 but for acetic acid.

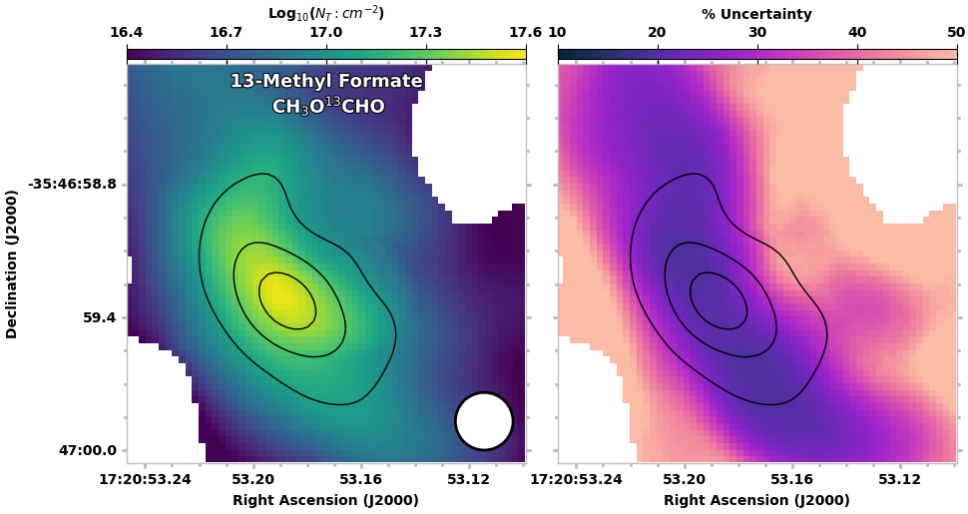


Fig. 6.65.— Same as Figure 6.49 but for 13-methyl formate.

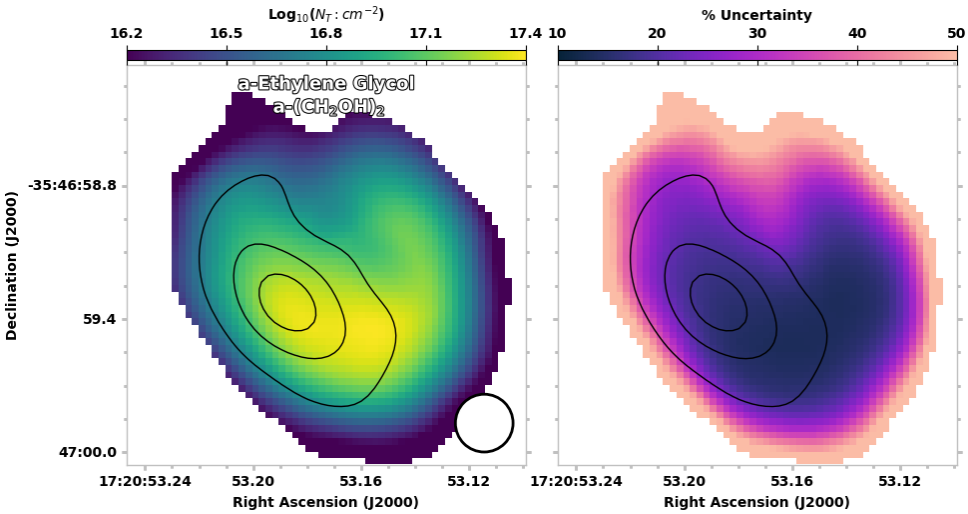


Fig. 6.66.— Same as Figure 6.49 but for a-ethylene glycol.

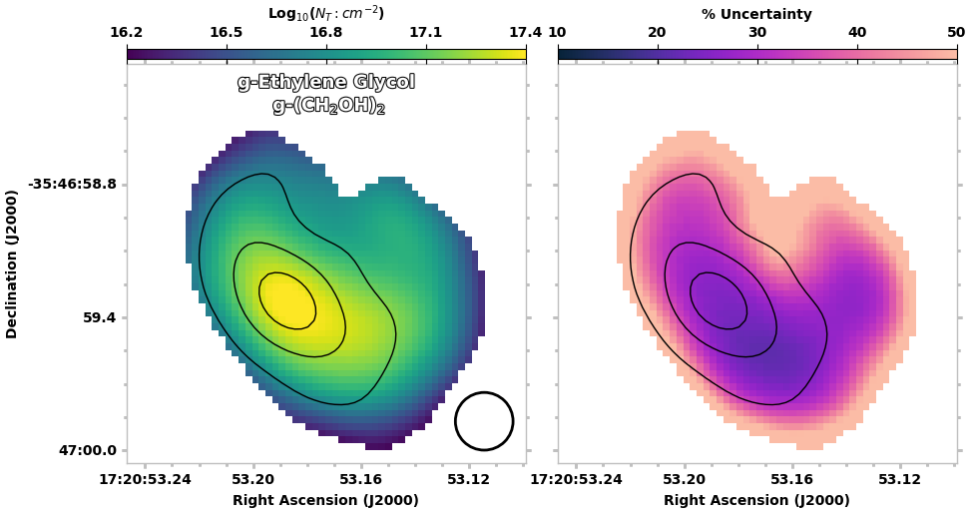


Fig. 6.67.— Same as Figure 6.49 but for g-ethylene glycol.

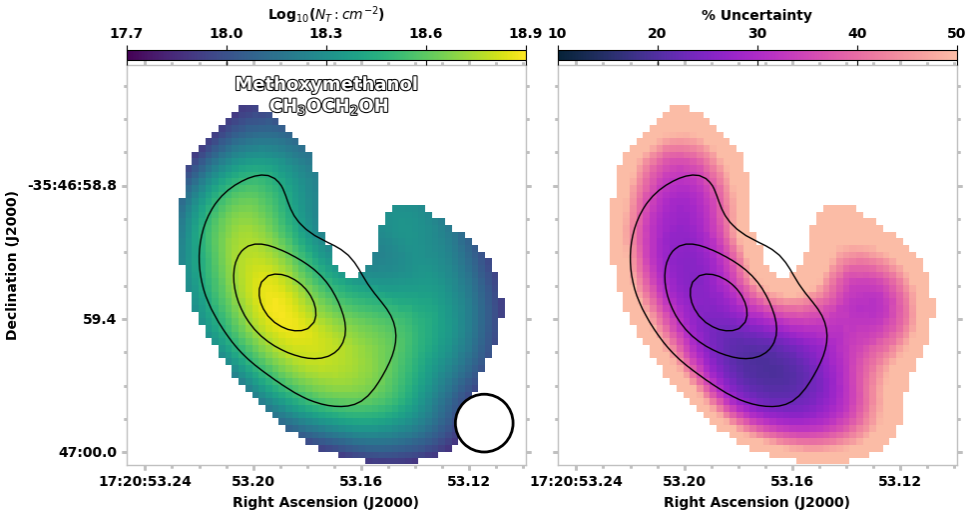


Fig. 6.68.— Same as Figure 6.49 but for methoxymethanol.

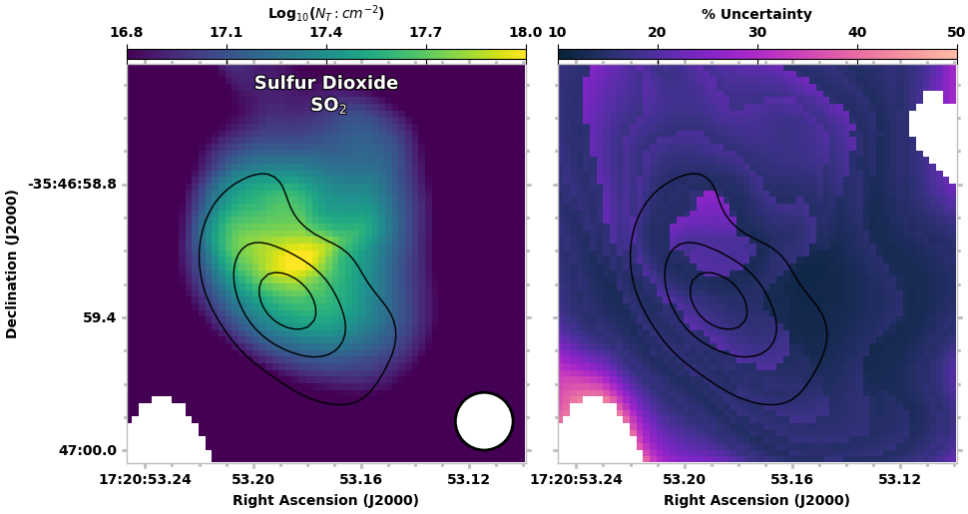


Fig. 6.69.— Same as Figure 6.49 but for sulfur dioxide.

# A3 Appendix C - Miscellaneous Data

We present two spectra extracted from the northernmost “filament" in the linewidth map of Figure 3.6 to showcase the measurable difference in the lineshapes in Figure 6.70. We also present a pair of spectra demonstrating how the variation in spectral crowding across the source can impact the measured velocity using the moment map technique.

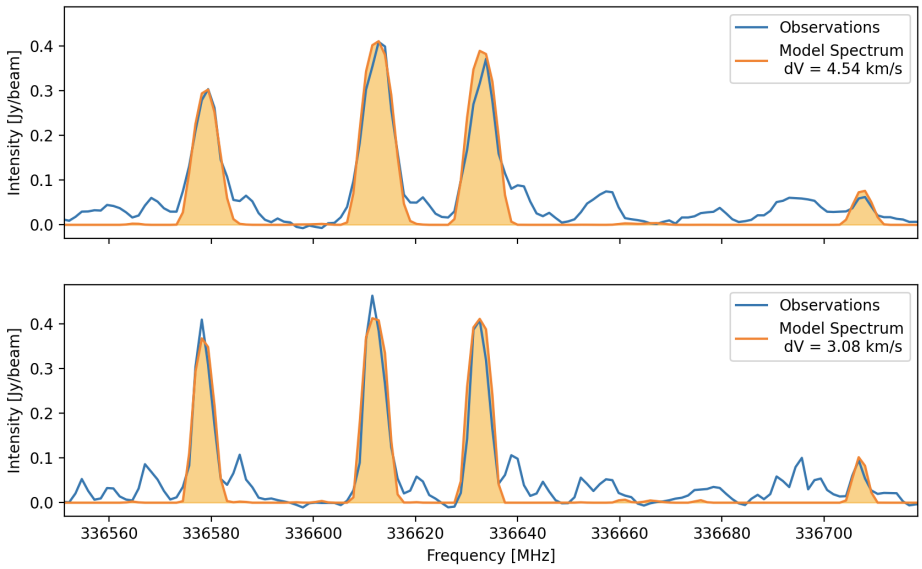


Fig. 6.70.— A pair of spectra extracted from the northernmost “filament" in the linewidth map of Figure 3.6. The two spectra were extracted from pixels that were in the center *(top)* and edge *(bottom)* of the feature.

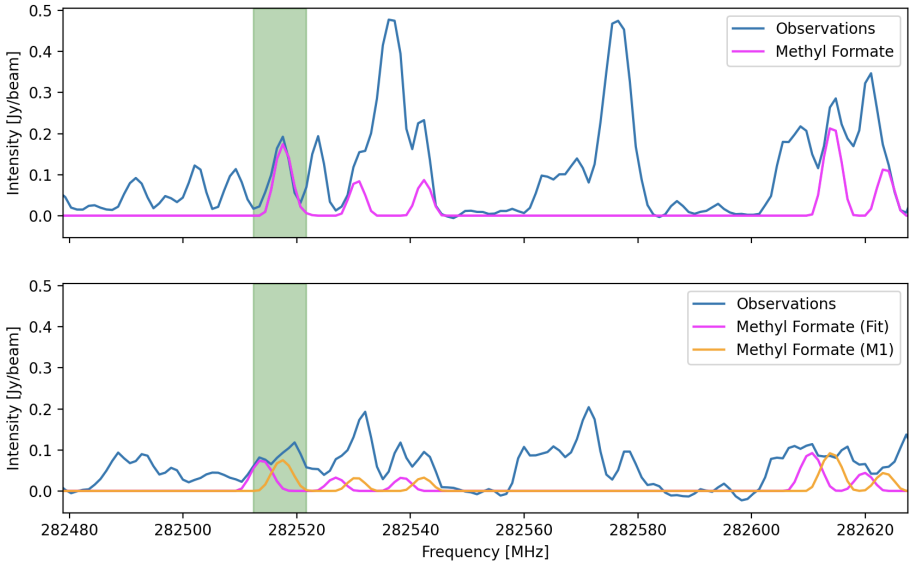


Fig. 6.71.— The top spectrum is from one of the pixels that was used in El-Abd et al. (2019) to measure the properties of methyl formate in MM1 with the channels used for the moment 1 map highlighted in green. The bottom spectrum is from a pixel where our method of measuring the velocity disagreed with the moment map by almost 4 km $s^{-1}$ with a simulated spectrum at both velocities overlaid. Note how the moment 1 map understandably skews toward the stronger transition in the channel range while our method (correctly) picks out the weaker transition. This speaks to both the difficulty in picking out an appropriate channel range for the entirety of a turbulent region for a moment 1 map as well as the strength of our method as the velocity is not skewed by an individual transition for a molecule.

# References

Andre, P., Ward-Thompson, D., & Barsony, M. 1999, publisher: [object Object] Version Number: 1

Astropy Collaboration, Price-Whelan, A. M., Lim, P. L., Earl, N., Starkman, N., Bradley, L., Shupe, D. L., Patil, A. A., Corrales, L., Brasseur, C. E., Nöthe, M., Donath, A., Tollerud, E., Morris, B. M., Ginsburg, A., Vaher, E., Weaver, B. A., Tocknell, J., Jamieson, W., van Kerkwijk, M. H., Robitaille, T. P., Merry, B., Bachetti, M., Günther, H. M., Aldcroft, T. L., Alvarado-Montes, J. A., Archibald, A. M., Bódi, A., Bapat, S., Barentsen, G., Bazán, J., Biswas, M., Boquien, M., Burke, D. J., Cara, D., Cara, M., Conroy, K. E., Conseil, S., Craig, M. W., Cross, R. M., Cruz, K. L., D'Eugenio, F., Dencheva, N., Devillepoix, H. A. R., Dietrich, J. P., Eigenbrot, A. D., Erben, T., Ferreira, L., Foreman-Mackey, D., Fox, R., Freij, N., Garg, S., Geda, R., Glattly, L., Gondhalekar, Y., Gordon, K. D., Grant, D., Greenfield, P., Groener, A. M., Guest, S., Gurovich, S., Handberg, R., Hart, A., Hatfield-Dodds, Z., Homeier, D., Hosseinzadeh, G., Jenness, T., Jones, C. K., Joseph, P., Kalmbach, J. B., Karamehmetoglu, E., Kałuszyński, M., Kelley, M. S. P., Kern, N., Kerzendorf, W. E., Koch, E. W., Kulumani, S., Lee, A., Ly, C., Ma, Z., MacBride, C., Maljaars, J. M., Muna, D., Murphy, N. A., Norman, H., O'Steen, R., Oman, K. A., Pacifici, C., Pascual, S., Pascual-Granado, J., Patil,

R. R., Perren, G. I., Pickering, T. E., Rastogi, T., Roulston, B. R., Ryan, D. F., Rykoff, E. S., Sabater, J., Sakurikar, P., Salgado, J., Sanghi, A., Saunders, N., Savchenko, V., Schwardt, L., Seifert-Eckert, M., Shih, A. Y., Jain, A. S., Shukla, G., Sick, J., Simpson, C., Singanamalla, S., Singer, L. P., Singhal, J., Sinha, M., Sipőcz, B. M., Spitler, L. R., Stansby, D., Streicher, O., Šumak, J., Swinbank, J. D., Taranu, D. S., Tewary, N., Tremblay, G. R., de Val-Borro, M., Van Kooten, S. J., Vasović, Z., Verma, S., de Miranda Cardoso, J. V., Williams, P. K. G., Wilson, T. J., Winkel, B., Wood-Vasey, W. M., Xue, R., Yoachim, P., Zhang, C., Zonca, A., & Astropy Project Contributors. 2022, The Astrophysical Journal, 935, 167, aDS Bibcode: 2022ApJ...935..167A

Astropy Collaboration, Robitaille, T. P., Tollerud, E. J., Greenfield, P., Droettboom, M., Bray, E., Aldcroft, T., Davis, M., Ginsburg, A., Price-Whelan, A. M., Kerzendorf, W. E., Conley, A., Crighton, N., Barbary, K., Muna, D., Ferguson, H., Grollier, F., Parikh, M. M., Nair, P. H., Unther, H. M., Deil, C., Woillez, J., Conseil, S., Kramer, R., Turner, J. E. H., Singer, L., Fox, R., Weaver, B. A., Zabalza, V., Edwards, Z. I., Azalee Bostroem, K., Burke, D. J., Casey, A. R., Crawford, S. M., Dencheva, N., Ely, J., Jenness, T., Labrie, K., Lim, P. L., Pierfederici, F., Pontzen, A., Ptak, A., Refsdal, B., Servillat, M., & Streicher, O. 2013, The Astrophysical Journal Letters, 558, A33

Balucani, N., Ceccarelli, C., & Taquet, V. 2015, Monthly Notices of the Royal Astronomical Society: Letters, 449, L16

Belloche, A., Müller, H. S. P., Menten, K. M., Schilke, P., & Comito, C. 2013, Astronomy & Astrophysics, 559, A47

Beuther, H., Churchwell, E. B., McKee, C. F., & Tan, J. C. 2006, publisher: [object Object] Version Number: 2

Beuther, H., Walsh, A. J., Thorwirth, S., Zhang, Q., Hunter, T. R., Megeath, S. T., & Menten, K. M. 2007, Astronomy & Astrophysics, 466, 989, arXiv:astro-ph/0702190

Bonnell, I. A. & Bate, M. R. 2006, Monthly Notices of the Royal Astronomical Society, 370, 488

Brogan, C. L., Chandler, C. J., Hunter, T. R., Shirley, Y. L., & Sarma, A. P. 2007, The Astrophysical Journal, 660, L133

Brogan, C. L., Hunter, T. R., Cyganowski, C. J., Chandler, C. J., Friesen, R., & Indebetouw, R. 2016, The Astrophysical Journal Letters, 832, 1

Brogan, C. L., Hunter, T. R., Cyganowski, C. J., Chibueze, J. O., Friesen, R. K., Hirota, T., MacLeod, G. C., McGuire, B. A., & Sobolev, A. M. 2018, The Astrophysical Journal, 866, 87, arXiv:1809.04178 [astro-ph]

Brogan, C. L., Hunter, T. R., Towner, A. P. M., McGuire, B. A., MacLeod, G. C., Gurwell, M. A., Cyganowski, C. J., Brand, J., Burns, R. A., O Garatti, A. C., Chen, X., Chibueze, J. O., Hirano, N., Hirota, T., Kim, K.-T., Kramer, B. H., Linz, H., Menten, K. M., Remijan, A., Sanna, A., Sobolev, A. M., Sridharan, T. K., Stecklum, B., Sugiyama, K., Surcis, G., Van Der Walt, J., Volvach, A. E., & Volvach, L. N. 2019, The Astrophysical Journal Letters, 881, L39

Brouillet, N., Despois, D., Baudry, A., Peng, T. C., Favre, C., Wootten, A., Remijan, A. J., L., W. T., Combes, F., & Wlodarczak, G. 2013, antike und abendland, 550, A46

Bøgelund, E. G., McGuire, B. A., Ligterink, N. F. W., Taquet, V., Brogan, C. L., Hunter, T. R., Pearson, J. C., Hogerheijde, M. R., & van Dishoeck, E. F. 2018, Astronomy & Astrophysics, 615, A88, arXiv:1804.01090 [astro-ph]

Calcutt, H., Jørgensen, J. K., Müller, H. S. P., Kristensen, L. E., Coutens, A., Bourke, T. L., Garrod, R. T., Persson, M. V., van der Wiel, M. H. D., van Dishoeck, E. F., & Wampfler, S. F. 2018, Astronomy & Astrophysics, 616, A90, arXiv:1804.09210 [astro-ph]

Calcutt, H., Viti, S., Codella, C., Beltrán, M. T., Fontani, F., & Woods, P. M. 2014, Monthly Notices of the Royal Astronomical Society, 443, 3157

Campbell, S. 2018, Comparison of the generalized centroid with Gaussian and quadratic peak localization methods, arXiv:1807.08355 [astro-ph]

Caratti O Garatti, A., Stecklum, B., Garcia Lopez, R., Eislöffel, J., Ray, T. P., Sanna, A., Cesaroni, R., Walmsley, C., Oudmaijer, R. D., De Wit, W. J., Moscadelli, L., Greiner, J., Krabbe, A., Fischer, C., Klein, R., & Ibañez, J. M. 2017, Nature Physics, 13, 276

Carroll, P. B., Drouin, B. J., & Widicus Weaver, S. L. 2010, The Astrophysical Journal, 723, 845

Cazaux, S. & Tielens, A. G. G. M. 2004, The Astrophysical Journal, 604, 222

Chen, Y., Van Gelder, M. L., Nazari, P., Brogan, C. L., Van Dishoeck, E. F., Linnartz, H., Jørgensen, J. K., Hunter, T. R., Wilkins, O. H., Blake, G. A., Caselli, P., Chuang, K.-J., Codella, C., Cooke, I., Drozdovskaya, M. N., Garrod, R. T., Ioppolo, S., Jin, M., Kulterer, B. M., Ligterink, N. F. W., Lipnicky, A., Loomis, R., Rachid,

M. G., Spezzano, S., & McGuire, B. A. 2023, Astronomy & Astrophysics, 678, A137

Chibueze, J. O., Omodaka, T., Handa, T., Imai, H., Kurayama, T., Nagayama, T., Sunada, K., Nakano, M., Hirota, T., & Honma, M. 2014, The Astrophysical Journal, 784, 114

Chini, R., Barr, A., Buda, L. S., Dembsky, T., Drass, H., Nasseri, A., Hoffmeister, V. H., & Fuhrmann, K. 2013, publisher: [object Object] Version Number: 1

Cortes, P., Vlahakis, C., Hales, A., Carpenter, J., Dent, B., Kameno, S., Loomis, R., Vila Vilaro, B., Biggs, A., Miotello, A., Rosen, R., Stoehr, F., & Saini, K. 2023, publisher: Zenodo Version Number: Cycle 10; Doc. 10.3; version 1.1

Cunningham, N., Ginsburg, A., Galván-Madrid, R., Motte, F., Csengeri, T., Stutz, A. M., Fernández-López, M., Álvarez Gutiérrez, R. H., Armante, M., Baug, T., Bonfand, M., Bontemps, S., Braine, J., Brouillet, N., Busquet, G., Díaz-González, D. J., Di Francesco, J., Gusdorf, A., Herpin, F., Liu, H., López-Sepulcre, A., Louvet, F., Lu, X., Maud, L., Nony, T., Olguin, F. A., Pouteau, Y., Rivera-Soto, R., Sandoval-Garrido, N. A., Sanhueza, P., Tatematsu, K., Towner, A. P. M., & Valeille-Manet, M. 2023, Astronomy & Astrophysics, 678, A194

El-Abd, S. J., Brogan, C. L., Hunter, T. R., Lee, K. L. K., Loomis, R. A., & McGuire, B. A. 2024, publisher: [object Object] Version Number: 1

El-Abd, S. J., Brogan, C. L., Hunter, T. R., Willis, E. R., Garrod, R. T., & McGuire, B. A. 2019, The Astrophysical Journal, 883, 129, arXiv:1907.13551 [astro-ph]

Elsila, J. E., Glavin, D. P., & Dworkin, J. P. 2009, Meteoritics & Planetary Science, 44, 1323

Favre, C., Despois, D., Brouillet, N., Baudry, A., Combes, F., Guélin, M., Wootten, A., & Wlodarczak, G. 2011, antike und abendland, 532, A32

Fischer, W. J., Hillenbrand, L. A., Herczeg, G. J., Johnstone, D., Kóspál, , & Dunham, M. M. 2022, Accretion Variability as a Guide to Stellar Mass Assembly, arXiv:2203.11257 [astro-ph]

Fischer, W. J., Safron, E., & Megeath, S. T. 2019, The Astrophysical Journal, 872, 183, aDS Bibcode: 2019ApJ...872..183F

Frank, A., Ray, T. P., Cabrit, S., Hartigan, P., Arce, H. G., Bacciotti, F., Bally, J., Benisty, M., Eislöffel, J., Güdel, M., Lebedev, S., Nisini, B., & Raga, A. 2014, in Protostars and Planets VI (University of Arizona Press)

Fuente, A., Cernicharo, J., Caselli, P., MCoey, C., Johnstone, D., Fich, M., van Kempen, T., Palau, A., Yidiz, U. A., Tercero, B., & López, A. 2014, antike und abendland, 568, A65

Garatti, A. C. o., Stecklum, B., Lopez, R. G., Eislöffel, J., Ray, T. P., Sanna, A., Cesaroni, R., Walmsley, C. M., Oudmaijer, R. D., de Wit, W. J., Moscadelli, L., Greiner, J., Krabbe, A., Fischer, C., Klein, R., & Ibañez, J. M. 2017, Nature Physics, 13, 276, arXiv:1704.02628 [astro-ph]

Garrod, R. T. 2013, The Astrophysical Journal, 765, 60

Garrod, R. T. & Herbst, E. 2006, Astronomy & Astrophysics, 457, 927

Garrod, R. T., Jin, M., Matis, K. A., Jones, D., Willis, E. R., & Herbst, E. 2022, The Astrophysical Journal Supplement Series, 259, 1, arXiv:2110.09743 [astro-ph]

Garrod, R. T., Weaver, S. L. W., & Herbst, E. 2008, The Astrophysical Journal, 682, 283

Ginsburg, A. & Mirocha, J. 2011, Astrophysics Source Code Library, ascl:1109.001, aDS Bibcode: 2011ascl.soft09001G

Ginsburg, A., Sokolov, V., de Val-Borro, M., Rosolowsky, E., Pineda, J. E., Sipőcz, B. M., & Henshaw, J. D. 2022, The Astronomical Journal, 163, 291, arXiv:2205.04987 [astro-ph]

Goldsmith, P. F. & Langer, W. D. 1999, The Astrophysical Journal, 517, 209

Gordy, W. & Cook, R. L. 1984, Microwave molecular spectra, 3rd edn. (New York: Wiley)

Gusdorf, A., Pineau Des Forêts, G., Cabrit, S., & Flower, D. R. 2008, Astronomy & Astrophysics, 490, 695

Helmich, F. P. & Van Dishoeck, E. F. 1997, Astronomy and Astrophysics Supplement Series, 124, 205

Herbst, E., Green, S., Thaddeus, P., & Klemperer, W. 1977, Astrophysical Journal, 215, 503

Herbst, E. & Van Dishoeck, E. F. 2009, Annual Review of Astronomy and Astrophysics, 47, 427

Herbst, E. & van Dishoeck, E. F. 2009, Annual Reviews of Astronomy and Astrophysics, 47, 427

Hollis, J. M., Jewell, P. R., Lovas, F. J., & Remijan, A. 2004, The Astrophysical Journal, 613, L45, aDS Bibcode: 2004ApJ...613L..45H

Horn, A., Møllendal, H., Sekiguchi, O., Einar, U., Roberts, H., Herbst, E., Viggiano, A. A., & Fridgen, T. D. 2004, Astrophysical Journal, 611, 605

Hunter, T. R., Brogan, C. L., De Buizer, J. M., Towner, A. P. M., Dowell, C. D., MacLeod, G. C., Stecklum, B., Cyganowski, C. J., El-Abd, S. J., & McGuire, B. A. 2021, The Astrophysical Journal Letters, 912, L17, arXiv:2104.05187 [astro-ph]

Hunter, T. R., Brogan, C. L., MacLeod, G., Cyganowski, C. J., Chandler, C. J., Chibueze, J. O., Friesen, R., Indebetouw, R., Thesner, C., & Young, K. H. 2017, The Astrophysical Journal, 837, L29, aDS Bibcode: 2017ApJ...837L..29H

Hunter, T. R., Indebetouw, R., Brogan, C. L., Berry, K., Chang, C.-S., Francke, H., Geers, V. C., Gómez, L., Hibbard, J. E., Humphreys, E. M., Kent, B. R., Kepley, A. A., Kunneriath, D., Lipnicky, A., Loomis, R. A., Mason, B. S., Masters, J. S., Maud, L. T., Muders, D., Sabater, J., Sugimoto, K., Szűcs, L., Vasiliev, E., Videla, L., Villard, E., Williams, S. J., Xue, R., & Yoon, I. 2023, Publications of the Astronomical Society of the Pacific, 135, 074501

Ilyushin, V., Kryvda, A., & Alekseev, E. 2009, Journal of molecular spectroscopy, 255, 32

Ilyushin, V. V., Endres, C. P., Lewen, F., Schlemmer, S., & Drouin, B. J. 2013, Journal of Molecular Spectroscopy, 290, 31

Jaber, A. A., Ceccarelli, C., Kahane, C., & Caux, E. 2014, Astrophysical Journal, 791

Jorgensen, J. K., Belloche, A., & Garrod, R. T. 2020, Annual Review of Astronomy and Astrophysics, 58, 727, arXiv:2006.07071 [astro-ph]

Jørgensen, J. K., van der Wiel, M., Coutens, A., Lykke, J., Muller, H., van Dishoeck, E., Calcutt, H., Bjerkeli, P., Bourke, T., Drozdovskaya, M., Fayolle, E., Favre, C., Garrod, R., Jacobsen, S., Öberg, K., Persson, M., & Wampfler, S. 2016, Astronomy & Astrophysics, 595, A117

Kennicutt, R. C. & Evans, N. J. 2012, Annual Review of Astronomy and Astrophysics, 50, 531

Kurayama, T., Nakagawa, A., Sawada-Satoh, S., Sato, K., Honma, M., Sunada, K., Hirota, T., & Imai, H. 2011, Publications of the Astronomical Society of Japan, 63, 513

Laas, J. C., Garrod, R. T., Herbst, E., & Widicus Weaver, S. L. 2011, The Astrophysical Journal, 728, 71

Lada, C. J. & Lada, E. A. 2003, Annual Review of Astronomy and Astrophysics, 41, 57

Lee, K. L. K., Loomis, R. A., Xue, C., El-Abd, S., & McGuire, B. A. 2023, molsim

Lefloch, B., Ceccarelli, C., & Codella, C. 2017, arxiv.v, 1

Ligterink, N. F. W., El-Abd, S. J., Brogan, C. L., Hunter, T. R., Remijan, A. J., Garrod, R. T., & McGuire, B. M. 2020, The Astrophysical Journal, 901, 37

Linnartz, H., Ioppolo, S., & Fedoseev, G. 2015, International Reviews in Physical Chemistry, 34, 205

Lykke, J. M., Favre, C., Bergin, E. A., & Jørgenson, J. K. 2015, antike und abendland, 582, A64

MacLeod, G. C., Smits, D. P., Goedhart, S., Hunter, T. R., Brogan, C. L., Chibueze, J. O., Van Den Heever, S. P., Thesner, C. J., Banda, P. J., & Paulsen, J. D. 2018, Monthly Notices of the Royal Astronomical Society, 478, 1077

Maret, S., Hily-Blant, P., Pety, J., Bardeau, S., & Reynier, E. 2011, Astronomy and Astrophysics, 526, A47, aDS Bibcode: 2011A&A...526A..47M

Martín, S., Martín-Pintado, J., Blanco-Sánchez, C., Rivilla, V. M., Rodríguez-Franco, A., & Rico-Villas, F. 2019, Astronomy & Astrophysics, 631, A159

McGuire, B. A. 2022, The Astrophysical Journal Supplement Series, 259, 30

McGuire, B. A., Brogan, C. L., Hunter, T. R., Remijan, A. J., Blake, G. A., Burkhardt, A. M., Carroll, P. B., Van Dishoeck, E. F., Garrod, R. T., Linnartz, H., Shingledecker, C. N., & Willis, E. R. 2018, The Astrophysical Journal Letters, 863, L35

McGuire, B. A., Burkhardt, A. M., Loomis, R. A., Shingledecker, C. N., Lee, K. L. K., Charnley, S. B., Cordiner, M. A., Herbst, E., Kalenskii, S., Momjian, E., Willis, E. R., Xue, C., Remijan, A. J., & McCarthy, M. C. 2020, The Astrophysical Journal, 900, L10, arXiv:2008.12349 [astro-ph]

McGuire, B. A., Shingledecker, C. N., Willis, E. R., Burkhardt, A. M., El-Abd, S., Motiyenko, R. A., Brogan, C. L., Hunter, T. R., Margules, L., Guillemin, J.-C., Garrod, R. T., Herbst, E., & Remijan, A. J. 2017a, The Astrophysical Journal Letters, 851, L46

McGuire, B. A., Shingledecker, C. N., Willis, E. R., Burkhardt, A. M., El-Abd, S., Motiyenko, R. A., Brogan, C. L., Hunter, T. R., Margulès, L., Guillemin, J.-C.,

Garrod, R. T., Herbst, E., & Remijan, A. J. 2017b, The Astrophysical Journal, 851, L46, arXiv:1712.03256 [astro-ph]

McGuire, B. A., Shingledecker, C. N., Willis, E. R., Kelvin Lee, K. L., Martin-Drumel, M.-A., Blake, G. A., Brogan, C. L., Burkhardt, A. M., Caselli, P., Chuang, K.-J., El-Abd, S., Hunter, T. R., Ioppolo, S., Linnartz, H., Remijan, A. J., Xue, C., & McCarthy, M. C. 2019, The Astrophysical Journal, 883, 201

McKee, C. F. & Tan, J. C. 2002, Nature, 416, 59

Meyer, D. M.-A., Vorobyov, E. I., Elbakyan, V. G., Eislöffel, J., Sobolev, A. M., & Stöhr, M. 2020, Monthly Notices of the Royal Astronomical Society, 500, 4448

Meyer, D. M. A., Vorobyov, E. I., Elbakyan, V. G., Eislöffel, J., Sobolev, A. M., & Stöhr, M. 2021, Monthly Notices of the Royal Astronomical Society, 500, 4448, aDS Bibcode: 2021MNRAS.500.4448M

Meyer, D. M.-A., Vorobyov, E. I., Kuiper, R., & Kley, W. 2017, Monthly Notices of the Royal Astronomical Society: Letters, 464, L90

Motte, F., Bontemps, S., & Louvet, F. 2018, Annual Review of Astronomy and Astrophysics, 56, 41

Möller, T., Endres, C., & Schilke, P. 2017, Astronomy & Astrophysics, 598, A7

Müller, H. S., Schlöder, F., Stutzki, J., & Winnewisser, G. 2005a, Journal of Molecular Structure, 742, 215

Müller, H. S. P., Schlöder, F., Stutzki, J., & Winnewisser, G. 2005b, Journal of Molecular Structure, 742, 215

Pickett, H. M., Poynter, R. L., Cohen, E. A., Delitsky, M. L., Pearson, J. C., & Muller, H. 1998a, Journal of Quantitative Spectroscopy and Radiative Transfer, 60, 883

Pickett, H. M., Poynter, R. L., Cohen, E. A., Delitsky, M. L., Pearson, J. C., & Müller, H. S. P. 1998b, Journal of Quantitative Spectroscopy and Radiative Transfer, 60, 883, aDS Bibcode: 1998JQSRT..60..883P

Qiu, K., Wyrowski, F., Menten, K. M., Güsten, R., Leurini, S., & Leinz, C. 2011, The Astrophysical Journal, 743, L25

Rathborne, J. M., Jackson, J. M., & Simon, R. 2006, The Astrophysical Journal, 641, 389

Reid, M. J., Menten, K. M., Brunthaler, A., Zheng, X. W., Dame, T. M., Xu, Y., Wu, Y., Zhang, B., Sanna, A., Sato, M., Hachisuka, K., Choi, Y. K., Immer, K., Moscadelli, L., Rygl, K. L. J., & Bartkiewicz, A. 2014, The Astrophysical Journal, 783, 130

Remijan, A., Snyder, L. E., Friedel, D. N., Liu, S.-Y., & Shah, R. Y. 2003, The Astrophysical journal, 590, 314

Remijan, A., Snyder, L. E., Liu, S.-Y., Mehringer, D., & Kuan, Y.-J. 2002, The Astrophysical journal, 576, 264

Remijan, A., Xue, C., Margulès, L., Belloche, A., Motiyenko, R. A., Carder, J., Codella, C., Balucani, N., Brogan, C. L., Ceccarelli, C., Hunter, T. R., Maris, A., Melandri, S., Siebert, M., & McGuire, B. A. 2022, Astronomy & Astrophysics, 658, A85, arXiv:2112.03356 [astro-ph]

Rivilla, V. M., Beltrán, M. T., Cesaroni, R., Fontani, F., Codella, C., & Zhang, Q. 2017, antike und abendland, 598, A59

Rivilla, V. M., Beltrán, M. T., Vasyunin, A., Caselli, P., Viti, S., Fontani, F., & Cesaroni, R. 2019, Monthly Notices of the Royal Astronomical Society, 483, 806

Rivilla, V. M., Martin-Pintado, J., Jimenez-Serra, I., & Rodriguez-Franco, A. 2013, Astronomy & Astrophysics, 554, A48, arXiv:1302.2763 [astro-ph]

Robitaille, T. & Bressert, E. 2012, Astrophysics Source Code Library, ascl:1208.017, aDS Bibcode: 2012ascl.soft08017R

Sakai, T., Sakai, N., Foster, J. B., Sanhueza, P., Jackson, J. M., Kassis, M., Furuya, K., Aikawa, Y., Hirota, T., & Yamamoto, S. 2013, The Astrophysical Journal, 775, L31

Schuessler, C., Remijan, A., Xue, C., Carder, J., Scolati, H., & McGuire, B. 2022, The Astrophysical Journal, 941, 102, arXiv:2208.05823 [astro-ph]

Shannon, R. J., Blitz, M. A., Goddard, A., & Heard, D. E. 2013, Nature Chemistry, 5, 745

Shepherd, D. S., Nurnberger, D. E. A., & Bronfman, L. 2004, The Astrophysical Journal, 602, 850

Shepherd, D. S., Povich, M. S., Whitney, B. A., Robitaille, T. P., Nurnberger, D. E. A., Bronfman, L., Stark, D. P., Indebetouw, R., Meade, M. R., & Babler, B. L. 2007, The Astrophysical Journal, 669, 464

Shingledecker, C. N. & Herbst, E. 2018, Physical Chemistry Chemical Physics, 20, 5359

Shu, F. H., Adams, F. C., & Lizano, S. 1987, Annual Review of Astronomy and Astrophysics, 25, 23

Skouteris, D., Balucani, N., Ceccarelli, C., Vazart, F., Puzzarini, C., Barone, V., Codella, C., & Lefloch, B. 2018, The Astrophysical Journal Letters, 854, 135

Snyder, L. E., Lovas, F. J., Hollis, J. M., Friedel, D. N., Jewell, P. R., Remijan, A., Ilyushin, V. V., Alekseev, E. A., & Dyubko, S. F. 2005, The Astrophysical Journal, 619, 914

Taquet, V., López-sepulcre, A., Ceccarelli, C., Neri, R., Kahane, C., & Charnley, S. B. 2015, Astrophysical Journal, 804, 81

The Casa Team, Bean, B., Bhatnagar, S., Castro, S., Meyer, J. D., Emonts, B., Garcia, E., Garwood, R., Golap, K., Villalba, J. G., Harris, P., Hayashi, Y., Hoskins, J., Hsieh, M., Jagannathan, P., Kawasaki, W., Keimpema, A., Kettenis, M., Lopez, J., Marvil, J., Masters, J., McNichols, A., Mehringer, D., Miel, R., Moellenbrock, G., Montesino, F., Nakazato, T., Ott, J., Petry, D., Pokorny, M., Raba, R., Rau, U., Schiebel, D., Schweighart, N., Sekhar, S., Shimada, K., Small, D., Steeb, J.-W., Sugimoto, K., Suoranta, V., Tsutsumi, T., Van Bemmel, I. M., Verkouter, M., Wells, A., Xiong, W., Szomoru, A., Griffith, M., Glendenning, B., & Kern, J. 2022, Publications of the Astronomical Society of the Pacific, 134, 114501

Tigé, J., Motte, F., Russeil, D., Zavagno, A., Hennemann, M., Schneider, N., Hill, T., Nguyen Luong, Q., Di Francesco, J., Bontemps, S., Louvet, F., Didelon, P., Könyves, V., André, P., Leuleu, G., Bardagi, J., Anderson, L. D., Arzoumanian, D., Benedettini, M., Bernard, J.-P., Elia, D., Figueira, M., Kirk, J., Martin, P. G., Minier, V., Molinari, S., Nony, T., Persi, P., Pezzuto, S., Polychroni, D., Rayner,

T., Rivera-Ingraham, A., Roussel, H., Rygl, K., Spinoglio, L., & White, G. J. 2017, Astronomy & Astrophysics, 602, A77

Turner, B. E. 1991, The Astrophysical Journal Supplement Series, 76, 617, aDS Bibcode: 1991ApJS...76..617T

Van Dishoeck, E. F. 2008, Proceedings of the International Astronomical Union, 4, 3

Vastel, C., Bottinelli, S., Caux, E., Glorian, J. M., & Boiziot, M. 2015, CASSIS: a tool to visualize and analyse instrumental and synthetic spectra., conference Name: SF2A-2015: Proceedings of the Annual meeting of the French Society of Astronomy and Astrophysics Pages: 313-316 ADS Bibcode: 2015sf2a.conf..313V

Vázquez-Semadeni, E., González-Samaniego, A., & Colín, P. 2016, Monthly Notices of the Royal Astronomical Society, stw3229

Wilkins, O. H., Carroll, P. B., & Blake, G. A. 2022, The Astrophysical Journal, 924, 4, aDS Bibcode: 2022ApJ...924....4W

Zernickel, A., Schilke, P., Schmiedeke, A., Lis, D. C., Brogan, C. L., Ceccarelli, C., Comito, C., Emprechtinger, M., Hunter, T. R., & Möller, T. 2012, Astronomy & Astrophysics, 546, A87, arXiv:1208.5516 [astro-ph]

Zhu, C., Byrd, R. H., Lu, P., & Nocedal, J. 1997, ACM Transactions on Mathematical Software, 23, 550